



TESIS DOCTORAL

**THREE DIMENSIONAL
LAGRANGIAN STRUCTURES IN
TURBULENT FLOWS:
APPLICATION TO OCEANIC
PROCESSES**

João Paulo Horta Bettencourt

Directores:

Dr. Cristóbal López
Prof. Emilio Hernández-García

Universitat de les Illes Balears

2014



**THREE DIMENSIONAL LAGRANGIAN STRUCTURES IN TURBULENT
FLOWS: APPLICATION TO OCEANIC PROCESSES**

João Paulo Horta Bettencourt
Instituto de Física Interdisciplinar y Sistemas Complejos (IFISC),
CSIC-UIB

PhD Thesis

Directores: Dr. Cristóbal López y Prof. Emilio Hernández-García

Cover: *Waves Breaking on a Lee Shore at Margate* (detail)
Joseph Mallord William Turner, c.1840
Tate Gallery, London

Copyright 2014, João Paulo Horta Bettencourt
Universidad de las Islas Baleares
Palma

This document was typeset with $\text{\LaTeX} 2_{\epsilon}$

Cristóbal López Sánchez, Profesor Titular de la Universidad de las Islas Baleares,
y Emilio Hernández-García, Profesor de Investigación del Consejo Superior de
Investigaciones Científicas

HACEN CONSTAR

que esta tesis doctoral ha sido realizada por el Sr. *João Paulo Horta Bettencourt*
bajo su dirección en el IFISC y, para que así conste, firman la misma.

Palma, 10 de Septiembre de 2014

Cristóbal López
Director

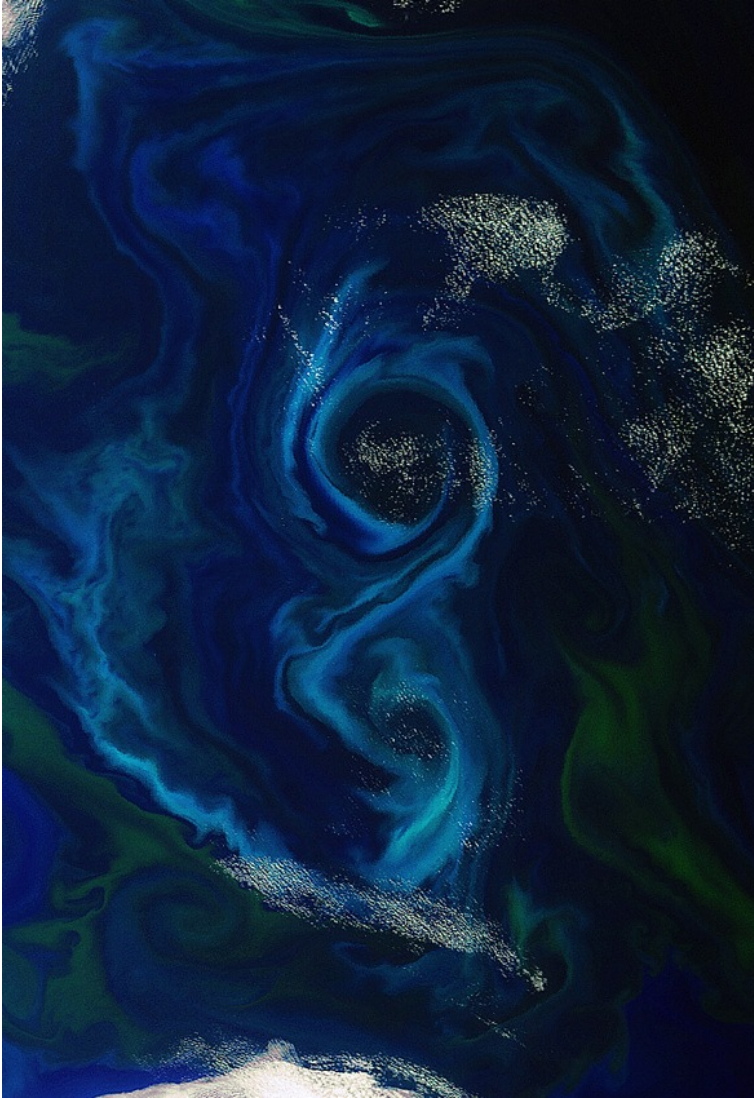
Emilio Hernández-García
Director

João Paulo Horta Bettencourt
Doctorando

Aos meus pais. A Sonia.

Tiene el mar su mecánica como el amor sus símbolos.

Pere Gimferrer



A southern summer bloom: a phytoplankton bloom swirls a figure-of-8 in the South Atlantic Ocean about 600 km east of the Falkland Islands. Photo: ESA

Índex

Índex	xi
Preface	xv
Abstract	xix
Resumen	xxv
Introduction	1
1 Introduction	3
1.1 Time and space scales of oceanic motions	4
1.2 Energetics of oceanic motions	6
1.3 Mesoscale motions in the ocean	7
1.4 Vertical motions in the ocean	8
1.5 Motivation and outline of the thesis	12
1.6 Acknowledgements	13
2 General notions	15
2.1 Fixed points and stability	16
2.2 Conservation laws for fluid motions	18

xi

2.3	Turbulent flows	19
2.3.1	Two-dimensional turbulence	23
2.4	Coherent structures	24
2.4.1	Coherent structures in 2d turbulence	25
2.5	Dispersion in turbulent flows	28
2.6	Chaotic advection	29
2.7	Mixing	30
2.8	Stretching and alignment in turbulent flows	33
2.9	Non-asymptotic Lyapunov exponents	35
2.9.1	The finite-time Lyapunov exponent (FTLE)	35
2.9.2	The finite-size Lyapunov exponent (FSLE)	36
2.10	Lagrangian coherent structures (LCS)	37
2.10.1	Lagrangian view of coherent structures	37
2.10.2	LCS in 3d as ridges of FSLE fields	39
2.10.3	Calculation of 3d FSLE fields	41
2.11	Numerical modeling of turbulent flows	42

Three-dimensional Lagrangian structures in turbulence 45

3 Coherent structures in a turbulent channel flow 47

3.1	Introduction	48
3.2	Data	49
3.3	Results	53
3.4	Conclusions	64

Applications to oceanic processes 67

4 Oceanic 3d Lagrangian Coherent Structures 69

4.1	Introduction	69
4.2	Data and Methods.	70
4.2.1	Velocity data set.	70
4.2.2	3d FSLE fields.	72
4.3	Results	74
4.3.1	Backward and forward 3d FSLE fields	74
4.3.2	Study of the dynamics of a relevant mesoscale eddy	77
4.4	Discussion.	83
4.5	Conclusions	88

5	Mesoscale stirring in the Peru Oxygen Minimum Zone	89
5.1	Introduction	90
5.2	Data	91
5.2.1	Circulation and Oxygen Minimum Zone modeling	91
5.2.2	3d FSLE fields	92
5.3	Results	92
5.3.1	Backward FSLE 3d fields	92
5.3.2	Exit times	96
5.3.3	Correlations between mean FSLE and O ₂ fields	98
5.3.4	Ventilation by eddies and eddy fluxes	102
5.3.5	Cross-wavelet spectra	108
5.4	Conclusions	109
6	Lagrangian structures in a coastal filament	111
6.1	Introduction	111
6.2	Data	113
6.2.1	Simulation of the Western Iberian shelf	113
6.2.2	3d FSLE fields	114
6.3	Results	114
6.3.1	FSLE fields and mesoscale structures	114
6.3.2	Formation and evolution of a coastal filament	117
6.3.3	Lagrangian structure and transport in the filament	120
6.3.4	3d Lagrangian structure of the filament	125
6.4	Conclusions	129
	Conclusions	131
7	General Conclusions	133
	Appendices	135
A	Numerical Methods	137
A.1	Interpolation in the ROMS grid	137
A.1.1	The ROMS curvilinear, terrain following grid	137
A.1.2	Interpolation procedure	138
A.1.3	Trajectory integration in curvilinear coordinates	139

A.2 Differentiation of scalar fields	140
A.3 The stretched vertical node distribution	141
List of Tables	143
List of Figures	145
Bibliography	153
References	155
Curriculum Vitae	169

Preface

Preface

In the late summer of 2010, having worked as an hydrodynamic design engineer for two years before, I found myself sitting in a dinner table at a hotel restaurant, overlooking the Mediterranean Sea from the italian coast at Sperlonga, a small town in the province of Latina, about halfway between Rome and Naples.

I was enjoying a five course dinner in the company of established theoretical physicists when one of them said something like:

We are not engineers. Engineers do what they are told without questioning. We scientists have to be critical and question everything.

Those words remained in my mind, periodically resurfacing and asking for reflection, and as my doctoral work progressed and my contact with science increased, I found myself thinking that the words were true. Indeed, science and engineering are two different activities that call for different mindsets, and I have come to agree that engineers, by necessity, do not question their established methods and results while the scientist has an obligation to do so if the need arises and while for the former creativity is bound by established rules and most of the times it is looked upon with suspicion for the latter it is nothing more than a tool of the trade that should be used as often as possible.

Now, as I write my thesis, I realize that in addition to the results presented in this document, I have achieved also a change of mind that is necessary first step in becoming a scientist and for this I have mainly to thank my advisors Profs. Cristóbal López and Emilio Hernández-García. To them, I owe a great deal and hope they are not too much disappointed with this outcome. To them, I say with sincerity: Thank you!

I would like to thank also my colleagues at IFISC for maintaining a active and stimulating working environment, noisy at times but always interesting. My time at IFISC showed me how a serious research institute should be run. This is a valuable insight for anyone starting a career in science and I thank the senior scientists for running such a tidy ship.

During this period, I had the privilege of being in contact with outstanding scientists whose knowledge and attitude towards science helped to shape my views of the scientist's tasks. I thank Drs. Véronique Garçon, Aurélien Paulmier, Boris deWitte, Ivonne Montes, Álvaro Peliz, Vincent Rossi, Ismael Hernández-Carrasco and Martinho Marta-Almeida for all the enlightning discussions we had.

To my family in Mallorca, Óscar, Bárbara and Marcos a warm thank you for making me feel at home away from home.

Finally, I thank Sonia with all my heart for the patience and unwavering support that were necessary to accompany me in this journey. No matter how I write, words will always fail to express my deepest admiration and gratitude for her courage, caring and tenderness that I have had the privilege of receiving. Thank you, minha cerejinha.

Abstract

Abstract

The dynamics of the ocean is characterized by multiple time and space scales of motion driven by the energy input at the large scale ocean gyres. Through the mechanism of baroclinic instability, a substantial part of this energy input is transferred to mesoscale motions, characterized by time and space scales of weeks to months and tens to hundreds of kilometers. These mesoscale motions are ubiquitous in the global ocean and occur as Rossby waves or mesoscale eddies. These last are masses of fluid in nonlinear rotation, typically with diameters of the order of 100 kms and depths up to 1000 meters. They are long lived (life spans reaching few months) and can carry differentiated water masses through hundreds of kilometers across the open ocean.

Water masses in the ocean move principally in the horizontal, and vertical velocities are normally negligible due to the combined effect of rotation and stratification. However, vertical motions are at the core of extremely important processes in the ocean, specially in the vertical exchange of tracers between the stratified interior and the well mixed superficial layers. The supply of nutrients to the usually nutrient depleted surface waters, where photosynthesis and production of new organic matter occurs, is one of such processes. Mesoscale motions are an important driver of these vertical exchanges and are responsible for a large supply of nutrients to the euphotic layer.

Mesoscale eddies are coherent, i.e., they maintain their identity for long enough time to allow their observation. Coherent structures are common in a large variety of turbulent flows and are thought to play a major role in turbulent processes. They have been mostly studied in the Eulerian perspective where persistent correlations between flow quantities are sought in a fixed spatial domain. However, by not following the fluid motion, Eulerian techniques are limited because they

miss a major aspect of coherency: the transport of the same fluid mass by the coherent motion. The Lagrangian viewpoint, on the other hand follows the fluid as it moves and thus is a natural way of looking at coherent fluid motions.

The Lagrangian perspective of ocean dynamics has benefited greatly with the adoption of several concepts and tools from dynamical systems theory. These contributions deal with the fate of individual trajectories of fluid particles and with ensembles of particles. The study of these provides a powerful insight into the transport properties of turbulent flows and how these properties affect the budget of physical and biogeochemical tracers such as carbon dioxide or oxygen in the ocean. A very useful concept is the Lagrangian coherent structure that may be defined as a region of the flow that greatly impacts the behavior of fluid masses in its vicinity. They behave as barriers or pathways to transport in the ocean and have an important effect in the turbulent fluxes of tracers. Most of the applications have been to two dimensional (2d) settings but given the importance of vertical motions in several critical processes occurring in the ocean, the study of these structures in three dimensions (3d) is a pressing and prominent step forward in our understanding of the ocean. A resume of the contributions of this thesis follows:

In a canonical turbulent flow in a channel, the 3d Lagrangian coherent structures were found to be related to eddies that are created at the near-wall portion of the channel and are advected normally to the wall by the turbulence itself. Unlike 3d Eulerian coherent structures, Lagrangian structures function as 3d barriers separating the inner turbulent motions from the more quiet center region of the channel. They are advected at the mean flow speed and thus have a material character.

In the oceanic setting of the Benguela upwelling region, the relatively small magnitude of vertical velocities confines the motions to quasi 2d planes. The 3d Lagrangian structures we observe are then quasi vertical and populate the region, signaling the complexity of ocean transport in mesoscale active regions. They form material barriers around mesoscale eddies and the exchange of water between the eddy interior and the exterior is controlled by the evolution of these 3d Lagrangian eddy boundaries.

Oceanic tracer budgets are strongly affected by stirring, i.e., the process of intensification of the tracer gradient by advection. In the oxygen minimum zone (OMZ) off Peru, mesoscale eddies are ubiquitous and the associated Lagrangian structures are strongly correlated to enhanced O_2 gradients in the OMZ core, along a region between 400 and 600 m depth. Furthermore, the Lagrangian barriers around the eddies allow them to carry O_2 rich waters into the OMZ, in episodic ventilation events. The combined effect of these events is to enhance

turbulent fluxes of O_2 into the OMZ, that are one order of magnitude higher than the mean O_2 fluxes.

Coastal filaments play an important role in the cross-shore exchange of water masses. These filaments are frequently observed in upwelling regions. In the Iberian upwelling region, the 3d Lagrangian structures defining the 3d structure of the offshore transport through a filament, were found to be barriers that prevented the fluid inside the filament to mix with outside water. These 3d structures provided a channel that transported the flow from the coastal upwelling source to a cyclonic eddy in open waters.

Summing up, in three different oceanic settings, 3d Lagrangian structures were found to determine fluid transport and consequently the exchange of physical and biogeochemical properties between distinct physical and biogeochemical regions: mesoscale eddy interior/exterior in the Benguela upwelling regions; the Peruvian OMZ core/exterior oxygenated regions and nearshore cold waters and offshore warm waters in the Iberian upwelling region.

Resumen

Resumen

La dinámica del océano se caracteriza por múltiples escalas espacio-temporales regidas por el suministro de energía en los giros oceánicos de gran escala. A través del mecanismo de inestabilidad baroclínica una gran parte de esta energía es transferida a los movimientos de mesoescala caracterizados por escalas espacio-temporales de semanas a meses y de decenas a cientos de kilómetros. Estos movimientos de mesoescala son comunes en el océano y ocurren como ondas de Rossby o remolinos de mesoescala. Estos últimos constituyen fluido en rotación no lineal, típicamente con diámetros del orden de los 100 kilómetros y profundidades de hasta los 1000 metros. Éstos tienen un tiempo de vida extenso alcanzando algunos meses de existencia y pueden transportar masas de agua diferenciadas cientos de kilómetros a través del océano.

Las masas de agua en el océano se mueven principalmente en la horizontal y las velocidades verticales son normalmente despreciables debido al efecto combinado de la rotación y la estratificación del océano. Sin embargo, los movimientos verticales están en el núcleo de procesos oceánicos muy importantes, especialmente en el intercambio vertical de los trazadores entre el interior estratificado del océano y las capas superficiales bien mezcladas. Uno de estos procesos es el suministro de los nutrientes hacia las aguas superficiales, usualmente desprovistas de nutrientes, donde la fotosíntesis y la producción del nuevo material orgánico ocurren. Los movimientos de mesoescala son un importante conductor de estos intercambios verticales y son los responsables de una gran aportación de nutrientes a la capa eufótica.

Los remolinos de mesoescala son coherentes y esto significa que los mismos conservan su identidad durante un tiempo suficientemente largo como para permitir su observación. Las estructuras coherentes son comunes en una gran variedad de

flujos turbulentos y se piensa que juegan un importante papel en los procesos turbulentos. Estos han sido principalmente estudiados en la perspectiva Euleriana, en la cual se buscan correlaciones persistentes entre las cantidades del flujo en un dominio espacial fijo. Sin embargo, al no seguir el movimiento del fluido, las técnicas Eulerianas son limitadas porque estas no consideran un aspecto mayor de la coherencia: el transporte de la misma masa del fluido por un movimiento coherente. El punto de vista Lagrangiano, por otra parte, sigue al fluido mientras este se mueve y entonces es un medio natural de observar los movimientos coherentes del fluido.

La perspectiva Lagrangiana de la dinámica del océano ha sido beneficiada en gran medida con la adopción de varios conceptos y herramientas de la teoría de sistemas dinámicos. Estas contribuciones tienen que ver con las trayectorias individuales de las partículas del fluido y con conjuntos de partículas. El estudio de estas permite profundizar el estudio del transporte de las propiedades de flujos turbulentos y conocer como estas propiedades afectan el balance de los trazadores físicos y biogeoquímicos tales como el dióxido de carbono o el oxígeno en el océano.

Un concepto muy útil es la estructura coherente Lagrangeana que puede ser definida como una región del flujo que afecta en gran medida el comportamiento de las masas de agua alrededor. Estas se comportan como barreras o avenidas para el transporte en el océano y tienen un efecto importante en los flujos turbulentos de los trazadores. Muchas de las aplicaciones de este concepto han sido en entornos bidimensionales (2d) pero dada la importancia de los movimientos verticales en procesos críticos que ocurren en el océano, el estudio de estas estructuras en 3 dimensiones (3d) constituye un paso hacia adelante en el conocimiento del océano. A continuación se presenta el resumen de esta tesis:

En un flujo canónico turbulento en un canal, las estructuras Lagrangianas coherentes en 3d están relacionadas con los remolinos que son creados en una región próxima de la pared del canal y son transportadas hacia el interior del canal por la propia turbulencia. Por el contrario de las estructuras Eulerianas 3d coherentes, las estructuras Lagrangianas funcionan como una barrera 3d, separando los movimientos turbulentos próximos a la pared de la región central del canal. Estas son transportadas a la velocidad del flujo medio y por esto tienen un carácter material.

En el entorno oceánico de la región de Benguela, la magnitud relativamente pequeña de las velocidades verticales limita los movimientos a planos casi 2d. Las estructuras Lagrangianas 3d que se observan son casi verticales y ocupan la región, indicando la complejidad del transporte oceánico en las regiones de mesoescala activas. Estas forman barreras de material alrededor de los giros de mesoescala

e intercambian agua entre el interior y el exterior del remolino controlado por la evolución de las fronteras de estos giros Lagrangeanos 3d.

El balance oceánico de los trazadores está fuertemente influenciado por la advección, o sea, el proceso de intensificación del gradiente del trazador. En la zona de oxígeno mínimo (OMZ) en la costa de Perú, los remolinos de mesoescala son ubícuos y están asociados a las estructuras Lagrangianas, que están fuertemente correlacionadas con los gradientes de O_2 intensificados en el núcleo de la OMZ a lo largo de una región entre los 400 y los 600 m de profundidad. Además, las barreras Lagrangianas alrededor de los remolinos permiten transportar el agua rica en O_2 hacia el interior de la OMZ mediante eventos de ventilación episódicos. El efecto combinado de estos eventos produce el incremento de flujos turbulentos de O_2 hacia el interior de la OMZ que son un orden de magnitud mas grandes que los flujos medios de O_2 .

Los filamentos costeros juegan un papel importante en el intercambio de masas de agua entre la costa y el océano abierto. Estos filamentos son frecuentemente observados en las regiones de afloramiento costero. En la region Ibérica de afloramiento, se ha encontrado que las estructuras Lagrangianas 3d, que definen las estructuras 3d del transporte hacia el océano abierto a través del filamento, son barreras que previnien que el algua dentro del filamento se mezcle con el agua exterior. Estas estructuras 3d forman un canal que transporta el flujo desde la fuente costera de afloramiento hacia un remolino ciclónico en aguas abiertas.

Para concluir, en tres diferentes entornos oceánicos, se ha encontrado que las estructuras Lagrangianas 3d determinan el transporte del fluido y por consiguiente el intercambio de las propiedades físicas y biogeoquímicas entre el interior y el exterior de remolinos de mesoescala en la region de afloramiento de Benguela; entre las regiones del núcleo y el exterior oxigenado de la OMZ peruana y entre las aguas frías costeras y las aguas cálidas exteriores en la región Ibérica de afloramiento costero.

Introduction

Introduction

The oceans are restless. They are in a state of perpetual motion sustained by the action of the winds at the ocean surface and by density differences in the surface and in the ocean's interior. These motions drive important oceanic processes that greatly affect the state of the planet and of life in it. From the maintenance of fishery stocks to carbon sequestration from the atmosphere, oceanic processes play an indisputable role in the fate of planet Earth and of its living organisms.

Motions in the ocean are turbulent: three-dimensional, nonlinear, random, diffusive, dissipative and continuous*. In our study of the dynamics of the ocean we may at times neglect one or more of these aspects for the convenience of the analysis, but ultimately they are common to all processes, although their relative importance can be quite different.

Three-dimensionality is an aspect that is often put aside in the analysis of oceanic motions due to the fact that the Earth's rotation and the stratification of the ocean greatly limit vertical motions of water parcels, resulting in vertical velocities that are several orders of magnitude smaller than the horizontal ones. Nonetheless, as weak as they may be, vertical motions play a very important role in the state of the oceans because they, among other things, provide mechanisms for the sinking of ventilated surface waters to the abyss and for bringing nutrients to the euphotic zone, where through photosynthesis, production of organic matter occurs.

Randomness and diffusivity in the ocean are connected in the phenomenon of mixing. Mixing is a combination of two distinct processes: stirring and diffusion. Turbulence promotes energetic motions of water parcels with distinct concentrations. Due to the nonlinearity of eddy motions, scalars fields are deformed by the

*List adapted from [1]

CHAPTER 1. INTRODUCTION

rotating and translating eddies (stirring) producing elongated features (filaments) that can bring waters with different physical, chemical and biological signatures into contact. The current view [2] is that the stirring process will intensify gradients up to a level where molecular diffusion will overcome the intensification process and eventually mix locally the water masses. Additionally, the eddies can carry with them physical, chemical and biological anomalies across considerable distances before disappearing.

The quasi-steady state circulation of the ocean implies that the energy imparted to oceanic motions must be lost by other processes or else the circulation would accelerate. This is accomplished through the dissipative character of phenomena such as wave breaking or bottom drag. Another pathway for the dissipation of energy is viscous dissipation whereby kinetic energy is transformed into internal energy of the fluid. This requires that a continuum of time and space scales exist in the ocean so that the energy forcing the motions at large scales is transferred to the smallest scales of motion where it is dissipated by molecular viscosity.

1.1

Time and space scales of oceanic motions

The oceanic motions and the processes that these control occur on a large spectrum of time and space scales. At the seaside, one can observe surface waves with periods in the range of one to ten seconds and wave heights from centimeters to several meters; tides are also ubiquitous phenomena in almost all coastal areas with periods from several hours to one day and amplitudes in the meter range. Currents may also be casually observed stretching for several kilometers along the coast. The set of ocean dynamics that is readily observable through the naked eye is only a small subset of the full range of ocean motions that are known. On the small time/space scale end of the spectrum (see Figure 1.1), molecular processes are present while on the opposite end of the spectrum we have decadal oscillations and climate variations occurring over scales of 10-100 years and across 1000-10000 km. What Figure 1.1 also shows is that the spectrum of oceanic motions is continuous both in time and space. In this thesis, we will be concerned primarily with the medium range of ocean dynamics: the mesoscale motions occupying the spectrum between the weekly to yearly periods and 10 km to 500 km of spatial expression.

1.1. TIME AND SPACE SCALES OF OCEANIC MOTIONS

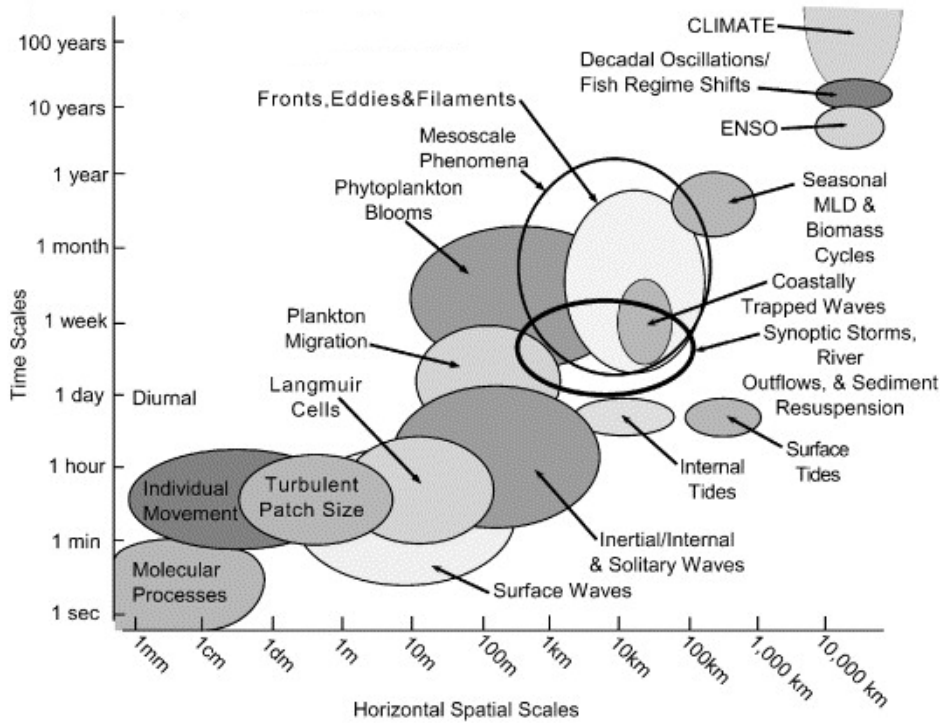


Figure 1.1: Time and space scales of oceanic processes. Adapted from [3].

CHAPTER 1. INTRODUCTION

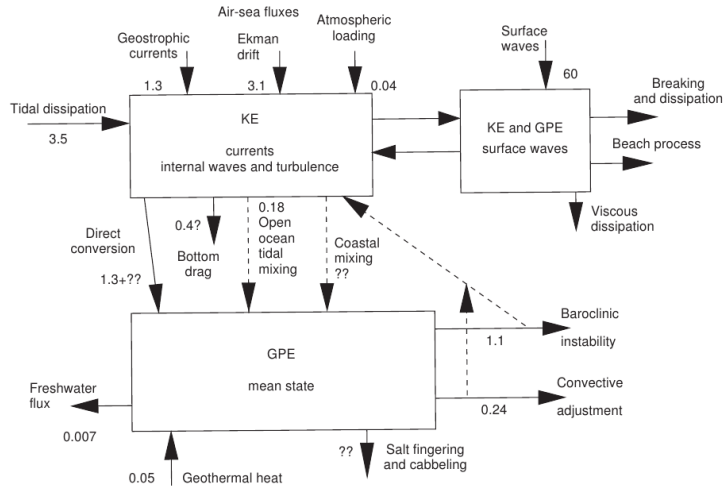


Figure 1.2: Mechanical energy balance for the world's oceans in TW [4]. KE – Kinetic Energy. GPE – Gravitational Potential Energy.

1.2

Energetics of oceanic motions

The major source of energy to the oceans is the heat flux of solar radiation [4], amounting to 52.4 PW (1 PW = 10^{15} W). Although the oceans are subject to differential heating they are not a heat engine. Sandstrom's theorem [5] states that a closed circulation can be maintained in the ocean only if the heating source is situated at a pressure level higher than the cooling source. The atmosphere is heated from below and cools at the top, but the ocean is heated and cooled from the surface (neglecting geothermal heat fluxes) so there should be no circulation driven by the thermal forcing. The fact that there is a circulation raises the important question of how? The answer is mechanical mixing that carries the warmer fluid to a higher pressure thereby lowering the effective level of heating of the oceans [6]. The main sources of this mechanical mixing are wind stress and tides [7](see Figure 1.2).

Ekman flux convergence creates a vertical velocity (Ekman pumping) W_E at the base of the Ekman layer. The pumping is responsible for pushing warm water into the subsurface ocean and thus forming the bowl shaped main thermocline in the subtropical ocean [8, 9]. This process of lifting of isopycnal surfaces acts as a means of conversion of kinetic energy to gravitational potential energy and

1.3. MESOSCALE MOTIONS IN THE OCEAN

estimates based on scaling analysis show that the potential energy available by this process is 1000 times larger than the kinetic energy associated to the mean wind-driven circulation [10].

Steep isopycnal surfaces along the edges of the wind driven ocean gyres are baroclinically unstable and the available potential energy can be converted by this mechanism to eddy kinetic energy, that can be 100 times higher than the kinetic energy of the mean flow [10]. Maximum energy transfer rates are found for eddies with wavelength of 200 km and e-folding times of 80 days, placing these features of oceanic circulation in the mesoscale range of oceanic motions. Since eddy energy is mostly dissipated by small scale processes, this mechanism provides a sink to the potential energy of the mean flow through mesoscale motions.

1.3

Mesoscale motions in the ocean

Satellite global observations of sea-surface height (SSH) anomalies have revealed that more than half of the SSH variability is due to features with amplitudes of 5-25 cm and diameters of 100-200 km, propagating westward at the phase speed of nondispersive baroclinic Rossby waves [11]. While earlier studies attributed this observations to linear Rossby waves (with modifications due to effects not accounted for in the classical theory) [12], more recent observations [11, 13] have determined the prevalence of coherent vortices with $O(100 \text{ km})$ radii and mean amplitude of 8 cm. These vortices are long lived (average lifetime of 32 weeks) and propagate on average 550 km.

An important feature of these vortices is their nonlinearity, as measured by the ratio U/c where U is maximum rotational speed within the vortex interior and c the propagation speed. When $U/c > 1$ the vortex is nonlinear and there is trapped fluid in its interior. These coherent nonlinear vortices are termed mesoscale eddies. The eddy polarity is fairly equally distributed between cyclonic and anticyclonic eddies, although there is a preference for the strongest eddies to be anticyclonic in the Northern hemisphere and cyclonic in the Southern hemisphere [13]. Highly nonlinear eddies follow the same preference.

SSH anomalies with length scales larger than those of mesoscale eddies propagate westward at phase speeds higher than eddy propagation speed, which signal the existence of features obeying linear Rossby waves dynamics. There is however a fundamental difference in that mesoscale eddies, unlike linear Rossby waves, are capable of transporting momentum, heat, mass and chemical species of seawater for long distances and travelling times.

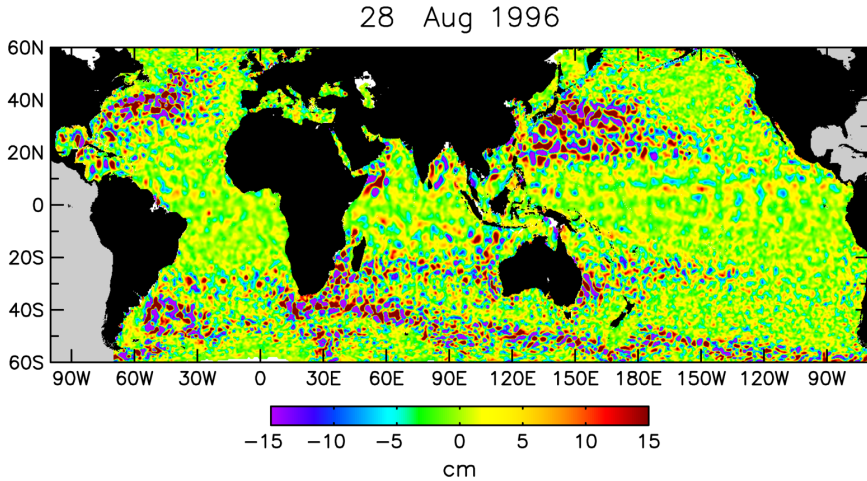


Figure 1.3: Global map of SSH on 28 August 1996 constructed from the merged T/P and ERS-1 data after spatially high-pass filtering with half-power filter cutoffs of 20° of longitude by 10° of latitude [13].

The mesoscale variability is the dominant signal in the ocean circulation [14]. Areas of intense mesoscale activity are (see Figure 1.3) the western boundary currents and the Antarctic Circumpolar Current. Open ocean currents that are part of the large scale gyre circulation also contain mesoscale eddies. At the eastern boundaries we observe vigorous currents and coastal upwelling systems exhibiting high levels of mesoscale activity [14]. Although mixing and transport in the oceans occur in a wide range of scales, mesoscale and sub-mesoscale (length scales of 1-10 km) variability are known to play a very important role [15–20]. In the southern Benguela, for instance, cyclonic eddies shed from the Agulhas current can transport and exchange warm waters from the Indian Ocean to the South Atlantic [21, 22].

1.4

Vertical motions in the ocean

Vertical motions in the ocean, named upwelling or downwelling, are sustained by velocities much smaller than the horizontal ones. These motions are nevertheless extremely important, as already mentioned. A first mechanism promoting

1.4. VERTICAL MOTIONS IN THE OCEAN

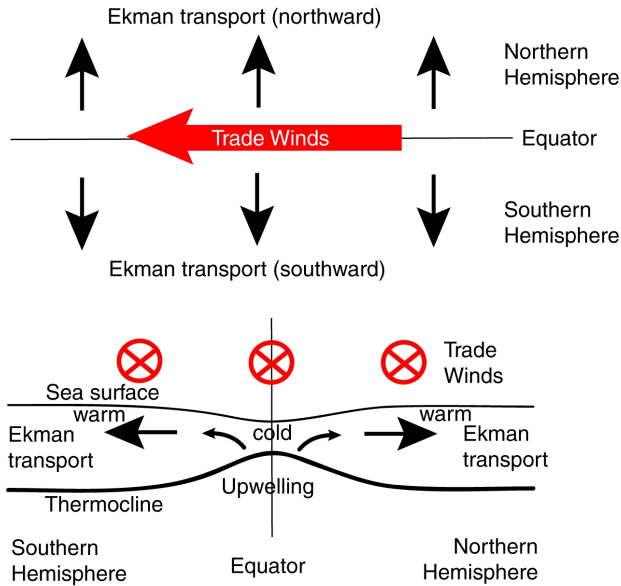


Figure 1.4: Ekman transport divergence near the equator driven by easterly trade winds. Top: Ekman transports; Bottom: Meridional cross-section showing effect on the thermocline and surface temperature. Adapted from [23].

CHAPTER 1. INTRODUCTION

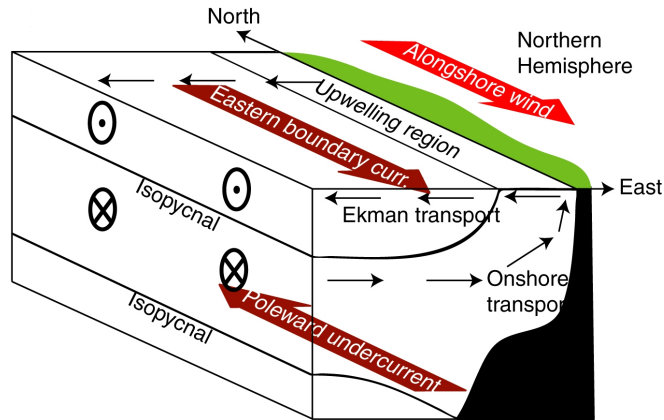


Figure 1.5: Coastal upwelling system due to an alongshore wind with offshore Ekman transport (Northern Hemisphere). Adapted from [23].

such motions is Ekman divergence or convergence, whereby differential Ekman transport caused by differences in wind stress across the ocean surface cause, by necessity of mass conservation, the raising of subsurface waters in the case of divergence or the sinking of surface waters in the case of Ekman convergence. This mechanism is responsible for **Equatorial upwelling** (Figure 1.4) or the aforementioned raising of density surfaces at the edges of oceanic gyres.

A related mechanism, due also to Ekman dynamics, is **coastal upwelling**. Here, an alongshore wind stress, with the coast to its left (right) in the Northern (Southern) hemisphere will induce an offshore Ekman transport in the surface layer (Figure 1.5). This offshore motion requires, in turn, to conserve mass, an upward motion of coastal waters to compensate. In ideal, 2d, circumstances, this motion is supplied by an onshore flow below the surface water layer. This supply of sub-surface, nutrient enriched waters is responsible for making coastal upwelling regions the most biologically active and productive marine zones in the world [24, 25].

Associated with the upward motion of cold subsurface waters is the raising of isopycnal surfaces, producing an outcropping of these surfaces and strong cross-shore density gradients. This thin strip of strong density change is called the upwelling front and it is a major component of the dynamics of coastal upwelling. Due to this density gradient, an alongshore current is expected, by the thermal wind relation [26]. In fact, a complex pattern of equatorward currents and poleward counter-currents are usually found in these upwelling regions whose in-

1.4. VERTICAL MOTIONS IN THE OCEAN

stability mechanisms are a major source of mesoscale variability in the form of mesoscale eddies, fronts and submesoscale filaments [27–30]. The mesoscale eddy activity in these upwelling areas seems to suppress production due to the induced offshore export of nutrients [24, 31, 32]. Studies of the vertical structure of such eddies in the Benguela region (e. g. [33] and [34]) have shown that they can extend to one thousand meters deep waters.

Mesoscale motions are themselves relevant in the promotion of vertical motions in the ocean. Many physical and biogeochemical tracers exhibit a common structure with high vertical gradients found just below the mixed layer. After sufficient time a tracer balance will be achieved whereby the vertical tracer concentration is maintained by the source/sink at the upper ocean (biological production and air-sea exchanges) in equilibrium with the upper ocean/interior vertical tracer exchange and tracer supply in the ocean interior. During winter, the deepening of the mixed layer favors vertical convection and exchange but in the remaining of the year stratification prevents the surface/ocean interior exchange through mixed layer vertical velocities. Therefore, only vertical motions below the mixed layer can be responsible for the vertical fluxes of tracers. This vertical velocity is due almost entirely to mesoscale motions [30, 35, 36]. Indeed, mesoscale eddies have been shown to drive important biogeochemical processes in the ocean such as the vertical flux of nutrients into the euphotic zone [37–39].

One of the processes by which mesoscale eddies contribute to this vertical flux is the eddy pumping mechanism [40–43], where uplifting of isopycnals occurs at the center of cyclonic and mode-water eddies, bringing thermocline waters into the surface layer (anticyclones have an opposite effect). Another process that enhances vertical exchanges in mesoscale eddies is the eddy/wind interaction [44] whereby Ekman divergence inside the eddy produces persistent vertical velocities.

Another effect of eddy activity seems to be the intensification of mesoscale and sub-mesoscale variability due to the filamentation process where strong tracer gradients are created by the stretching of tracers in the shear- and strain-dominated regions in between eddy cores [45]. In this view, important vertical motions occur at the eddy periphery or in between eddies [16]. The intense straining motions may create large horizontal density gradient, that will force a vertical velocity response according to the Omega equation [46]. High resolution surveys of a density front found vertical velocities up to 40 m/day at 200 m of depth [47]. At eddy boundaries, that may be thought of as circular fronts, nonlinear Ekman pumping was proposed as a mechanism for enhanced vertical velocities [15] and for stimulating the injection of nutrients at the submesoscale in oligotrophic regions of the ocean [39].

Motivation and outline of the thesis

In the last decades new developments in the description and modeling of oceanic mixing and transport from a Lagrangian viewpoint have emerged [48, 49]. These Lagrangian approaches have become more and more frequent due to the increased availability of detailed knowledge of the velocity field from Lagrangian drifters, satellite measurements and computer models.

In particular, the very relevant concept of Lagrangian coherent structure (LCS) [50, 51] is becoming crucial for the analysis of transport in flows. LCSs are structures that separate regions of the flow with different dynamical behavior. They give a general geometric view of the dynamics, acting as a (time-dependent) roadmap for the flow. They are templates serving as proxies to, for instance, barriers and avenues to transport or eddy boundaries [51–56].

In the ocean, where it is widely recognized that filamentary structures, eddies, and in general oceanic meso- and submeso-scale structures have a great influence on marine ecosystems the identification of LCSs and the study of their role in the transport of biogeochemical tracers has primarily been restricted to two-dimensional (2d) layers [24, 32, 57, 58]. There are two concurrent reasons for this: a) because of stratification and rotation, vertical motions in the ocean are usually very small when compared to horizontal displacements; b) synoptic measurements (e.g. from satellites) of relevant quantities are restricted to the surface.

There are, however, areas in the ocean where vertical motions are fundamental, as discussed in the previous section. Thus, the identification of the three-dimensional LCSs in these areas is crucial and their relevance begins to be unveiled in atmospheric contexts [59–61] and in a turbulent channel flow in [62]. A kinematic ABC flow was studied in [63] and a few previous results for mesoscale eddies in 3d were obtained in [64, 65], by applying the methodology of lobe dynamics and the turnstile mechanism.

Given the success in the application of the concept of Lagrangian structures in 2d oceanic settings and the importance of 3d mesoscale dynamics as a source of vertical motions in the ocean, the objective of this thesis is to study the 3d characteristics of Lagrangian structures and their influence on oceanic processes. To accomplish this, we compute 3d fields of finite size Lyapunov exponent (FSLE) for different oceanic settings and use the concept of ridge of the scalar FSLE field to locate Lagrangian coherent structures. Due to the scarcity of measured 3d velocity fields in the ocean, we were limited to the use of numerical data

1.6. ACKNOWLEDGEMENTS

from simulations of the ocean. Moreover, we focused on situations where vertical motions play an important role: mesoscale phenomena in coastal upwelling areas.

This thesis is organized as follows:

In chapter 2 we introduce general notions and concepts of dynamical systems theory and of turbulent fluids that form the theoretical basis of this work. Especially, concepts such as stable and unstable manifolds, Lyapunov exponents and Lagrangian coherent structures are introduced.

In chapter 3 we study the nature of Lagrangian structures in a canonical turbulent flow denominated channel (Poiseuille) flow by computing 3d FSLE fields and extracting ridges of the FSLE fields. We compare their characteristics with the known Eulerian results for coherent structures in channel flows and highlight their effect in fluid transport in the turbulent channel.

Chapter 4 describes the extraction of 3d Lagrangian structures in an oceanic setting: the Benguela upwelling system and, especially, we study the structure of a 3d mesoscale eddy in terms of Lagrangian structures and their effect on transport.

In chapter 5 we study the effects of stirring of a biogeochemical tracer (dissolved O_2) by Lagrangian coherent structures in the Eastern Tropical South Pacific Oxygen Minimum Zone and how this stirring action changes with depth.

Chapter 6 is dedicated to the structure and evolution of a coastal cold water filament in the Iberian upwelling system. We extract 3d Lagrangian structures to identify the filament boundaries and analyze its transport properties.

In chapter 7 we draw general conclusions.

1.6

Acknowledgements

The author was financially supported by the Portuguese FCT (Foundation for Science and Technology) and by the Fundo Social Europeu (FSE/QREN/POPH) through the predoctoral grant SFRH/BD/63840/2009.

In addition, this work received support from the Ministerio de Economía y Competitividad (Spain) and Fondo Europeo de Desarrollo Regional through projects FISICOS (FIS2007-60327) and ESCOLA (CTM2012- 39025-C02-01) and from the CSIC Intramural project TurBiD.

General notions

This chapter collects concepts and notions used during the development of this work. They are mostly related to turbulent flows and dynamical systems theory. Physical oceanography topics were relegated to the different chapters that follow this one, introduced as necessary to the discussion. No claim is made of strict coherence of the material presented in this chapter or to any logic sequence in its presentation and personal preference weighted considerably in the choice of subjects.

The first topic that should be discussed is the difference between the Eulerian and Lagrangian perspective of fluid dynamics, because it is at the heart of this work and the base for all the others mentioned here.

Imagine that the reader is tasked with counting how many vehicles cross a bridge in a given day of the week; he/she can do it in two ways: in the first way by standing at the end of the bridge and simply count how many cars cross the road at that location; in the second way, by standing in the beginning of the bridge, stopping the next car that intends to cross it, getting in the car and riding in it until the end of the bridge; the reader will then exit the car and count it as one more car who crossed the bridge and fastly make it's way back to the beginning of the bridge to ride the next one. The first way is the Eulerian way because the reader observes what occurs in a particular position and time, while the second way is the Lagrangian way because he/she follows the object of interest and observes what happens along its path.

In fluid dynamics terms, in the Lagrangian perspective you follow fluid elements along their trajectories, while in the Eulerian perspective you observe the changes to flow variables at a fixed location in time and space.

CHAPTER 2. GENERAL NOTIONS

In the Lagrangian description of fluid flows, the particle motion is described by a system of ordinary differential equations (ODE's). The nature of the flow, from laminar to strongly turbulent, is determined by the right-hand side (RHS) of these ODE's, the dynamics. The Lagrangian view provides a natural link between fluid dynamics and dynamical systems due to the fact that in the Lagrangian description, the phase-space explored by the fluid particles is just the n -dimensional configuration space in which the fluid lives. Seen as a dynamical system, the fluid flow properties can be studied using concepts from dynamical systems theory.

Finally, a word of caution: consistency in notation throughout this chapter was impossible to achieve. The main reason for this is the different sources for the material presented here - mainly review papers and books - and the particular notation used therein. The other reason is that certain types of notations are better suited than others to illustrate certain concepts, especially when the topic under discussion relies heavily on tensor objects, so while boldface is used to denote vector and tensor objects, some expressions make use of index notation for clarity. Scalar quantities are denoted in normal face.

2.1

Fixed points and stability

A dynamical system of arbitrary dimension changes with time according to

$$\dot{x} = f(x(t), t) , \quad (2.1)$$

where t is the independent variable, x the state of the system and f a generally smooth function of position and time representing the forcing of the system. As time evolves the solution $x(t)$ will take values in a sequence that can be represented as a curve in the domain of the system called the phase-space.

If the forcing f is independent of time, the system is said to be autonomous. In this case, there are a special class of solutions that do not change, i.e., they do not trace a curve in phase-space and occupy the same position for all t . For this reason they are called fixed points x^* and we have $dx^*/dt = 0$. The configuration of phase-space in the vicinity of these fixed points turns out to be highly dependent on the nature of the fixed points. To see this, consider a small perturbation $y = x - x^*$ to x^* whose dynamics can be expressed as:

$$\dot{y} = \frac{d}{dt}(x - x^*) = \frac{d}{dt}(y + x^*) = f(y + x^*). \quad (2.2)$$

2.1. FIXED POINTS AND STABILITY

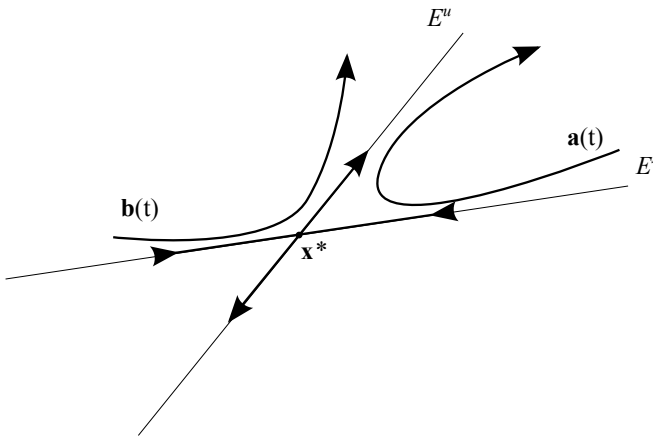


Figure 2.1: Stable E^s and unstable E^u invariant subspaces of a fixed point x^* in 2d phase-space. Trajectories $\mathbf{a}(t)$ and $\mathbf{b}(t)$ approach the fixed point along E^s and leave along E^u at exponential rates.

For the small perturbation y and neglecting higher order terms we may write

$$f(y + x^*) = f(x^*) + y \left. \frac{df}{dx} \right|_{x=x^*}, \quad (2.3)$$

and since $f(x^*) = 0$ we have that

$$\dot{y} = y \left. \frac{df}{dx} \right|_{x=x^*}, \quad (2.4)$$

where the derivative is computed at $x = x^*$, say Df^* . Then, the perturbation will evolve as $y(t) = y(0) \exp(Df^*t)$, exponentially growing or decaying if Df^* is positive or negative, respectively. The fixed point will then be named *stable* if it attracts nearby trajectories ($Df^* < 0$) and *unstable* if it repels nearby trajectories ($Df^* > 0$).

In two or more dimensions, Df^* is a constant $n \times n$ matrix with n eigenvalues e_1, \dots, e_n and eigenvectors $\mathbf{v}_1, \dots, \mathbf{v}_n$. The phase space can be represented as the direct sum of three subspaces E^s , E^u and E^c , where E^s spans the eigenvectors whose eigenvalues have negative real part, E^u spans those eigenvectors whose eigenvalues have positive real part and E^c spans the eigenvectors whose eigenvalues are purely imaginary [66]. Since solutions with initial conditions contained in E^s , E^u or E^c will remain there for all time, these subspaces are invariant subspaces under the linearized flow. Their continuations to the nonlinear regime are the so-called invariant manifolds. Solutions starting in E^s or its manifold approach $y = 0$

CHAPTER 2. GENERAL NOTIONS

asymptotically as $t \rightarrow +\infty$ so this subspace is called the *stable* subspace or manifold, while solutions starting in E^u or its manifold approach $y = 0$ asymptotically as $t \rightarrow -\infty$ so the E^u subspace is called the *unstable* subspace or manifold.

2.2

Conservation laws for fluid motions

Fluid motions, how complex they may be, are governed by simple principles, the most important being the conservation principle: *in the absence of sources or sinks of a quantity Q , the total amount of Q does not change.* This principle is usually expressed in the form of balance equations such as:

$$\frac{\partial Q}{\partial t} + \nabla \cdot (\mathbf{u}Q) = S_Q(\mathbf{x}, t) , \quad (2.5)$$

where the first term is the change of Q in a fixed position \mathbf{x} (the local rate of change), the second term is the amount of Q flowing through \mathbf{x} due to the velocity of the fluid \mathbf{u} and S_Q is the rate at which Q is produced or consumed at \mathbf{x} at time t . Thus, fluid motions can be defined by considering the conservation principle applied to the fluid's mass, momentum and internal energy. For incompressible fluids ($\nabla \cdot \mathbf{u} = 0$) with negligible changes in density, the following conservation equations are obtained

$$\frac{\partial \rho}{\partial t} + \mathbf{u} \cdot \nabla \rho = 0 , \quad (2.6)$$

$$\frac{\partial \mathbf{u}}{\partial t} + \mathbf{u} \cdot \nabla \mathbf{u} = -\frac{1}{\rho} \nabla p + \nu \nabla^2 \mathbf{u} + \mathfrak{F} , \quad (2.7)$$

$$\frac{DE}{Dt} = \frac{1}{\rho} k \nabla^2 T + \frac{\Upsilon}{\rho} . \quad (2.8)$$

In all these conservation laws, ρ is the fluid density and the left-hand side (LHS) represents the rate of change along the trajectory of a fluid particle, the material derivative $D()/Dt = \partial()/\partial t + \mathbf{u} \cdot \nabla()$. The first conservation equation expresses the conservation of unitary mass and states that local changes in density are due solely to fluid of different density being transported by the velocity field. The second conservation equation states that the rate of change of momentum per unitary mass along a particle trajectory is, in accordance with Newton's 2nd law, due to the sum of applied forces to the fluid particle: normal surface forces due to differential normal pressure ∇p ; tangential surface forces due to tangential stresses $\nu \nabla^2 \mathbf{u}$ and volume forces \mathfrak{F} . The coefficient ν is the kinematic viscosity

2.3. TURBULENT FLOWS

(the ratio between the fluid viscosity μ and density) $\nu = \mu/\rho$ and represents the diffusion of momentum due to molecular motions across the fluid element's surface. The energy equation states that the change in the fluid element's internal energy, E , along a trajectory is due to heat conduction across its boundaries (1st term of the RHS) and through viscous dissipation (2nd term of the RHS). Viscous dissipation always acts to increase the internal energy of the fluid [67]. This set of equations is termed the Navier-Stokes equations (NSE) and they are the cornerstone of modern fluid dynamical analysis. They are also extremely complex and not thoroughly understood: at the moment there is no rigorous global existence and uniqueness statement on the NSE *.

2.3

Turbulent flows

In spite of the difficulties presented by the NSE, they provide an accurate description of fluid flows that we observe in Nature. Given the tremendous variety of these latter, ranging from orderly and predictable to erratic and impossible to forecast, we can expect that these equations hold this vast richness of behaviors in their inner workings. To the simple flows we call laminar, while the more complex are named turbulent. There is a non-dimensional parameter Re —the Reynolds number —that determines the complexity of the flow. It is defined as the ratio between the typical magnitudes of the inertial effects and the viscous effects of the flow:

$$Re = \frac{UL}{\nu} . \quad (2.9)$$

When non-dimensionalized by characteristic scales of velocity U and length L , the momentum equation reads:

$$\frac{\partial \hat{\mathbf{u}}}{\partial \hat{t}} + \hat{\mathbf{u}} \cdot \nabla \hat{\mathbf{u}} = -\nabla \hat{p} + \frac{1}{Re} \nabla^2 \hat{\mathbf{u}} + \hat{\mathcal{F}} , \quad (2.10)$$

with primed variables made non-dimensional. The pipe flow experiments of Reynolds showed that when Re is small, the flow was laminar while higher Re resulted in turbulent motions in the pipe. The non-dimensional momentum equation (2.10) shows that turbulence is a phenomenon dominated by inertia since as $Re \rightarrow \infty$, the viscous term vanishes.

*There is a very non-negligible sum of \$ 1,000,000 waiting for the first man or woman that can produced such statement. Check the Millennium Prize at <http://www.claymath.org/millennium-problems/navier-stokes-equation/>

CHAPTER 2. GENERAL NOTIONS

Turbulent flows exhibit strong irregularities and are highly sensitive to initial disturbances. This character makes it difficult to obtain even approximate solutions to the NSE at high Re. Moreover, the spectrum of time and space scales occupied by flow phenomena increases with Re and so computational requirements are much more demanding for turbulent flows. Due to these obstacles, turbulent flows have been studied extensively through statistical analysis where characteristic values of the solutions and typical departures thereof are sought, instead of a complete description of all flow features. The process of extracting statistical information is called Reynolds averaging and it considers flow variables, say velocity \mathbf{u} , to be composed of a mean value $\bar{\mathbf{u}}$ and a fluctuating component $\mathbf{u}' = \mathbf{u} - \bar{\mathbf{u}}$ with $\overline{\mathbf{u}'} = 0$. Through this approach, an equation for the mean flow can be obtained (in tensor index notation for clarity):

$$\rho \bar{u}_j \frac{\partial \bar{u}_i}{\partial x_j} = \rho \bar{f}_i + \frac{\partial}{\partial x_j} (-\bar{p} \delta_{ij} + \mu S_{ij} - \overline{\rho u'_i u'_j}) , \quad (2.11)$$

where $S_{ij} = (\frac{\partial \bar{u}_i}{\partial x_j} + \frac{\partial \bar{u}_j}{\partial x_i})$. Except for the last term in the RHS of (2.11), the mean momentum equation contains the mean forcings by normal pressure, tangential stresses and mean body forces. The term $-\overline{\rho u'_i u'_j}$ is an additional forcing term that originates in the fluctuating part of the flow and represents the mean transport of turbulent momentum by the turbulence itself [68]. Additional insight to the effect of turbulent fluctuations on the mean, large-scale flow can be gained by looking at the equation for the mean kinetic energy of the flow, neglecting viscous terms:

$$\rho \bar{u}_j \frac{\partial}{\partial x_j} (\frac{1}{2} \bar{u}_i \bar{u}_i) = -\frac{\partial}{\partial x_j} (\bar{p} \bar{u}_j + \overline{\rho u'_i u'_j} \bar{u}_i) + \overline{\rho u'_i u'_j} S_{ij} . \quad (2.12)$$

Terms inside brackets in the RHS represent pressure work and redistribution of mean kinetic energy by turbulence. The last term of the RHS represents deformation work due to turbulent fluctuations and is almost always negative [68] so its effect is to remove kinetic energy from the mean flow.

Where does this energy go? Richardson [69] proposed the mechanism of the energy cascade whereby the flow is forced (energy injected in) at the large scales (mean flow scales), producing large eddies that break up into smaller ones that in turn break up into even smaller ones and so on so forth until an eddy size is reached where viscosity dominates and the kinetic energy of the turbulence is converted into heat by viscous dissipation.

This energy cascade involves a range of wavenumbers $k = 2\pi/l$ where l is the typical size of an eddy of a given scale. The lower bound to this range is given by the largest possible eddy size, determined by the size of the system L , so we'll have $k_{min} = 2\pi/L$. The energy cascade proceeds through k -space until it is arrested by

2.3. TURBULENT FLOWS

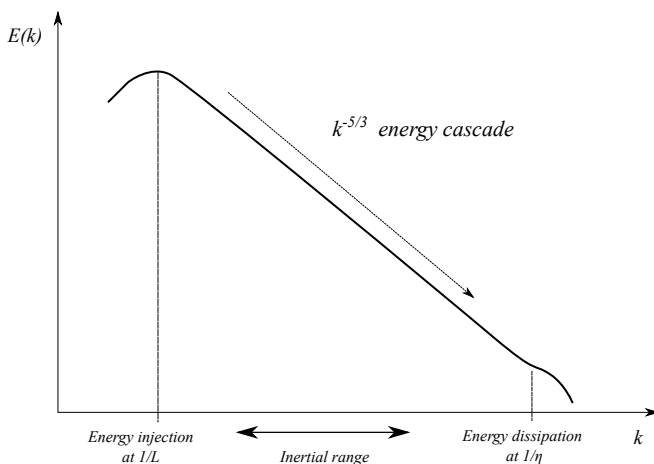


Figure 2.2: Energy cascade in 3d turbulence. $E(k)$ is the turbulent kinetic energy spectrum as function of wavenumber k . The large scale mean flow has characteristic length scale L and η is the length scale at which viscous dissipation of turbulent fluctuations occurs.

viscous dissipation. The physical parameters we can use to determine this scale of dissipation are the kinematic viscosity ν and the dissipation rate $\varepsilon = -dE'/dt$, where E' is the total kinetic energy of the turbulent fluctuations. A characteristic size of eddies at the dissipative end of the cascade is

$$\eta = (\nu^3/\varepsilon), \quad (2.13)$$

and the maximum possible wavenumber is $k_{max} = 2\pi/\eta$. A velocity scale can also be formed as $v = (\nu\varepsilon)^{1/4}$. At this scale, the Reynolds number is $Re = v\eta/\nu = 1$ and we conclude that viscous effects dominate rather than inertial ones. Note that k_{min} is determined by the nature of the system under consideration while k_{max} is determined by the properties ν and ε , so the ratio k_{max}/k_{min} can be made as large as desired and infinitely large for infinite Re .

Energy is determined by the lowest wavenumber and the dissipation rate by the highest wavenumber [70]. In between these two limits, the inertial range can be made as large as we want simply by increasing Re . In this inertial range, eddies of different size coexist in physical space. When two eddies interact the effects can be decomposed into (a) convection of one eddie by the other and (b) shearing of one eddie by the other. The first of these modes of interaction is not dynamically significant [71] while the second results in distortion of the eddies and transfer of energy to smaller disturbances. If the eddies differ considerably

CHAPTER 2. GENERAL NOTIONS

in size we may say that the second effect is very small and only the first mode, dynamically irrelevant, is present. We can therefore argue that eddy interaction is local in wavenumber space [71]. The combination of locality and averaging over several eddy turn-over times leads us to conclude that the energy cascade becomes independent of the actual mechanism that created turbulence and we can invoke an universality in the high wavenumber range of the energy spectrum of 3d turbulence [71].

Kolmogorov [72, 73] put forth these ideas in two hypotheses: that at sufficiently high wave numbers the energy spectrum depends only on k , ν and ε so that we should have:

$$E(k) = v^2 \eta f(k\eta) = \nu^{5/4} \varepsilon^{1/4} f(k\eta) , \quad (2.14)$$

where f is a function of universal form; and that $E(k)$ should become independent of the viscosity as Re is increased towards infinity which amounts to having

$$f(k\eta) = C(k\eta)^{-5/3} = C\nu^{-5/4} \varepsilon^{5/12} k^{-5/3} , \quad (2.15)$$

with C constant. Then we will have

$$E(k) = C\varepsilon^{2/3} k^{-5/3} , \quad (2.16)$$

in the limit $Re \rightarrow \infty$. In the case of large but finite Re , we can assume the existence of a range where $k_{min} \ll k \ll k_{max}$ in which $E(k)$ is independent of viscosity and has a $k^{-5/3}$ slope. Although Kolmogorov's theory is based on dimensional arguments, it has been proven to be in good agreement with experiments for the 5/3 energy spectrum.

The actual physical mechanism by which energy is transferred to smaller scales is a topic of great importance. Vortex stretching is widely considered to be such mechanism [71]. Turbulent flows exhibit strong vorticity fluctuations. A conservation equation for vorticity $\boldsymbol{\omega}$ can be obtained by taking the curl of the momentum equation (2.7):

$$\frac{D\boldsymbol{\omega}}{Dt} = \boldsymbol{\omega} \cdot \nabla \mathbf{u} + \nu \nabla^2 \boldsymbol{\omega} . \quad (2.17)$$

The last term in the RHS of (2.17) represents molecular diffusion of vorticity just as in (2.11) there is a term for molecular diffusion of momentum ($\nu \nabla^2 \mathbf{u}$). The first term of the RHS of (2.17) has however no counterpart in the momentum balance equation and represents the interaction of vorticity with the velocity gradients in physical space. In the inertial range, where scales of motion are much larger than $1/k_{max}$, viscosity effects may be neglected and we can consider that vorticity moves with the fluid [67]. As the velocity gradients will act, in

2.3. TURBULENT FLOWS

average, to stretch fluid line elements [71], vortex lines will also stretch on average. Then, a stretched vortex line, by conservation of angular momentum, will increase its angular velocity as it's width is reduced and the energy associated with the reduced length scale will increase. Therefore we observe a transfer of energy from large to small scales in turbulence, whenever the vortex stretching mechanism is present.

2.3.1 Two-dimensional turbulence

Turbulence in two-dimensional (2d) flows is another manifestation of irregular fluid motion. Rigorously, it is never realized in nature or the laboratory where there is always a certain degree of 3-dimensionality. Although unrealistic in the strict sense, aspects of 2d turbulence manifest themselves in the physical world. Of special interest to this work, we cite the case of nonlinear, chaotic, large-scale motions in the oceans [74, 75].

In 2d, vorticity is normal to the plane of the flow, hence the vortex stretching term disappears for the conservation equation for vorticity (2.17) and in the inviscid limit $\nu \rightarrow 0$, vorticity is conserved along fluid particle trajectories. In 2d homogeneous or periodic systems the total energy changes as [76]:

$$\frac{DE}{Dt} = -\nu Z , \quad (2.18)$$

where $Z = \langle \omega^2 \rangle$ is the enstrophy. Since vorticity does not diverge in the inviscid limit there is no viscous dissipation of energy, contrary to the case in 3d turbulence. Thus a direct energy cascade of energy cannot exist in 2d turbulence. On the other hand, enstrophy changes as

$$\frac{DZ}{Dt} = -\nu \langle (\nabla \omega)^2 \rangle , \quad (2.19)$$

and in the inviscid limit there can still be dissipation of Z at the small scales since $(\nabla \omega)^2$ will be amplified by distortion due to the velocity field [76] that generates thin filaments of vorticity, enhancing $\nabla \omega$. So, in 2d, a direct cascade of enstrophy from the large scales to the small scales should be expected [77].

For a $E(k) \sim k^{-\alpha}$, we return to the Kolmogorov scaling (2.16). For the direct enstrophy cascade range, the enstrophy flux is estimated to be $\Sigma(k) \sim \lambda_k k^3 E(k)$. A constant enstrophy flux implies

$$E(k) = C' \varepsilon_Z k^{-3} , \quad (2.20)$$

where ε_Z is the dissipation of enstrophy by viscosity and C' is a dimensionless constant [78].

CHAPTER 2. GENERAL NOTIONS

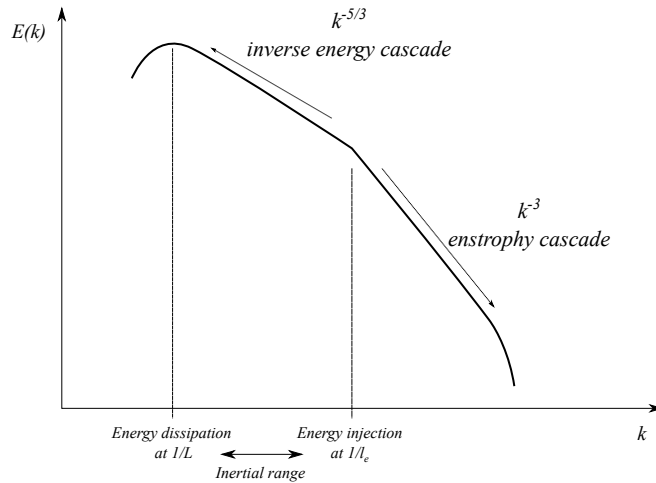


Figure 2.3: Energy and enstrophy cascade in 2d turbulence. $E(k)$ is the turbulent kinetic energy spectrum as function of wavenumber k . Energy is supplied at $k = 1/l_e$ and dissipated at the large scale mean flow has $k = 1/L$ by friction.

2.4

Coherent structures

The established view of turbulence as a purely random phenomenon implied that solely through statistical methods could it be understood. Visual observations however, brought forward the concept of coherent structures that, it seemed, gave turbulence a certain degree of deterministic organization. In this novel perspective of turbulent phenomena, coherent structures appear as motions with apparent order in the sense of a correlated and concentrated dynamic quality [79]. This correlation in time and space can also be expressed as *existing for long enough time to allow its observation* [80]. As for the dynamical quality, vorticity ω has been used most extensively [81, 82], but any fundamental flow variable that exhibits this kind of correlation may be used [83].

From visual observations, criteria to define a coherent structure were derived [79]:

- (a) Coherent structures exhibit several scales, the largest comparable to the characteristic dimension of the system.
- (b) Are flow-specific and indirectly related to boundary conditions.

2.4. COHERENT STRUCTURES

- (c) Exhibit recurrent patterns with a life span at least the average passage time of the structure.
- (d) Possess a high degree of organization in their structure and dynamics.
- (e) Appear quasi-periodically at best and typically are stochastically intermittent.
- (f) Show strong similarities with corresponding structures of the (previous) laminar-turbulent transition.

The initial formation mechanism is thought to be a flow instability and coherent structures may be viewed initially as instability modes of the basic flow [79]. Vorticity is the dynamical variable more frequently involved in the identification of coherent structures, so it is unsurprising to find that the taxonomy of coherent structures is mainly populated by vortex type structures, as those in Figure 2.4. In simple, canonical flows a reduced set of elementary coherent structures would be composed of [79]: line vortex, ring vortex, hairpin vortex and helical vortex.

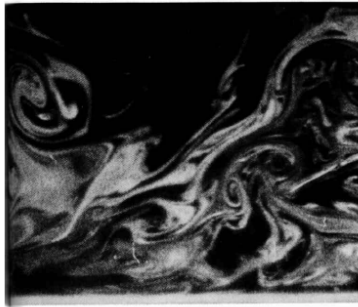
It is well known that coherent structures determine mixing, heat transfer and other fluid phenomena in turbulent flows. Estimates of the fraction of total turbulent energy attributable to coherent structures varies between 10 and 25 percent depending on the type of flow [79].

2.4.1 Coherent structures in 2d turbulence

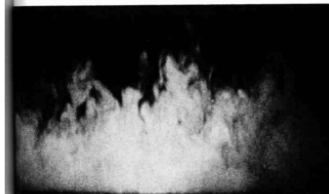
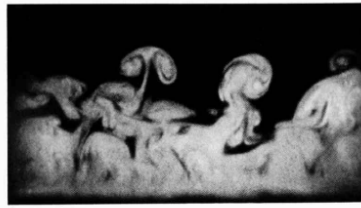
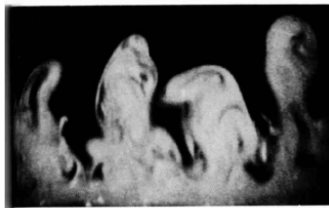
In an extended range of conditions, the flow structure of 2d turbulence has its vorticity concentrated in a small fraction of the spatial domain of the system. These structures of correlated vorticity have typical long lifetimes when compared with the characteristic eddy turnover times, persisting under advection by the mean flow [85]. These coherent vortices contain most of the energy of the system and their appearance is connected to the inverse energy cascade from small to large scales [78].

Two-dimensional turbulence is then characterized by a background of random, weakly energetic fluctuations, disturbed by strong coherent vortices and thin vorticity filaments (Figure 2.5).

CHAPTER 2. GENERAL NOTIONS



162. "Typical eddy" in a turbulent boundary layer. Oil fog is illuminated by a sheet of laser light to show the lower two-thirds of a turbulent boundary layer in side view. The vortex-ring structure just below and to the right of center, which resembles a sliced mushroom leaning left, is an example of what Falco has called a "typical eddy." It scales on wall variables (figure 161) rather than on the boundary-layer thickness. Photograph by R. E. Falco



163. Oblique transverse sections of a turbulent boundary layer. The flow is viewed head-on, with smoke illuminated by a sheet of light that is inclined 45° downstream from the wall on the left and 45° upstream on the right.

The Reynolds number based on momentum thickness is 600 in the upper pair of photographs and 9400 below. Head & Bandyopadhyay 1981

Figure 2.4: Coherent structures in an 3d turbulent boundary layer (from [84]).

2.4. COHERENT STRUCTURES

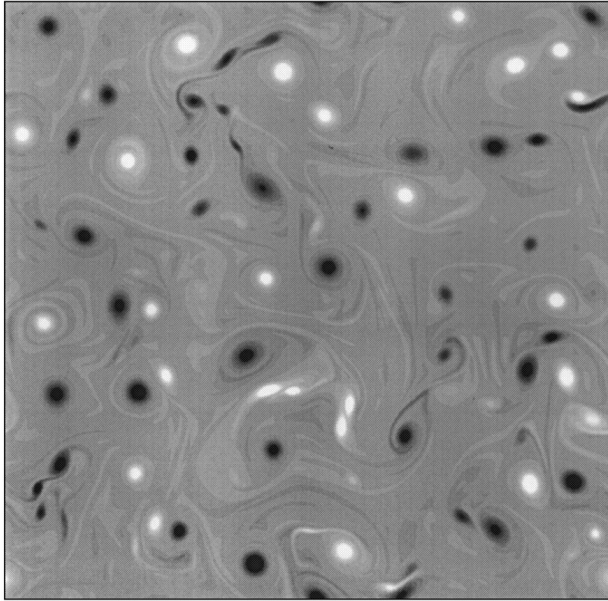


Figure 2.5: Vorticity field from a numerical simulation of freely decaying two-dimensional turbulence (from [78]). Bright and dark tones indicate negative and positive vorticity respectively.

Dispersion in turbulent flows

In a statistically homogeneous, stationary turbulent flow, the probability of finding a particle at $x_1 = x_0 + X$ at time $t_1 = t_0 + T$ can be described by the single particle displacement probability density function (pdf) $Q(X, t)$. The absolute dispersion is defined as the second moment of Q :

$$\overline{X^2}(t) = \int X^2 Q(X, t) dX . \quad (2.21)$$

The time derivative of $\overline{X^2}(t)$ is the absolute diffusivity

$$\kappa_a(t) = \frac{1}{2} \frac{d}{dt} \overline{X^2}(t) = \overline{X(t)u(t)} = \int_0^t \overline{u(X, t)u(X, \tau)} d\tau , \quad (2.22)$$

which is the integral of the velocity autocorrelation [49]. Another form of the absolute diffusivity is $\kappa_a(t) = \overline{(u(t) - \bar{u})^2} \int_0^t R(\tau) d\tau$, which allows us to write the absolute dispersion as:

$$\overline{X^2}(t) = 2 \overline{(u(t) - \bar{u})^2} \int_0^t (t - \tau) R(\tau) d\tau , \quad (2.23)$$

where $R(\tau)$ is the normalized velocity autocorrelation. At initial times $R(\tau) \sim 1$ and the absolute dispersion grows quadratically in time as

$$\lim_{t \rightarrow 0} \overline{X^2}(t) = \overline{(u(t) - \bar{u})^2} t^2 . \quad (2.24)$$

In the limit of large times we have

$$\lim_{t \rightarrow \infty} \overline{X^2}(t) = 2 \overline{(u(t) - \bar{u})^2} t \int_0^\infty R(\tau) d\tau - \int_0^\infty \tau R(\tau) d\tau , \quad (2.25)$$

and the absolute dispersion grows linearly in time.

If we consider instead the average separation between particle pairs in turbulence, we face the problem of relative dispersion. Analogous to absolute dispersion, relative dispersion is measured as:

$$\overline{Y^2}(t) = \int Y^2 P(Y, t) dY , \quad (2.26)$$

where $P(Y, t)$ is the separation probability of two particles separated by Y at time t . The relative diffusivity is again the time derivative of the dispersion:

$$\kappa_r(t) = \frac{1}{2} \frac{d}{dt} \overline{Y^2}(t) = \overline{Y(t)\delta u(t)} , \quad (2.27)$$

2.6. CHAOTIC ADVECTION

where $\delta u = dY(t)/dt$ is the pair separation velocity. For initial times the pair velocity difference is constant if the particles are very close and the diffusivity increases linearly in time [49]. For large times, particle velocities will be uncorrelated and relative dispersion will grow at twice the absolute diffusivity.

For intermediate times, pair velocities are correlated and we'll have, for an Eulerian turbulence energy spectrum $E(k) \propto k^{-\alpha}$ [86]:

$$\overline{\delta u(Y)^2} \propto Y^{\alpha-1}, \quad 1 < \alpha < 3, \quad (2.28)$$

and the diffusivity will scale as $\kappa_r \propto Y^{(\alpha+1)/2}$. In the inertial range of 2d and 3d turbulence we have $\alpha = 5/3$ and we find that

$$\overline{Y^2}(t) \propto \varepsilon t^3, \quad \kappa_r \propto \varepsilon^{1/3} Y^{4/3}, \quad (2.29)$$

where ε is the energy dissipation rate. The cubic dispersion law was predicted by Richardson [87] and is named *Richardson dispersion*. In 2d turbulence there is an additional range, the direct enstrophy cascade with $\alpha = 3$, we find that, on dimensional grounds [88]

$$\overline{Y^2}(t) \propto \exp(A\zeta^{1/3}t), \quad \kappa_r \propto \overline{Y^2}, \quad (2.30)$$

where ζ is the enstrophy dissipation rate. In 2d turbulence, one will find exponential separation in the direct enstrophy cascade and Richardson dispersion in the inverse energy cascade.

2.6

Chaotic advection

The motion of the fluid changes the arrangement of the fluid elements and hence of the properties that these elements carry. To this process we call advection. Considering a scalar property q in incompressible fluid, the conservation principle reads (see section 2.2):

$$\frac{\partial q}{\partial t} + \mathbf{u} \cdot \nabla q = S_q(\mathbf{x}, t). \quad (2.31)$$

The LHS of (2.31) is just the material derivative of q and so the advection process can be described as $Dq/Dt = S_q$. During fluid motion particles carry an amount of the scalar q that changes according to the agencies that produce or consume q , $S_q(\mathbf{x}, t)$. The particular changes of q during time evolution of the flow will therefore depend on the trajectory $\mathbf{x}(t)$ of the fluid elements carrying q that will visit different regions of the fluid domain.

CHAPTER 2. GENERAL NOTIONS

In 2d stationary flow, the velocity \mathbf{u} can be represented by a scalar streamfunction ψ such that

$$\mathbf{u} = (u, v) = \left(\frac{\partial \psi}{\partial y}, -\frac{\partial \psi}{\partial x} \right), \quad (2.32)$$

and we recognize the form of one-degree of freedom Hamiltonian dynamics where the streamfunction ψ plays the role of the Hamiltonian. In these type of flows, streamlines are lines of constant ψ . The rate of change of ψ along a particle trajectory is its material derivative

$$\frac{D\psi}{Dt} = \mathbf{u} \cdot \nabla \psi = \frac{\partial \psi}{\partial y} \frac{\partial \psi}{\partial x} - \frac{\partial \psi}{\partial x} \frac{\partial \psi}{\partial y} = 0. \quad (2.33)$$

If ψ does not change along particle trajectories, then particles move along the lines of constant ψ , i.e. they move along streamlines, which are smooth. In time dependent flows, ψ is no longer conserved along trajectories and fluid particles are no longer restricted to motion along streamlines. In this regime, the KAM theorem assures the existence of regular islands where particle trajectories are smooth. These regular islands are surrounded by chaotic regions where particle trajectories are aperiodic and chaotic. The regular islands are surrounded by invariant surfaces that form barriers to the mixing between chaotic regions. As the time dependence strengthens, these regular islands become scarce and eventually the chaotic regions grow until occupying most of the fluid domain and fluid trajectories fill the entire domain [89].

In 3d flows, the streamfunction does not exist and particles are not forced to flow along streamlines even in time-independent flows. Thus chaotic particle motion can exist in the simplest of laminar flows.

2.7

Mixing

A more complete expression for the time evolution of a scalar q in fluid flow is obtained by adding the diffusive flux of q due to molecular motions to (2.31). The diffusive flux is usually modeled by Fick's law where diffusion is proportional to the scalar gradient ∇q . We assume, for simplicity, that the diffusion coefficient K is constant. We then obtain (in index notation):

$$\frac{\partial q}{\partial t} + u_j \frac{\partial q}{\partial x_j} = K \frac{\partial^2 q}{\partial x_j \partial x_j} + S_q. \quad (2.34)$$

2.7. MIXING

During the evolution of the flow, q will be advected by the velocity field and its content in a fluid element will change due to local diffusive flux and by the possibly various sources and sinks contained in the S_q term. When $K = 0$ and $S_q = 0$ we obtain $Dq/Dt = 0$ and the scalar q is conserved along fluid particle trajectories. Either way (conserved or not conserved during time evolution), the observation of the field q in physical space will reveal patterns of high or low q in the fluid domain that themselves evolve with time. The shape and complexity of these regions is without a doubt related to the processes described by (2.34).

Connected to the shape of these patterns in the flow is the time evolution of the gradient of q . To obtain a evolution equation for $q_i = \partial q / \partial x_i$, we differentiate (2.34) with respect to x_j to obtain (neglecting the source term):

$$\frac{\partial q_i}{\partial t} + u_j \frac{\partial q_i}{\partial x_j} + q_j \frac{\partial u_j}{\partial x_i} = K \frac{\partial^2 q_i}{\partial x_j \partial x_j}. \quad (2.35)$$

The gradient norm evolution is obtained by multiplying (2.35) by q_i and, after collecting similar terms, we have [64]:

$$\frac{D}{Dt} q^2 + \frac{\partial u_j}{\partial x_i} q_i q_j = K \left(\frac{\partial^2 q^2}{\partial x_i \partial x_i} - \frac{\partial q_i}{\partial x_j} \frac{\partial q_j}{\partial x_j} \right), \quad (2.36)$$

where $q^2 = q_i q_i / 2$.

The evolution of a tracer advected and diffused by a flow was studied by Eckart [90] who proposed a three phased evolution for q^2 : in the initial phase, the dynamics is dominated by the advection of the scalar gradient norm, represented by the first term of the LHS of (2.36). In this phase the scalar field is gently distorted by the fluid's motions. In the second phase, called the "stirring" phase by Eckart, the dominant term is $\partial u_j / \partial x_i q_i q_j$ and the scalar gradient is strained and elongated by the velocity gradient field. To see this more clearly we neglect diffusion in this second phase and recall that since q is conserved along trajectories, these are isolines of q and we can define $\nabla q = dq/ds \mathbf{n}$, where dq is the difference in q between two neighboring isolines, ds the distance between those isolines and \mathbf{n} is a unit vector in the direction normal to the isoline of q . The gradient norm is $\rho = dq/ds$ and since dq is constant the change in the gradient norm obeys

$$\frac{1}{\rho} \frac{D\rho}{Dt} = -\frac{1}{ds} \frac{D}{Dt}(ds), \quad (2.37)$$

where we stress that this relations hold along a fluid particle trajectory. Integration of (2.37) yields:

$$\rho(t) = C_2 ds(t)^{-1} = C_2 e^{\lambda t}, \quad (2.38)$$

CHAPTER 2. GENERAL NOTIONS

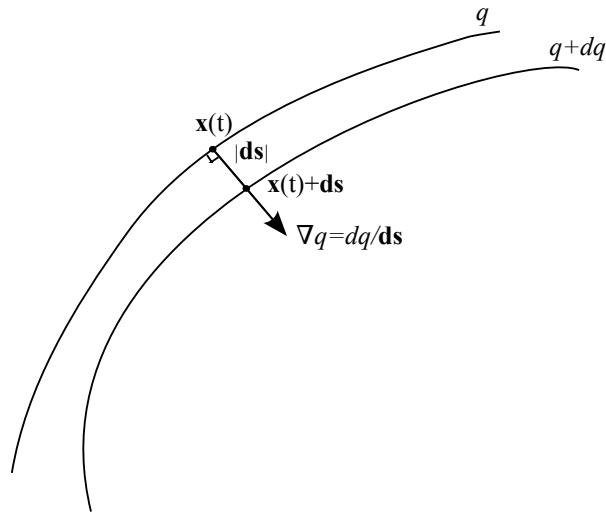


Figure 2.6: Gradient of a conserved scalar q . The scalar isolines q and $q + dq$ are also material lines. As $d\mathbf{s}$ grows or decays the norm of the scalar gradient decays or grows. Fast growth of the gradient norm is found when particles diverge exponentially in the direction normal to the gradient orientation.

where C_2 is a constant. We recall that for long enough time (but not too long as to allow diffusive effects to become dominant) the growth of infinitesimal line segments is exponential with rate equal to λ_1 (see section 2.8).

The third and final phase of the evolution of the scalar gradient norm is achieved when the scalar gradient has been intensified by the stretching action of the velocity gradients up to a point when the diffusive terms in (2.36) take over as dominant. At this stage, diffusion starts to smooth the scalar field and mixing occurs. A estimate of the width of q filaments when diffusion starts to become dominant, the arrest scale, is $w_a \propto (K/\lambda_1)^{1/2}$ [91].

Stretching and alignment in turbulent flows

In three-dimensional (3d) space $\mathbf{x} = (x, y, z)$, the trajectories of the fluid particles are governed by the following dynamics:

$$\begin{aligned}\dot{x} &= u(x, y, z, t) , \\ \dot{y} &= v(x, y, z, t) , \\ \dot{z} &= w(x, y, z, t) ,\end{aligned}\tag{2.39}$$

where $\mathbf{u} = (u, v, w)$ is the velocity field. Sufficient regularity of \mathbf{u} ensures that solutions to (2.39) exist and are unique. Another requirement on \mathbf{u} , specific to the work here presented, is that the flow should be volume preserving, i.e., incompressible:

$$\nabla \cdot \mathbf{u} = 0 .\tag{2.40}$$

Solutions to (2.39) are described by the flow map $\phi_t^T : \mathbf{x}(t) \mapsto \mathbf{x}(t+T)$, a mapping that has as input the initial location of a particle at time t and whose output is the position of the particle at time $t+T$.

The behavior of nearby trajectories is determined by the tangent map, the linearization of the flow about the trajectory of interest. In fluid dynamics, the tangent map is the velocity gradient tensor of the flow \mathbf{A} :

$$A_{ij} = \frac{\partial u_i}{\partial x_j} ,\tag{2.41}$$

The importance of \mathbf{A} in fluid dynamics is related to its symmetrical and anti-symmetrical parts:

$$A_{ij} = \frac{1}{2}S_{ij} + \frac{1}{2}\Omega_{ij} = \frac{1}{2}\left(\frac{\partial u_i}{\partial x_j} + \frac{\partial u_j}{\partial x_i}\right) + \frac{1}{2}\left(\frac{\partial u_i}{\partial x_j} - \frac{\partial u_j}{\partial x_i}\right).\tag{2.42}$$

The rate-of-strain tensor \mathbf{S} has three real eigenvalues s_i that in incompressible flow must add to zero. When ordered by value, $s_1 \geq 0$, $s_3 \leq 0$ and s_2 can have either sign. The anti-symmetric part, the vorticity tensor $\mathbf{\Omega}$, has two complex conjugate, imaginary eigenvalues and one zero eigenvalue whose eigenvector is half the vorticity vector $\omega_k = -1/2\varepsilon_{ijk}\Omega_{ij}$. In an Eulerian frame, motions in the vicinity of a point are composed by elongation and rotation as determined by the rate-of-strain and vorticity tensors.

In dynamical systems studies, the symmetrical and anti-symmetrical components of \mathbf{A} are rarely considered separately and, essentially, all anti-symmetrical information is ignored [92]. Instead, attention is drawn to the evolution of small

CHAPTER 2. GENERAL NOTIONS

perturbations $\delta\mathbf{x}$ to \mathbf{x} , that, using (2.39), after Taylor expansion about \mathbf{x} and neglecting higher order terms, are governed by

$$\delta\dot{\mathbf{x}} = \mathbf{A} \cdot \delta\mathbf{x} , \quad (2.43)$$

where $\delta\mathbf{x}$ and \mathbf{A} are evaluated along $\mathbf{x}(t)$. The linear, first order ODE (2.43) has as fundamental matrix solution the tangent flow map [93], say from 0 to t :

$$\mathbf{M}(t, 0; \mathbf{x}_0) = \nabla_{\mathbf{x}_0} \phi_0^t(\mathbf{x}_0) , \quad (2.44)$$

such that $\delta\mathbf{x}(t) = \mathbf{M}(t, 0; \mathbf{x}_0)\delta\mathbf{x}(0)$. The norm of the perturbation will grow as *

$$\|\delta\mathbf{x}(t)\|^2 = \|\mathbf{M}(t, 0; \mathbf{x}_0)\delta\mathbf{x}(0)\|^2 = \delta\mathbf{x}(0)\mathbf{M}^T(t, 0; \mathbf{x}_0)\mathbf{M}(t, 0; \mathbf{x}_0)\delta\mathbf{x}(0) . \quad (2.45)$$

We can define a mean rate of growth of the perturbation as:

$$\lambda_\infty = \lim_{t \rightarrow \infty} \frac{1}{t} \ln \frac{\|\delta\mathbf{x}(t)\|}{\|\delta\mathbf{x}(0)\|} . \quad (2.46)$$

This is the largest Lyapunov exponent and if it is positive, it implies exponential growth of perturbations hence great sensitivity to initial conditions. Oseledec's theorem [94] proves that for all initial conditions, except a set of measure zero, (2.46) exists.

The tensor $\mathbf{M}^T\mathbf{M}$ is symmetric and positive-definite, hence its eigenvectors form an orthonormal set and its eigenvalues are real and positive. In n -dimensional space, there are n pairs of eigenvalues/vectors σ_i/ξ_i and if $\delta\mathbf{x}_0$ is initially aligned with ξ_i , $\delta\mathbf{x}_0 = \delta_0\xi_i$, then it will grow as $\delta\mathbf{x}(t) = \mathbf{M}\delta_0\xi_i$ and the length at time t will be:

$$\|\mathbf{M}\delta_0\xi_i\| = (\delta_0\xi_i^T\mathbf{M}^T\mathbf{M}\delta_0\xi_i)^{1/2} = \delta_0(\sigma_i)^{1/2} . \quad (2.47)$$

Returning to the mean growth rate and taking the limit $\delta_0 \rightarrow 0$ so that the linearization is valid for arbitrary long time we have

$$\lambda_i = \lim_{t \rightarrow \infty} \lim_{\delta_0 \rightarrow 0} \frac{1}{t} \ln \left(\frac{\|\mathbf{M}\delta_0\xi_i\|}{\delta_0} \right) = \lim_{t \rightarrow \infty} \lim_{\delta_0 \rightarrow 0} \frac{1}{2t} \ln \sigma_i . \quad (2.48)$$

We can therefore define a ordered set of non-increasing Lyapunov exponents λ_i , that in general will depend, on the initial condition \mathbf{x}_0 , except for ergodic systems where it is the same for all initial conditions except in a set of measure zero [94]. The λ_i can be positive or negative, but for incompressible flows, they must sum to zero. In 3d, if there are non-zero λ_i then $\lambda_1 > 0$, $\lambda_3 < 0$ and λ_2 can be either —a familiar result already encountered for the eigenvalues of the rate-of-strain

* $\mathbf{M}^T\mathbf{M}$ is usually referred to as the Cauchy-Green tensor

2.9. NON-ASYMPTOTIC LYAPUNOV EXPONENTS

tensor —whereas in 2d the λ_i must be $\lambda_1 = -\lambda_2$. This last result implies that there will be a direction along which there is elongation ξ_1 and contraction along ξ_2 in order to preserve mass (area in this case).

When $\delta\mathbf{x}_0$ is not directed along any of the ξ_i , it can nevertheless be expressed by a sum of projections in to each of the eigendirections as $\delta\mathbf{x}_0 = \sum_i \alpha_i \xi_i$ and its evolution will be given by

$$\delta\mathbf{x}(t) = \sum_i \alpha_i \mathbf{M}\xi_i . \quad (2.49)$$

The vectors $\mathbf{M}\xi_i$ will grow in time as $e^{\lambda_i t}$ so after long enough time (2.49) will be dominated by the largest positive Lyapunov exponent λ_1 and, independently of the initial orientation of $\delta\mathbf{x}(t)$, the perturbation will be aligned with ξ_1 and will grow exponentially as $e^{\lambda_1 t}$ and we then may write $\lambda_\infty \sim \lambda_1$.

2.9

Non-asymptotic Lyapunov exponents

The Lyapunov exponents defined above characterize the asymptotic behavior of infinitesimally separated particles in a fluid system. However most of our observations occur on finite time intervals and at finite spatial scales. Thus the use of asymptotically defined measures is problematic. In addition, for ergodic systems, the leading Lyapunov exponent is constant almost everywhere, fact that does not provide a local view of stretching and alignment in turbulent flows. To overcome these shortcomings, non-asymptotic variants of the classic Lyapunov exponent λ_∞ were introduced: the finite-time and finite-size Lyapunov exponents.

2.9.1 The finite-time Lyapunov exponent (FTLE)

The finite-time Lyapunov exponent (FTLE) measures the stretching rate of infinitesimal material line segments in a finite time interval $[t, t + \Delta t]$ under the evolution of the flow given by the flow map $\phi_t^{t+\Delta t}(\mathbf{x})$. By removing the asymptotic time limit in (2.48) we obtain the expression for the FTLE:

$$\lambda(\Delta t; \mathbf{x}, t) = \lim_{\delta_0 \rightarrow 0} \frac{1}{2\Delta t} \ln \sigma_1 , \quad (2.50)$$

where σ_1 is the maximum eigenvalue of the $\mathbf{M}\mathbf{M}^T$ tensor, computed for the interval $[t, t + \Delta t]$. The FTLE depends on the initial condition so when computed for a

CHAPTER 2. GENERAL NOTIONS

domain D we obtain a map of FTLE showing regions with different rates of stretching during evolution of the flow between t and $t + \Delta t$.

The FTLE is distributed around a mean value that is none other than the asymptotic Lyapunov exponent and as the integration time increases the FTLE distribution approaches this maximum [89]. Note that in the calculation of (2.50) Δt should be large enough to allow the alignment with the principal eigenvector of the finite-time Cauchy-Green tensor to occur.

2.9.2 The finite-size Lyapunov exponent (FSLE)

The FTLE considers infinitesimal perturbations so it still has a asymptotic character. In order to study non-asymptotic dispersion processes such as stretching at finite scales and bounded domains, the finite size Lyapunov Exponent (FSLE) was introduced [52, 95, 96]. It is defined as:

$$\lambda(d_0, d_f; \mathbf{x}, t) = \frac{1}{\tau} \log \frac{d_f}{d_0}, \quad (2.51)$$

where τ is the time it takes for the separation between two particles, initially d_0 , to reach a value d_f . In addition to the dependence on the values of d_0 and d_f , the FSLE depends also on the initial position of the particles and on the time of deployment, as was the case with the FTLE.

An important aspect of the FSLE is its scale dependence. The growth of non-infinitesimal perturbations δ is governed by nonlinearity and the growth rate is scale-dependent [95, 97]. Thus for a fixed amplification ratio $r = d_f/d_0 > 1$ and averaging over many particle pairs we find the following regimes for $\lambda(d_0, r)$ [98]:

1. In the limit $d_0 \rightarrow 0$, the FSLE tends to λ_∞ .
2. In the case of standard diffusion with linear growth of dispersion, $\lambda(d_0, r) \sim d_0^{-2}$.
3. When advection is relevant, correlations persist for long time and $\lambda(d_0, r) \sim d_0^{-\alpha}$, with $\alpha > -2$.
4. When $\lambda(d_0, r) = \text{constant}$ over a range of d_0 we observe exponential separation between trajectories.

The FSLE is a more convenient measure for the case of bounded flows because characteristic spatial scales are more direct to identify than temporal ones. The FSLE has been shown to be robust with respect to noisy or poorly resolved velocity fields [99].

2.10. LAGRANGIAN COHERENT STRUCTURES (LCS)

2.10

Lagrangian coherent structures (LCS)

In turbulent flows, coherent structures tend to emerge. These are dynamic regions where a flow quantity exhibits a high degree of correlation. In 3d turbulence, coherent structures usually take the form of vortical structures of various shapes. In 2d turbulence, coherent structures are identified with axisymmetric vortices embedded in a background of weak turbulence. In between these vortices, thin filaments of concentrated vorticity exist.

The Eulerian approach to coherent structures consists in the partition of the flow field in regions with coherently distinct distributions of vorticity or other dynamical quantities, e.g., regions where rotation dominates over strain and regions where the opposite occurs. While allowing for systematic utilization, the structures so deduced do not reveal much of the underlying fluid motion, since these criteria are not conserved along the trajectories of the fluid elements.

The Lagrangian view, on the other hand, looks directly at the behavior of the trajectories and thus is able to provide a more accurate view of fluid motions. This is an important point because, as seen in the earlier in this chapter, fluid motions induced stirring in scalar fields that will eventually lead to enhanced mixing of these quantities, a process that supports important phenomena in the natural as in the technical world.

2.10.1 Lagrangian view of coherent structures

Visualizations of densely populated patches of passive particles in 2d turbulence leads to the observation of distinct behaviors: continued elongation and thinning of initially thick blobs of particles; coherent rotation of particle patches or simple, correlated, translational motions of particles. From observations of this kind of coherent motions, distinct Lagrangian dynamical regions can be deduced:

1. Local stretching in the flow appears to happen across coherent structure boundaries through divergence of nearby particles.
2. Thinning and folding appears to happen along coherent structure boundaries, as particles follow the curved boundaries

The first behavior is related to instability of particle trajectories due to which divergence occurs while the second resembles the behavior of particle trajectories converging towards an unstable manifold of the flow. For this reason coherent

CHAPTER 2. GENERAL NOTIONS

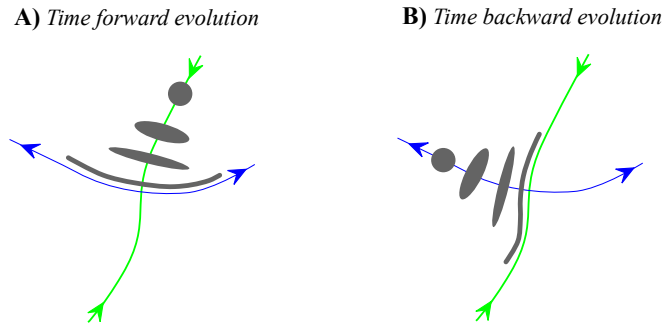


Figure 2.7: Time evolution of a fluid patch (gray) in the vicinity of attracting (blue) and repelling (green) coherent structures. A) Forward in time. B) Backward in time. Arrows indicate forward in time direction of trajectories *on* the coherent structure.

structures, in a Lagrangian view, can be seen as material lines that create smaller tracer scales through stability or instability [100].

Since stability in forward time is equivalent to instability in backward time, the coherent structures in the Lagrangian view can be classified as unstable in the two time directions (Figure 2.7): the forward time unstable, in forward time will *attract* nearby fluid that will thin and fold along them; the backward time unstable will, in backward time, also *attract* nearby fluid that will thin and fold along them. So a backward time integration will reveal attracting coherent structures while a forward time integration will reveal repelling coherent structures.

Analytic criteria for the identification of such structures were derived for flows in 2d [100] and 3d [63]. These criteria were based firstly on the computation of the time interval during which a material surface would be stable or unstable, coherent structures being those that maximized this measure (the hyperbolicity time approach). The criteria involved the computation of the invariants of the velocity gradient along particle trajectories [100]. Another alternative criteria put forth [63] was the identification of coherent structures with the local extrema of the FTLE field. The rationale for this criteria is that if coherent structures attract or repel particles for the longest in the flow, then, the net growth of a disturbance normal to them should be the largest during the time interval of interest. Since the FTLE (λ_1 for a finite-time interval, see section 2.8) measures the growth rate of disturbances then maximal disturbance growth should appear under the maxima of the FTLE field. An immediate advantage of the FTLE approach over the hyperbolicity time method was that the former could be computed directly

2.10. LAGRANGIAN COHERENT STRUCTURES (LCS)

from particle trajectories, without the need to compute the velocity gradient tensor.

Relationships of Lagrangian coherent structures (LCS) with FTLEs were then established [101, 102]. These relationships state that LCS can be identified with the ridges (generalized maxima) of the FTLE field. Furthermore they state that the flux through the LCS is inversely proportional to the strength of the ridge and to the integration time of the FTLE field calculation. This flux is shown to be small and the LCS extracted as the ridges of FTLE fields are considered to be almost material-like surfaces. This identification has become widely used in the field although it should be mentioned that there are other more precise definitions of LCS [56, 103, 104], that consider LCS to be exact material surfaces admitting zero flux across them.

In this work, we used instead finite-size Lyapunov exponents (FSLEs), which are a measure of the separation rate of fluid particles between two given distance thresholds (see section 2.9.2) to identify LCS. Although a rigorous connection between the FSLE and LCSs has not been established, previous works [54, 55, 105–107] have shown that the ridges of the FSLE behave in a similar fashion as the ridges of the FTLE field. Following these works we assume that LCSs can be computed as ridges of FSLEs, and that they are transported by the flow as almost material surfaces/lines, with negligible flux of particles through them. Observations presented in this thesis are consistent with those assumptions.

The identification of LCS calculated from FTLE or FSLE fields in 2d flows is straightforward since they practically coincide with (finite-time) stable and unstable manifolds of relevant hyperbolic structures in the flow [50, 51, 105] (but see [103, 108]). The structure of these manifolds in 3d is generally much more complex than in 2d [63, 109], and they can be locally either lines or surfaces.

2.10.2 LCS in 3d as ridges of FSLE fields

Differently than 2d, where LCS can be visually identified as the maxima of the FSLE field, in 3d they are hidden within the volume data and one needs to explicitly compute and extract them, using the definition of LCSs as the ridges of the FSLE field. A ridge L is a co-dimension 1 orientable, differentiable manifold (which means that for a 3d domain D , ridges are surfaces) satisfying the following conditions [102]:

1. The field λ attains a local extremum at L .
2. The direction perpendicular to the ridge is the direction of fastest descent of λ at L .

CHAPTER 2. GENERAL NOTIONS

The method used to extract the ridges from the scalar field $\lambda(\mathbf{x}_0, t)$ is from [110]. It uses an earlier [111] definition of ridge in the context of image analysis, as a generalized local maxima of scalar fields. For a scalar field $f : \mathbb{R}^n \rightarrow \mathbb{R}$ with gradient $\mathbf{g} = \nabla f$ and Hessian \mathbf{H} , a d -dimensional height ridge is given by the conditions

$$\forall d < i \leq n, \quad \mathbf{g}^T \mathbf{e}_i = 0 \text{ and } \alpha_i < 0, \quad (2.52)$$

where $\alpha_i, i \in \{1, 2, \dots, n\}$, are the eigenvalues of \mathbf{H} , ordered such that $\alpha_1 \geq \dots \geq \alpha_n$, and \mathbf{e}_i is the eigenvector of \mathbf{H} associated with α_i . For $n = 3$, Eq. (2.52) becomes

$$\mathbf{g}^T \mathbf{e}_3 = 0 \text{ and } \alpha_3 < 0. \quad (2.53)$$

In other words, in \mathbb{R}^3 the $\mathbf{e}_1, \mathbf{e}_2$ eigenvectors point locally along the ridge and the \mathbf{e}_3 eigenvector is orthogonal to it, so the ridge maximizes the scalar field in the normal direction to it and in this direction the field is more convex than in any other direction, since the eigenvector associated with the most negative eigenvalue is oriented along the direction of maximum negative curvature of the scalar field.

The extraction process progresses by calculating the points where the ridge conditions are verified and the ridge strength $|\alpha_3|$ is higher than a predefined threshold s so that ridge points whose value of α_3 is lower (in absolute value) than s are discarded from the extraction process. Since the ridges are constructed by triangulations of the set of extracted ridge points, the strength threshold greatly determines the size and shape of the extracted ridge, by filtering out regions of the ridge that have low strength. The reader is referred to [110] for details about the ridge extraction method. The height ridge definition has been used to extract LCS from FTLE fields in several works (see, among others, [112]).

Since the λ value of a point on the ridge and the ridge strength α_3 are only related through the expressions (2.52) and (2.53), the relationship between the two quantities is not direct, which makes difficult to choose the appropriate strength threshold s . A too small value of s will result in the extraction of very small LCSs that appear to have little influence on the dynamics, while a large value will result in only a partial rendering of the larger and more significant LCS, limiting the possibility of observing their real impact on the flow.

The ridges extracted from the backward FSLE map approximate the attracting LCSs, and the ridges extracted from the forward FSLE map approximate the repelling LCSs. The attracting ones are the more interesting from a physical point of view [54, 55], since particles (or any passive scalar driven by the flow) typically

2.10. LAGRANGIAN COHERENT STRUCTURES (LCS)

approach them and spread along them, so that they are good candidates to be identified with the typical filamentary structures observed in tracer advection.

2.10.3 Calculation of 3d FSLE fields

In principle, to compute FSLE in 3d, the method of [54] can be extended to include the third dimension, by computing the time it takes for particles initially separated by $d_0 = [(\Delta x_0)^2 + (\Delta y_0)^2 + (\Delta z_0)^2]^{1/2}$ to reach a final distance of $d_f = [(\Delta x_f)^2 + (\Delta y_f)^2 + (\Delta z_f)^2]^{1/2}$.

Concerning turbulent flows where we can implement a fully 3d computation of the FSLE, we proceed as follows. A grid of initial locations $\mathbf{x}_0 = (x_i, y_j, z_k)$ is set up at time t , fixing the spatial resolution of the FSLE field (figure 2.8). Particles are released from each grid point and their three-dimensional trajectories are calculated. The distances of each neighbor particle with respect to the central one (initially d_0) is monitored until one of the separations reaches a value d_f .

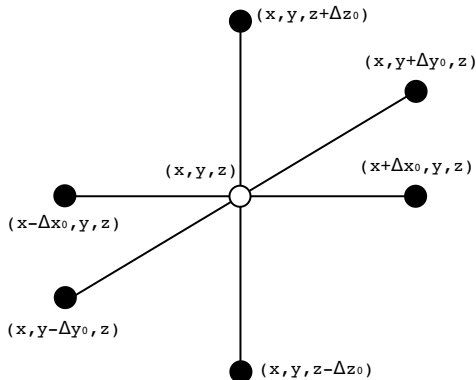


Figure 2.8: Computational setup for the calculation of the FSLE field in 3d. The FSLE at the location of the central particle (\circ) is a measure of the time it takes for any of the neighbor particles (\bullet) to diverge from the central particle by a distance greater than d_f .

In the ocean however, as indicated in [113], vertical displacements are much smaller than horizontal. Therefore, the displacement in the z direction does not contribute significantly to the calculation of d_f in the ocean, which prompts us to implement a quasi-3d computation of FSLEs: we use the full 3d velocity field for particle advection but particles are initialized in 2d horizontal ocean layers and the contribution Δz_f is not considered when computing d_f (see more details in

CHAPTER 2. GENERAL NOTIONS

[113]). In any case, since we allow the full 3d trajectories of particles, we take into account the vertical dynamics of the oceanic flows.

We obtain two different types of FSLE maps by integrating the three-dimensional particle trajectories backward and forward in time: the attracting LCSs (for the backward), and the repelling LCSs (forward) . We obtain in this way FSLE fields with a spatial resolution given by d_0 . When a particle leaves the velocity field domain or reaches a no-slip boundary, the FSLE value at its initial position and initial time is set to zero. If the interparticle separation remains smaller than d_f past a maximum integration time Δt , then the FSLE for that location is also set to zero.

2.11

Numerical modeling of turbulent flows

Turbulent flows have been a subject of intense research aiming at the development of simulation models. The main complication of the simulation is the range of scales of flow phenomena that need to be considered. Thus, the simulation of a turbulent flow requires the accurate representation of time and space scales that span several orders of magnitude and the higher the Reynolds number, the wider is this range. Given the constraints in computational resources, several classes of simulation methods have been devised in order to balance the need for accurate simulation of certain scales in the problem with the available resources. Thus, numerical models may be classed as [114]:

- (a) **Reynolds-averaged Navier Stokes (RANS) models:** In this class of models only the mean flow is explicitly calculated using the mean flow equations such as (2.11). Turbulent fluctuations are considered through the estimation of the Reynolds stress term by a variety of methods. In the most widespread of these, the Reynolds stress term is equated to a "diffusive term" proportional to the mean rate of strain and a "turbulent" viscosity.
- (b) **Large-eddy simulation (LES) models:** In this class of models, the larger scales of turbulent motions are explicitly modeled, while the smaller scales (the subgrid scales) are treated on an average sense just as in the RANS type of models.
- (c) **Direct numerical simulation (DNS) models:** This last class is comprised of models that treat explicitly the full spectrum of turbulent motions in a flow. In this models, the only approximation is in the discretization of

2.11. NUMERICAL MODELING OF TURBULENT FLOWS

space and time and they are the most accurate simulation models and also the most expensive.

The turbulent flow studied in chapter 3 was simulated with a DNS model using spectral discretization in a periodic domain. More details of the model can be found in section 3.2.

The oceanic velocity data used in this work (chapters 4, 5 and 6) was obtained from simulations of the regional ocean circulation model ROMS [115]. The ROMS model belongs to the group of models that solve the RANS equations in the LES fashion, using the hydrostatic and Boussinesq conditions. The first of these states that vertical changes in pressure are due only to changes in the weight of the water column and the second that density differences are small and negligible except when combined with gravity (e.g. in the calculation of weight). The ROMS model solves the primitive equations (RANS) in 3d curvilinear, terrain following grid with a free-surface [116] and additional equations for transported tracers. The Reynolds stress and turbulent fluxes at non resolved scales are parametrized in the RANS fashion with eddy viscosity and diffusivity. Further details on the ROMS model are given in the relevant chapters and a description of some numerical procedures for manipulating the outputs of ROMS data are described in the appendix A.

Three-dimensional Lagrangian structures in turbulence

Coherent structures in a turbulent channel flow

This chapter is based on

João H Bettencourt, Cristóbal López, and Emilio Hernández-García. Characterization of coherent structures in three-dimensional turbulent flows using the finite-size Lyapunov exponent. *Journal of Physics A: Mathematical and Theoretical*, 46(25):254022, 2013.

In this chapter we use the finite size Lyapunov Exponent (FSLE) to characterize Lagrangian coherent structures in a three-dimensional (3d) turbulent channel flow. Traditionally, fluid flows have been observed and studied in the Eulerian perspective where a fixed position is observed for a definite interval of time. The other perspective, the Lagrangian, follows the motion of the fluid and thus is better suited to study aspects of fluid flow such as material transport or the deformation of fluid material in a given state of motion. Lagrangian coherent structures act as the organizers of transport in fluid flows and are crucial to understand their stirring and mixing properties. Generalized maxima (ridges) of the FSLE fields are used to locate these coherent structures. Autocorrelations of the FSLE field show that the structure is substantially different from the near wall to the mid-channel region and relates well to the more widely studied Eulerian coherent structure of the turbulent channel flow. The ridges of the FSLE field have complex shapes due to the 3d character of the turbulent fluctuations.

CHAPTER 3. 3D COHERENT STRUCTURES IN CHANNEL FLOW

3.1

Introduction

Turbulent flow occurs in the natural environmental and in technological applications with such frequency that it could be considered the "natural" state of fluid flows to be found around us. Traditionally, fluid flows have been observed and studied in the Eulerian perspective where a fixed position is observed for a definite interval of time. The other perspective, the Lagrangian, follows the motion of the fluid and thus is better suited to study aspects of fluid flow such as material transport or the deformation of fluid material in a given state of motion.

Turbulent channel flow is a turbulent flow between two stationary, parallel walls separated by a distance 2δ . It has been studied extensively due to its geometrical simplicity and its wall-bounded nature, which makes it a suitable platform to study phenomena appearing in more complex turbulent wall-bounded flows of great technological interest.

The coordinates of the flow are: x for the streamwise direction, y for the cross-stream coordinate that separates the two plates, and z for the spanwise direction. The flow is maintained by a downstream pressure gradient $\frac{dP_0}{dx}$ acting against the wall shear stress. The laminar flow solution U_0 is a cross-stream parabolic profile given by

$$U_0(y) = \frac{y^2 - \delta^2}{2\mu} \frac{dP_0}{dx}, \quad (3.1)$$

where μ is the dynamic viscosity. Following the Reynolds averaging method [1], the turbulent flow velocity \mathbf{u} is decomposed in a mean $\mathbf{U} = (U(y), 0, 0)$ and a fluctuating component $\mathbf{u}' = (u', v', w')$. The mean turbulent velocity profile $U(y)$ differs from the laminar one, $U_0(y)$, by a lower centerline velocity $U(0)$ and increased near-wall velocity giving it a flatter shape. Due to the increase in mean velocity near the wall, the shear stress near the wall is higher for the turbulent case. The total shear stress τ appearing in the averaged Reynolds equations gets contributions from both the viscous stress and the Reynolds stress $-\overline{u'v'}$ associated to the velocity fluctuations:

$$\frac{\tau}{\rho} = \nu \frac{dU}{dy} - \overline{u'v'}. \quad (3.2)$$

The symmetries of the domain and the Reynolds equations imply that τ depends only on the cross-stream coordinate y , and the dependence is linear, so that it can be written as

$$\frac{\tau(y)}{\rho} = u_\tau^2 \left(1 - \frac{y}{\delta}\right). \quad (3.3)$$

3.2. DATA

The shear velocity u_τ gives the velocity scale of the turbulent velocity fluctuations. The formula [1]:

$$\rho u_\tau^2 = \mu \left. \frac{dU(y)}{dy} \right|_{y=0}, \quad (3.4)$$

allows to compute u_τ from measurements of the mean velocity profile from the simulations. A length scale can be formed by combining u_τ with ν : the wall scale $\delta^+ = \nu/u_\tau$. The wall distance can now be expressed as $y^+ = y/\delta^+$, and the same normalization could be done for the rest of coordinates. The viscous Reynolds number $Re_\tau = \delta/\delta^+$ is simply the ratio between the two relevant length scales.

The existence of coherent structures in turbulent wall-bounded flows has been known for several decades from investigations on intermittency in the interface between turbulent and potential flow regions, on the large eddy motions in the outer regions of the boundary layer, and on coherent features in the near-wall region ([83] and references therein). Since then, through experimental and numerical investigations, a picture of the organization of these coherent structures in the turbulent boundary layer has emerged, which has become rather complete from the Eulerian point of view [83, 117]. Our approach is a contribution to the Lagrangian exploration of these coherent structures, as in [62] and [118].

The longitudinal velocity field in the inner region of the channel (the viscous sub-layer adjacent to the wall and the intermediate buffer region) is organized into alternating streamwise streaks of high and low speed fluid. Turbulence production occurs mainly in the buffer region in association with intermittent and violent outward ejections of low-speed fluid and inrushes of high-speed fluid towards the wall. The outer region is characterized by the existence of three-dimensional δ -scale bulges that form on the turbulent/potential flows interface. Irrotational valleys appear at the edges of the bulges, entraining high-speed fluid into the turbulent inner region. A central element in the structure of the turbulent boundary layer is the hairpin vortex, mainly because it is a structure with the capability of transporting mass and momentum across the mean velocity gradient and because it provides a paradigm with which to explain several observations of wall turbulence [80, 83].

3.2

Data

The data used to extract the LCS come from a direct numerical simulation (DNS) of turbulent channel flow at a viscous Reynolds number $Re_\tau = 180$. The setup of the simulation follows that of [119] and is summarized in table 3.1. The

CHAPTER 3. 3D COHERENT STRUCTURES IN CHANNEL FLOW

Re chan. center	4000	Re_τ nominal	180	Re_τ actual	172
L_x	4π	δ	1	L_z	$\frac{4}{3}\pi$
L_x^+	2166.61	δ^+	0.0058	L_z^+	722.20
n_x	128	n_y	129	n_z	128
Δx^+	17.06	Δy^+	0.005	Δz^+	5.6867

Table 3.1: Simulation parameters. Quantities with $^+$ refer to wall units. L_x , 2δ and L_z are the domain sizes in the x , y and z directions. Δx^+ , Δy^+ and Δz^+ are the respective spatial resolutions (given at the first point above the wall for the y case), and n_x , n_y and n_z the corresponding number of grid points. $Re = U\delta/\nu$ is the Reynolds number based on the channel center mean speed, whereas $Re_\tau = u_\tau\delta/\nu$ is the viscous Reynolds number. The nominal value is an input to the computer code, and the actual value comes by using Eq. (3.4) for the computed mean profile $U(y)$.

simulations were conducted using the CFD solver `Channelflow.org` [120]. The `Channelflow.org` code solves the incompressible Navier-Stokes equations in a rectangular box with dimensions $L_x \times 2\delta \times L_z$, with periodic boundary conditions in the x (so that fluid leaving the computational domain in the direction of the mean flow at $x = L_x$ reenters it at $x = 0$) and in the spanwise z direction. No-slip conditions are imposed on $y = \pm\delta$. The unsteady velocity field \mathbf{u} is represented as a combination of Fourier modes in the x and z directions and of Chebyshev polynomials in the wall-normal direction. The pressure gradient necessary to balance the friction at the walls was chosen as to maintain a constant bulk velocity of $\frac{2}{3}U_0$. Time stepping is a 3rd-order Semi-implicit Backward Differentiation. Note that in our computations $\delta^+ = 1/Re_\tau = 0.0058$ so that in wall units $0 < y^+ < 344$.

The flow was integrated from an initial base-flow with parabolic profile and a small disturbance that evolved into a fully developed turbulent flow. The total integration time was $\Delta t = 600$ time units that in dimensionless form $t^+ = t(u_\tau^2/\nu)$ gives $\Delta t^+ = 83.54$. After an initial transient of about 200 time units the simulations reached a statistically stationary state from which statistics was accumulated.

The mean quantities and first order statistics of our simulations where compared to those of [119] and the agreement is quite good. The profile of the mean velocity in wall units is shown in figure 3.1. The profile for the Reynolds stress $-\overline{u'v'}$ shows that the maximum (in absolute value) is located at approximately $y^+ = 30$, in the outer limit of the buffer layer (see figure 3.2).

3.2. DATA

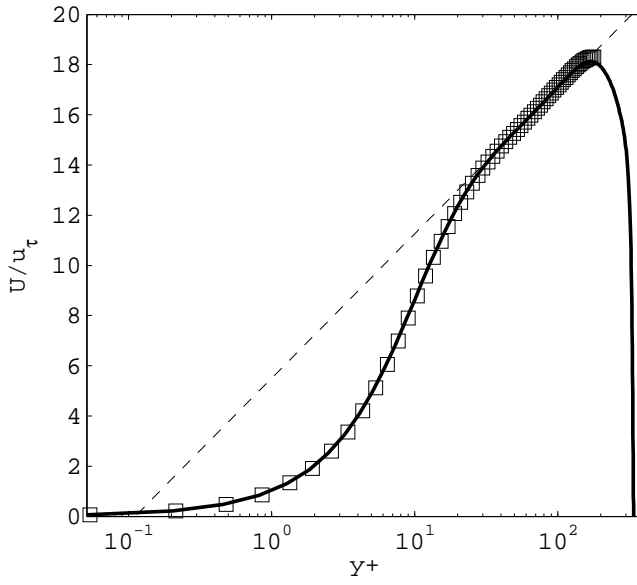


Figure 3.1: Mean velocity profile $U(y)/u_\tau$. Solid line: our simulations; squares: [119]; dashed line: logarithmic profile $U(y)/u_\tau = 2.5 \log(y^+) + 5.5$.

CHAPTER 3. 3D COHERENT STRUCTURES IN CHANNEL FLOW

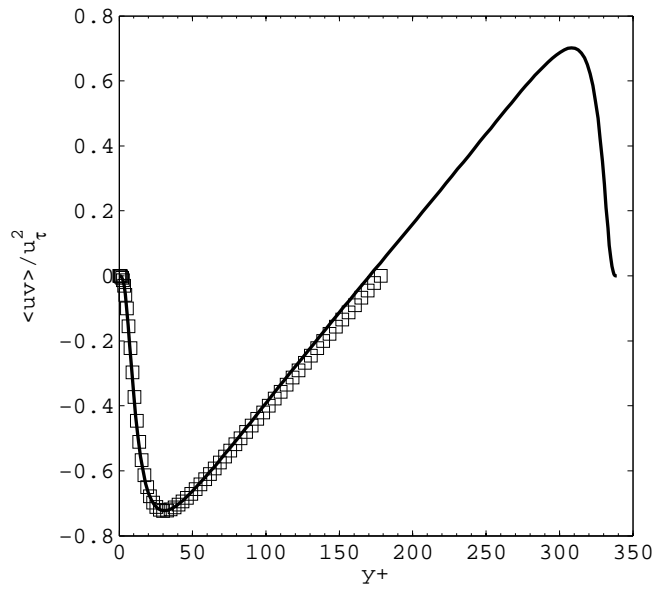


Figure 3.2: Reynolds stress $\overline{u'v'}$ profile at $Re_\tau = 180$. Solid line: our simulations; squares: [119] (given up to the channel centerline).

3.3. RESULTS

Calculation	d_0	d_f/d_0	Δt	dt
Complete channel	0.024	20	20	0.05
LCS subdomain	0.003	67	10	0.05

Table 3.2: FSLE calculation parameters. dt is the integration time step and Δt the maximum integration time.

3.3

Results

The LCS were extracted from the turbulent velocity field data described in the previous section. A calculation of FSLE field in the entire turbulent channel was conducted in order to understand the statistical properties of the FSLE field in this class of turbulent flows. A subsequent calculation in a subdomain of the channel was used to extract the LCS in that subdomain for a sequence of time instants. The setup of both calculations is shown in table 3.2.

The 3d FSLE field.

The 3d backward FSLE field for the entire channel was calculated at a single time instant in the statistically steady state. The initial and final distances d_0 and d_f were chosen as a balance between encompassing the widest possible range of scales of motion (measured by the ratio d_f/d_0), and adequate resolution and computational cost. The initial distance is of the order of $4\delta^+$ and the final distance of the order of 0.5δ – a typical scale of coherent structures found in the turbulent channel flow – so that the ratio of scales, d_f/d_0 , is approximately $Re_\tau/8$.

Figure 3.3 shows an instantaneous configuration of the FSLE values in a stream-wise wall-normal plane. The maxima of the FSLE appear to be located close to the walls with occasional sloping structures extending to the midchannel region. The channel center is devoid of high FSLE values but coherent patches of low FSLE values can still be observed. These structures are not distributed uniformly along the length of the channel but appear to be organized in packets. This organization bears resemblance to the widely accepted picture of organized structures in wall turbulence where the outer region is dominated by packets of sloping hairpin vortices and the inner region by near wall vortices (the hairpin vortices legs) and shear layers [80, 83].

CHAPTER 3. 3D COHERENT STRUCTURES IN CHANNEL FLOW

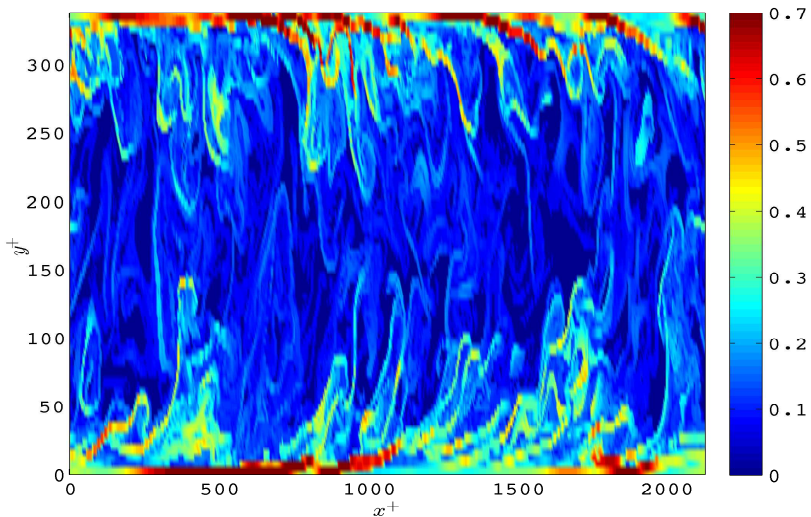


Figure 3.3: Instantaneous FSLE field at $t = 420$ shown on a streamwise/wall-normal plane in the turbulent channel. Walls are at the top and bottom of the figure. Mean velocity is in the streamwise direction from left to right.

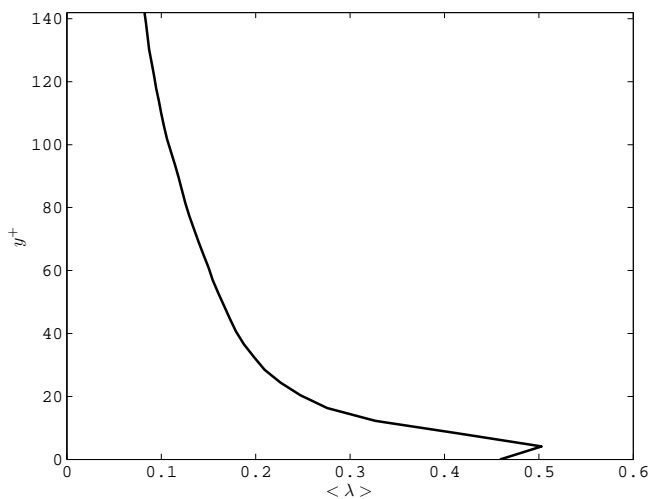


Figure 3.4: FSLE profile averaged over (x,z) , as a function of the cross-stream normalized coordinate y^+ . Only half of the channel is shown since the profile is quasi-symmetric about the channel centerline.

3.3. RESULTS

A cross-stream FSLE profile is obtained by averaging the 3d field over the periodic directions x and z . It is shown in figure 3.4. The profile is symmetric about the channel centerline and shows a maximum at approximately $y^+ = 4$, inside the viscous sublayer (this location corresponds to the first grid point off the wall).

Because of the periodic boundary conditions in the x and z directions the average profiles along these directions are rather unstructured, and we resort to two-point correlation functions to quantify the statistical structure properties. For each plane parallel to the walls, i.e. for each value of y^+ , we compute the fluctuations of the FSLE values around the average in that plane: $\Lambda(x^+, y^+, z^+) \equiv \lambda(x^+, y^+, z^+) - \langle \lambda(x^+, y^+, z^+) \rangle_{x^+, z^+}$. From this quantity we define the streamwise $R_{xx}(y^+; \bar{x}^+)$ correlation function as:

$$R_{xx}(y^+; \bar{x}^+) = \frac{\langle \Lambda(x^+, y^+, z^+) \Lambda(x^+ + \bar{x}^+, y^+, z^+) \rangle_{x^+, z^+}}{\langle \Lambda(x^+, y^+, z^+)^2 \rangle_{x^+, z^+}}, \quad (3.5)$$

and the spanwise $R_{zz}(y^+; \bar{z}^+)$ correlation function

$$R_{zz}(y^+; \bar{z}^+) = \frac{\langle \Lambda(x^+, y^+, z^+) \Lambda(x^+, y^+, z^+ + \bar{z}^+) \rangle_{x^+, z^+}}{\langle \Lambda(x^+, y^+, z^+)^2 \rangle_{x^+, z^+}}. \quad (3.6)$$

In the above equations the averages are over the periodic directions x^+ and z^+ . The correlations are shown in Figs. 3.5 and 3.6 at different distances from the walls: one smaller, one larger, and one approximately coincident with the location of the maximum Reynolds stress. These functions reveal sizes and organization of the different structures in the Lagrangian FSLE field, to be contrasted with Eulerian correlation functions in the same system [121].

Close to the wall ($y^+ = 4$ and $y^+ = 12.2$), viscous effects dominate. The correlations show that the FSLE field is organized in streamwise structures of length scale approximately $l^+ \sim 500$ wall units. In the transverse direction z^+ the oscillations seen in R_{zz} for $y^+ = 4$ indicate an approximately periodic arrangement of the streaks [62], with a spacing $\sim 50-100$ wall units. This pattern of organization is similar to what is seen in Eulerian descriptions [83, 121].

At planes further away from the wall ($y^+ = 28.4$ and $y^+ = 122.1$ in Figs. 3.5 and 3.6), correlation functions in both directions become shorter ranged, and periodic features are progressively lost. This corresponds to a rather disordered

CHAPTER 3. 3D COHERENT STRUCTURES IN CHANNEL FLOW

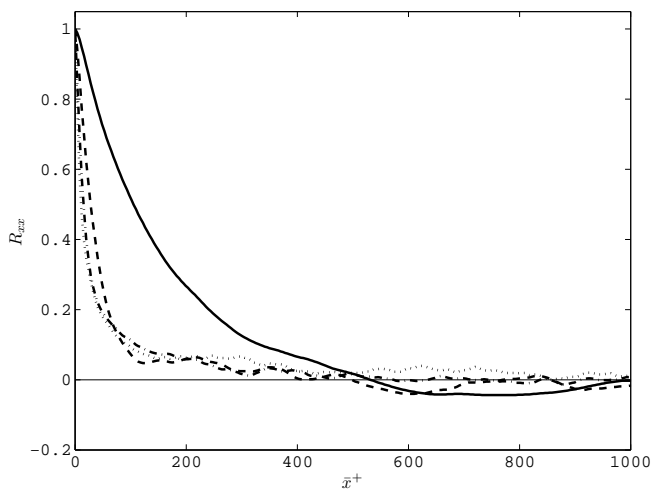


Figure 3.5: Streamwise correlation function $R_{xx}(y^+; \bar{x}^+)$ as a function of the streamwise separation \bar{x}^+ , at four distances from the lower wall: Continuous line: $y^+ = 4$; dashed line $y^+ = 12.2$; dash-dot line $y^+ = 28.4$; dotted line: $y^+ = 122.1$.

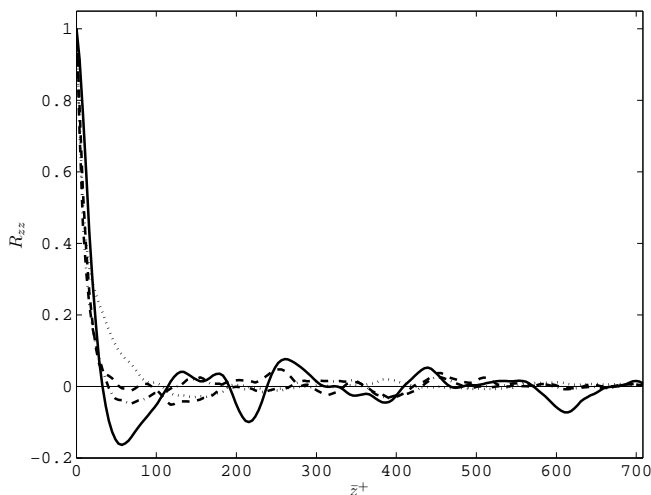


Figure 3.6: Spanwise correlation function $R_{zz}(y^+; \bar{z}^+)$ as a function of the spanwise separation \bar{z}^+ , at four distances from the lower wall: Continuous line: $y^+ = 4$; dashed line $y^+ = 12.2$; dash-dot line $y^+ = 28.4$; dotted line: $y^+ = 122.1$.

3.3. RESULTS

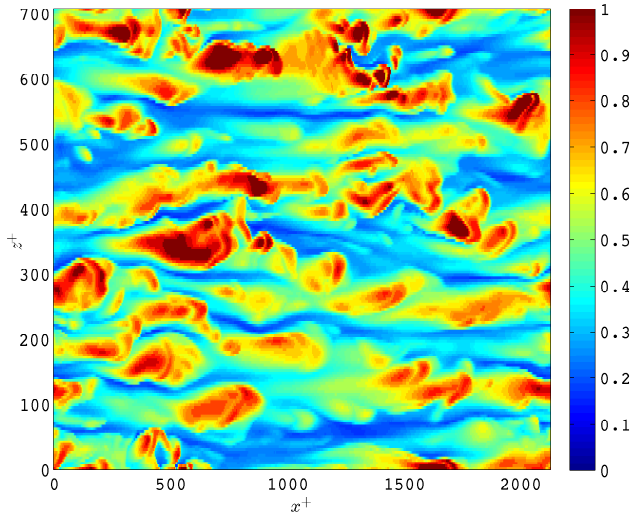


Figure 3.7: Instantaneous FSLE field in plane parallel to the wall at $y^+ = 4$. The time is the same as in figure 3.3

distribution of structures, each with a typical size related to the width of the correlation functions, i.e. of the order of 50 wall units, as also seen in figure 3.3.

An instantaneous near-wall FSLE field is shown in figure 3.7, where the high FSLE values appear in slender and elongated structures with length and width corresponding to the streamwise and spanwise correlation lengths discussed above. It is unclear whether the correlation lengths result from a single streamwise structure or from the overlapping of shorter structures (a feature of the near wall coherent structure arrangement [82]).

These are the highest FSLE values that are to be found in the channel as the plot in figure 3.4 shows. The mechanism for the formation of these structures could be the lifting of low speed fluid close to the wall by the action of counter rotating vortex pairs located above the viscous sublayer (see figure 3.8). This mechanism is widely known in the Eulerian view of coherent structures of turbulent wall bounded flows (*ejections* or *bursting*, [80]).

CHAPTER 3. 3D COHERENT STRUCTURES IN CHANNEL FLOW

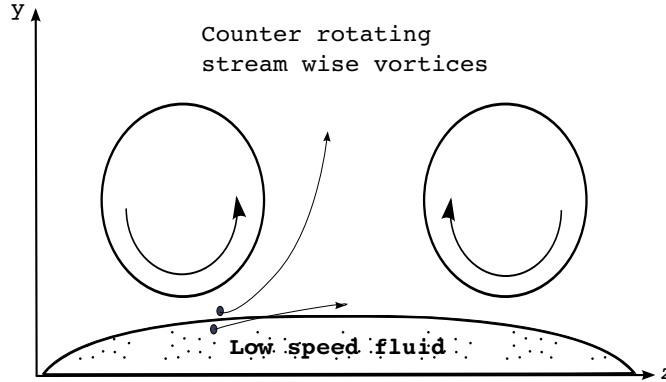


Figure 3.8: Mechanism for the rapid separation of fluid from the near wall viscous sublayer. The mean flow is into the page.

The near wall fluid is advected away from the wall by the action of these vortices. This mechanism could be responsible for very fast particle separation in particle pairs where one particle is lifted away and the other remains in the low speed zone close to the wall. We note that the particle separation would increase not only by the wall normal distance between particles but also because the ejected particle would move to a region with higher streamwise velocity. Shear layers near the wall is another possible way to produce large particle dispersion. These mechanisms would explain the fact that the maximum average FSLE is located so close to the wall and not on the buffer region where turbulence production is larger. To conclude, we note that these high FSLE regions near the wall seem to extend to the midchannel region in an inclined fashion. It is not clear whether this pattern signals the existence of a hairpin vortex with streamwise legs and inclined head or if there are two separate structures: the streamwise vortices *and* the hairpin arch or head [83]. Also, we note that the interpretation of the high FSLE regions near the wall do not require the existence of a counter rotation pair of vortices, as only one vortex would suffice.

To illustrate these mechanisms, a map of the FSLE field in a spanwise/wall normal plane for the LCS domain calculation is shown in figure 3.9, together with a set of passive particles initially located in a rectangular region close to the wall and released some instants before the time of the FSLE map. In order to focus just on the above mentioned ejection mechanism involving only the vertical motion of

3.3. RESULTS

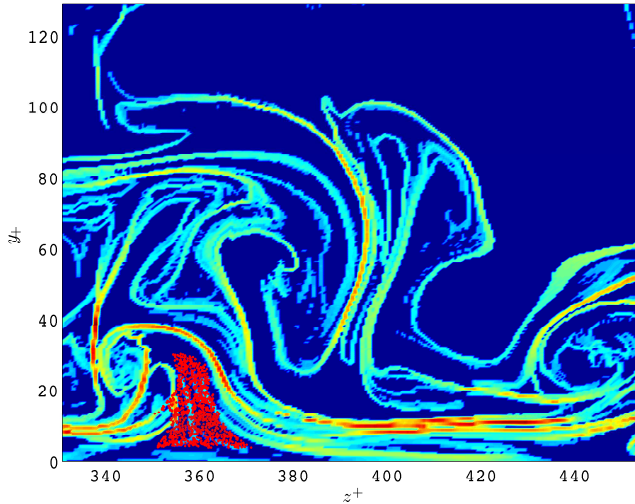


Figure 3.9: FSLE map in a (z, y) plane located at $x = 6.0$ ($x^+ = 1034$). The time of the map is $t = 413.8$, together with a set of particles initially located in rectangular region $z^+ \in [345, 380]$ and $y^+ \in [3.4, 13.8]$. The particles were released at $t = 409$. Particle trajectories were integrated using only the spanwise and wall normal velocity components. The mean flow is moving out of the page.

the particles, the trajectory integration was made in a 2d fashion by setting the longitudinal component of the particles velocity to zero.

The particles seem to have been lifted from wall by a streamwise vortex located to the left of the particle plume, with center at $(z^+, y^+) \sim (340, 30)$. We note that the structures are moving with the mean flow and that the continuous motion of the particles away from the wall is due to the passage of a streamwise structure that imparts this sustained motion to the particles for long enough time. To compare the Eulerian and Lagrangian coherent structures, figure 3.10 shows the turbulent velocity components in the same plane at the nearest time available in the turbulent dataset. The signature of the streamwise vortex discussed above can be seen in the Eulerian map at the same location. It is embedded in a patch of negative streamwise velocity fluctuation u . To the right, close to $z^+ = 380$, a vertical shear layer appears dividing the negative and positive patches of u . The Lagrangian signature of this vertical shear layer is not very strong and appears in figure 3.9 as quasi-vertical line of moderate FSLE extending from $y^+ = 25$

CHAPTER 3. 3D COHERENT STRUCTURES IN CHANNEL FLOW

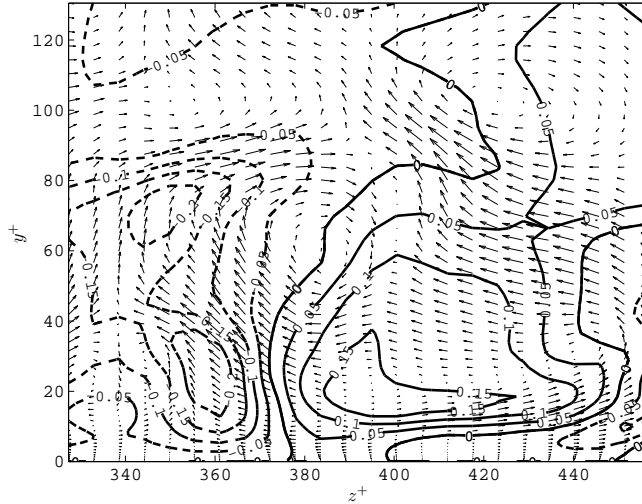


Figure 3.10: Instantaneous turbulent velocity components at $x = 6.0$ ($x^+ = 1034$) and $t = 413.75$. Velocity vectors correspond to the inplane velocity components (w, v) , together with contours of streamwise turbulent velocity u . Dashed contours are negative u (into the paper) and continuous contours are positive u (from the paper).

to $y^+ = 60$. On the lower right of the map, there is a set of high FSLE lines almost parallel to wall, signaling the existence of high particle dispersion. In the Eulerian map (figure 3.10), it can be seen that there is a shear layer parallel to the wall at the same location ($400 < z^+ < 440$ and $y^+ \sim 8$). The fact that this shear layer has a much stronger Lagrangian signature than the vertical shear layer could be because it has the same orientation and sign of the mean shear and therefore acts together with the latter to disperse neighboring particles across the wall normal direction. The high FSLE line seen at the middle of the map in figure 3.9, separating the two convoluted features can be seen to be related to the existence of two counter-rotating vortices, one with center located at $\sim (380, 60)$ and the other at $\sim (420, 100)$. The line of high FSLE line is seen to be located at the boundary between both vortices. In section 3.3, we present a 3d view of these structures and their evolution in time.

3.3. RESULTS

Propagation velocity.

In turbulent channel flow the velocity perturbations propagate in the streamwise direction approximately with the velocity of the mean flow [122]. In the case of Lyapunov exponents, [118] measured the FTLE field in an 2D turbulent boundary layer velocity field obtained by time-resolved PIV measurements. The FTLE maxima were found to move with the mean flow velocity.

We measured the propagation velocity of the FSLE field perturbation using a space-time correlation of the form:

$$R_{uu}(y^+; \bar{x}^+; \bar{t}^+) = \frac{\langle \Lambda(x^+, y^+, z^+, t^+) \Lambda(x^+ + \bar{x}^+, y^+, z^+, t^+ + \bar{t}^+) \rangle_{x^+, z^+}}{\langle \Lambda(x^+, y^+, z^+, t^+)^2 \rangle_{x^+, z^+}}, \quad (3.7)$$

where \bar{x}^+ and \bar{t}^+ are the delays in the streamwise direction and time. The time delay is fixed and the propagation velocity is defined as

$$V^+ = \frac{\bar{X}^+}{\bar{t}^+}, \quad (3.8)$$

where \bar{X}^+ is the streamwise lag for which R_{uu} is maximum. The choice of the time delay is related to the time scale of the FSLE field. A first rule is to choose a time delay that gives reasonable peaks in the correlation. If there are several time scales present, several \bar{t}^+ will result in correlations exhibiting peaks. The calculation of (3.8) was made for a full length and height spanwise section of the channel. A time series of FSLE fields with time step of $dt^+ = 1.8$ and time length $\Delta t^+ = 431$ was calculated for this section to offset the effects of the limited spanwise extent of the section. The final time lag used in (3.8) was equal to dt^+ . All larger delays produced correlations with no significant peak. A reason for this could be the fact that by setting the FSLE final distance the length scales of turbulence retained in the FSLE field is fixed, and then there will be only one time delay producing a peak in the correlation (3.7), specifically that corresponding to V^+ .

The profile of the propagation velocity is shown in figure 3.11. The propagation velocity is very close to the mean flow velocity. The result shows that the maxima of the FSLE field, that produce high values of R_{uu} and where we expect to find the ridges of the FSLE field, move with the flow. Hence, one may conclude, as expected, that the FSLE ridges also move with the flow approximately as material surfaces.

CHAPTER 3. 3D COHERENT STRUCTURES IN CHANNEL FLOW

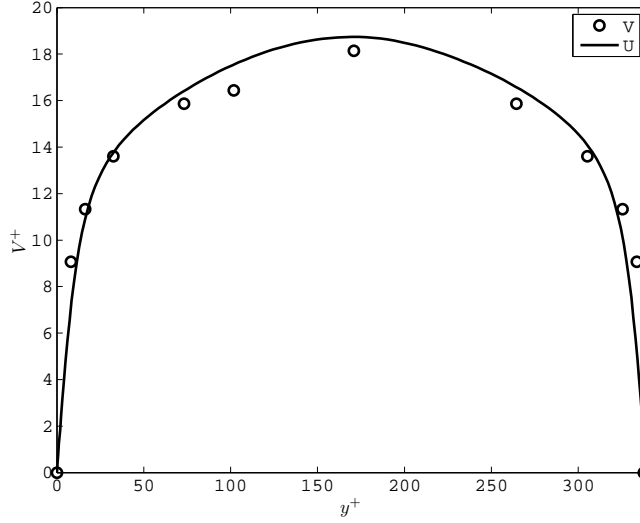


Figure 3.11: Propagation velocity of FSLE field (V^+) and mean flow (U^+).

The 3d LCS.

The previous description summarized the statistical properties of the different structures appearing in an instantaneous FSLE field. To make further progress we now extract three-dimensional attracting LCSs in a region of the channel at a series of time instants. The extraction domain had dimensions $L_x^+ \times L_y^+ \times L_z^+ = 103 \times 129 \times 124$. The initial separation d_0 and distance ratio d_f/d_0 were increased from the previous calculation to improve the resolution and extract smoother structures, but sacrificing a complete view of 3d LCS in the turbulent channel. The extraction threshold was set to $s = 50000$, a compromise value between speed and cost of extraction and continuity of the extracted surfaces. The FSLE fields were calculated for an interval of 1.5 time units with a time step of 0.1 units.

The 3d LCSs are rendered in figure 3.12, in a sequence of time instants, as they pass through the calculation domain. They have a clearly 3d shape and move with the flow. The LCS seem to create a boundary between the inner turbulent region and the outer region that is practically devoid of FSLE. The highest LCS have δ -scale heights above the wall, and have a distinct mushroom shape enclosing the regions of the channel closer to the wall, where high FSLE values can be found.

3.3. RESULTS

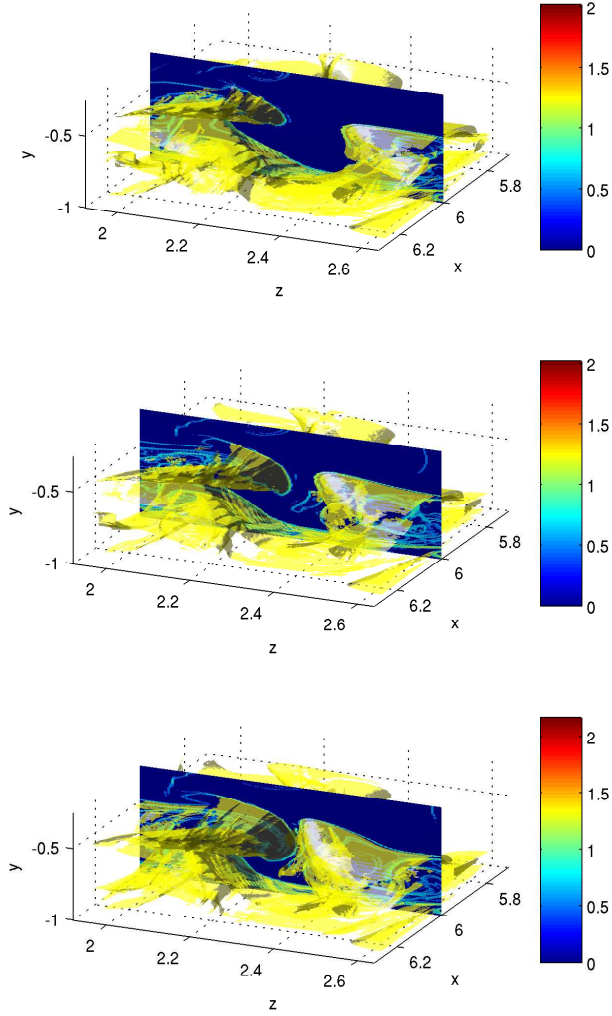


Figure 3.12: 3d attracting LCS in the channel flow together with a FSLE map at the fixed plane $x = 6.0$ ($x^+ = 1034$). Time goes from top to bottom, at intervals of 0.1 time units. The flow direction is in the positive x direction in each panel, and a wall is at the bottom. The sequence shows how one of the flow structures is advected and passes through the $x = 6.0$ plane.

CHAPTER 3. 3D COHERENT STRUCTURES IN CHANNEL FLOW

Near the wall, the LCS adopt the shape of sheets parallel to it, which reflects the high rates of shear that occur in that region. These sheets form the base of the mushroom-shaped excursions up to the channel center.

3.4

Conclusions

Lyapunov exponents are useful to identify Lagrangian coherent structures in turbulent flows. These constitute the pattern determining the pathways of particle transport in the flow and thus strongly influence the transport and mixing properties in the fluid. In a turbulent channel flow, the FSLE field is organized into longitudinal structures close to the wall that develop into sloping ones away from the wall. Correlations in the streamwise and spanwise direction show the typical dimensions of these structures. They were found to be similar to the Eulerian coherent structures that are known to exist in this same regions of the turbulent channel. Specially, elongated streamwise vortices that move low speed fluid away from the wall into the channel core. In 3d, the LCSs appear as mushroom-shaped excursions of near-wall sheet-like structures of a scale comparable to the channel width. They separate the channel into an interior region, where the FSLE attains high values, and an exterior region, showing low FSLE values. The distribution of LCS in the turbulent channel resembles the commonly accepted picture where upward excursions of near wall fluid coexist with inward rushes of mid-channel irrotational flow. Further work is necessary to elucidate the relations between LCS and fluid transport in these type of flows, not least because the visualization of 3d structures and transport in turbulence is a complex and time-consuming subject. We note that there are fundamental differences between the Lagrangian and Eulerian coherent structures, although they can actually have a common interpretation as vortices or shear layers. Lagrangian coherent structures have a clear impact in particle trajectories whereas Eulerian coherent structures are related to space/time coherency in, e.g., velocity signals and do not necessarily affect particles. In the above comparison, only the strongest FSLE features had a clear connection to the features in the Eulerian distribution, which indicates that, inversely, only the Eulerian features that live long enough or are strong enough to affect particles in a discernible fashion will appear in the Lagrangian point of view of coherent structures. The results shown in this chapter highlight the usefulness of Lyapunov analysis and dynamical systems theory as a tool to study transport and mixing in fluid flows, through the concept of Lagrangian coherent structures.

Acknowledgements

The ridge extraction algorithm of [110] is available in the `seek` module of the data visualization library `Teem` (<http://teem.sf.net>).

Applications to oceanic processes

Oceanic 3d Lagrangian Coherent Structures

This chapter is based on

João H. Bettencourt, Cristóbal López, and Emilio Hernández-García. Oceanic three-dimensional Lagrangian coherent structures: A study of a mesoscale eddy in the Benguela upwelling region. *Ocean Modelling*, 51(0):73 – 83, 2012.

We study three dimensional oceanic Lagrangian Coherent Structures (LCSs) in the Benguela region, as obtained from an output of the ROMS model. We first compute Finite-Size Lyapunov exponent (FSLE) fields in the region volume, characterizing mesoscale stirring and mixing. Average FSLE values show a general decreasing trend with depth, but there is a local maximum at about 100 m depth. LCSs are extracted as ridges of the calculated FSLE fields. They present a “curtain-like” geometry in which the strongest attracting and repelling structures appear as quasi vertical surfaces. LCSs around a particular cyclonic eddy, pinched off from the upwelling front are also calculated. The LCSs are confirmed to provide pathways and barriers to transport in and out of the eddy.

4.1

Introduction

The main objective of this chapter is the characterization of 3d LCSs, extracted in an upwelling region, the Benguela area in the Southern Atlantic Ocean. To confirm that our identification of LCSs with ridges of the FSLE field, we perform

CHAPTER 4. OCEANIC 3D STRUCTURES

(in section 4.3.2) direct particle trajectory integrations that show that the computed LCS really organize the tracer flow. In our work, we will emphasize the numerical methodology since up to now FSLEs have only been computed for the marine surface (an exception is [123]). We then focus on a particular eddy very prominent in the area at the chosen temporal window and study the stirring and mixing on its vicinity. Some previous results for Lagrangian eddies were obtained by [124] and [65], applying the methodology of lobe dynamics and the turnstile mechanism to eddies pinched off from the Loop Current. In this chapter we focus on FSLE fields and the associated particle trajectories to study transport in and out of the chosen mesoscale eddy.

To circumvent the lack of appropriate observational data in the vertical direction, we use velocity fields from a numerical simulation. They are high resolution simulations from the ROMS model (see section 4.2 below) thus appropriate to study regional-medium scale basins.

4.2

Data and Methods.

4.2.1 Velocity data set.

The Benguela ocean region is situated off the west coast of southern Africa. It is characterized by a vigorous coastal upwelling regime forced by equatorward winds, a substantial mesoscale activity of the upwelling front in the form of eddies and filaments, and also by the northward drift of Agulhas eddies.

The velocity data set comes from a regional ocean model simulation of the Benguela Region [126]. ROMS [115, 127] is a split-explicit free-surface, topography following model. It solves the incompressible primitive equations using the Boussinesq and hydrostatic approximations. Potential temperature and salinity transport are included by coupling advection/diffusion schemes for these variables. The model was forced with climatological data. The data set area extends from 12°S to 35°S and from 4°E to 19°E (see Fig. 1). The velocity field $\mathbf{u} = (u, v, w)$ consists of two years of daily averaged zonal (u), meridional (v), and vertical velocity (w) components, stored in a three-dimensional grid with an horizontal resolution of 1/12 degrees ~ 8 km, and 32 vertical terrain-following levels using a stretched vertical coordinate where the layer thickness varies, increasing from the surface to the ocean interior. Since the ROMS model considers the hydrostatic approximation it is important to note that [128], when comparing results from non-hydrostatic and hydrostatic versions of the same model of

4.2. DATA AND METHODS.

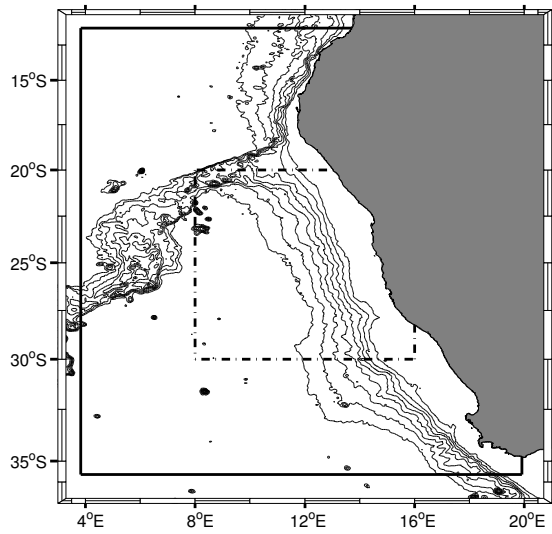


Figure 4.1: Benguela ocean region. The velocity field domain is limited by the continuous black line. The FSLE calculation area is limited by the dash-dot black line. Bathymetric contour lines are from ETOPO1 global relief model [125] starting a 0 m depth up to 4000 m at 500 m interval.

CHAPTER 4. OCEANIC 3D STRUCTURES

vertical motions at submesoscale fronts, found that while instantaneous vertical velocities structures differ, the averaged vertical flux is similar in both hydrostatic and non-hydrostatic simulations.

4.2.2 3d FSLE fields.

The main difficulty in extending the calculation of 3d FSLE fields is that in the ocean vertical displacements (even in upwelling regions) are much smaller than the horizontal ones, and so do not contribute significantly to total particle dispersion [123]. By the time the horizontal particle dispersion has scales of tenths or hundreds of kilometers (typical mesoscale structures are studied using $\delta_f \approx 100km$ [54]), particle dispersion in the vertical can have at most scales of hundreds of meters and usually less. This means that the vertical separation will not contribute significantly to the accumulated distance between particles. In addition, since length scales in the horizontal and vertical differ by several orders of magnitude, one faces the impossibility of assigning equal δ_0 to the horizontal and vertical particle pairs. It should be noted however that these shortcomings arise from the different scales of length and time that characterize horizontal and vertical dispersion processes in the ocean, and so should not be seen as intrinsic limitations of the method. For non-oceanic flows a direct generalization of FSLEs is straightforward.

Thus, in this chapter we implemented a quasi three-dimensional computation of FSLEs. That is, we make the computation for every (2d) ocean layer, but where the particle trajectories calculation use the full 3d velocity field. I.e., at each level (depth) we set $\delta z_O = 0$, and the final distance is computed without taking the vertical distance between particles. It is important to note that, since we allow the particles to evolve in the full 3d velocity field, we take into account vertical quantities such as vertical velocity shear that may influence the horizontal separation between particle pairs.

There are other possible approaches to the issue of different scales in the vertical and horizontal. One way is to assign anisotropic initial and final displacements in the FSLE calculation (i. e., including a δz_0 and δz_f much smaller than the horizontal initial and final separations). A second approach is to use different weights for the horizontal and vertical separations in the calculations of the distance, perhaps in combination with the first. We have checked both alternatives and found that, with reasonable choices of initial and final distances and distance metrics, the results were equivalent to the quasi-3d computation. The reason is that actual dispersion is primarily horizontal as commented above.

4.2. DATA AND METHODS.

More in detail, a grid of initial locations \mathbf{x}_0 in the longitude/latitude/depth geographical space (ϕ, θ, z) , fixing the spatial resolution of the FSLE field, is set up at time t . The horizontal distance among the grid points, δ_0 , was set to 1/36 degrees (≈ 3 km), i.e. three times finer resolution than the velocity field [99], and the vertical resolution (distance between layers) was set to 20 m in order to have a good representation of the vertical variations in the FSLE field. Particles are released from each grid point and their three dimensional trajectories calculated. The distances of each particle with respect to the ones that were initially neighbors at an horizontal distance δ_0 are monitored until one of the horizontal separations reaches a value δ_f . By integrating the three dimensional particle trajectories backward and forward in time, we obtain the two different types of FSLE maps: the attracting LCS (for the backward), and the repelling LCS (forward) [54, 105]. We obtain in this way FSLE fields with a horizontal spatial resolution given by δ_0 . The final distance δ_f was set to 100 km, which is, as already mentioned, a typical length scale for mesoscale studies. The trajectories were integrated for a maximum of $T = 178$ days (approximately six months) using an integration time step of 6 hours. When a particle reached the coast or left the velocity field domain, the FSLE value at its initial position and initial time was set to zero. If the inter particle horizontal separation remains smaller than δ_f during all the integration time, then the FSLE for that location is also set to zero.

The equations of motion that describe the evolution of particle trajectories are

$$\frac{d\phi}{dt} = \frac{1}{R_z} \frac{u(\phi, \theta, z, t)}{\cos(\theta)}, \quad (4.1)$$

$$\frac{d\theta}{dt} = \frac{1}{R_z} v(\phi, \theta, z, t), \quad (4.2)$$

$$\frac{dz}{dt} = w(\phi, \theta, z, t), \quad (4.3)$$

where ϕ is longitude, θ is latitude and z is the depth. R_z is the radial coordinate of the moving particle $R_z = R - z$, with $R = 6371$ km the mean Earth radius. For all practical purposes, $R_z \approx R$. Particle trajectories are integrated using a 4th order Runge-Kutta method. For the calculations, one needs the (3d) velocity values at the current location of the particle. Since the six grid nodes surrounding the particle do not form a regular cube, direct trilinear interpolation can not be used. Thus, an isoparametric element formulation is used to map the nodes of the velocity grid surrounding the particles position to a regular cube, and an inverse isoparametric mapping scheme [129] is used to find the coordinates of the interpolation point in the regular cube coordinate system.

CHAPTER 4. OCEANIC 3D STRUCTURES

The structure of LCS in 3d is can be very complex in turbulent flows (as seen in the previous chapter), and they can be locally either lines or surfaces. As commented before, however, vertical motions in the ocean are slow. Thus, at each fluid parcel the strongest attracting and repelling directions should be nearly horizontal. This, combined with the incompressibility property, implies that the most attracting and repelling regions (i.e. the LCSs) should appear as almost vertical surfaces, since the attraction or repulsion should occur normally to the LCS. As a consequence, the LCSs will have a “curtain-like” geometry, with deviations from the vertical due to either the orientation of the most attracting or repelling direction deviating from the horizontal, or when strong vertical shear produces variations along the vertical in the most repelling or attracting regions in the flow. We expect the LCS sheet-like objects to coincide with the strongest hyperbolic manifolds when these are two dimensional, and to contain the strongest hyperbolic lines.

The curtain-like geometry of the LCS was already commented in [64], [124], or [65]. In the latter paper it was shown that, in a 3d flow, these structures would appear mostly vertical when the ratio of vertical shear of the horizontal velocity components to the average horizontal velocities is small. This ratio also determines the vertical extension of the structures. In [124], the argument was used to construct a 3d picture of hyperbolic structures from the computation in a 2d slice. In the present chapter we confirm the curtain-like geometry of the LCSs, and show that they are relevant to organize the fluid flow in this realistic 3d oceanic setting. This is done in the next section by comparing actual particle trajectories with the computed LCSs.

4.3

Results

4.3.1 Backward and forward 3d FSLE fields

The 3d FSLE fields were calculated for a 30 day period starting September 17, with snapshots taken every 2 days. The fields were calculated for an area of the Benguela ocean region between latitudes 20°S and 30°S and longitudes 8°E to 16°E (see figure 4.1). The area is bounded at NW by the Walvis Ridge and the continental slope approximately bisects the region from NW to SE. The western half of the domain has abyssal depths of about 4000 m. The calculation domain extended vertically from 20 up to 580 m of depth. Both backward and forward calculations were made in order to extract the attracting and repelling LCS.

4.3. RESULTS

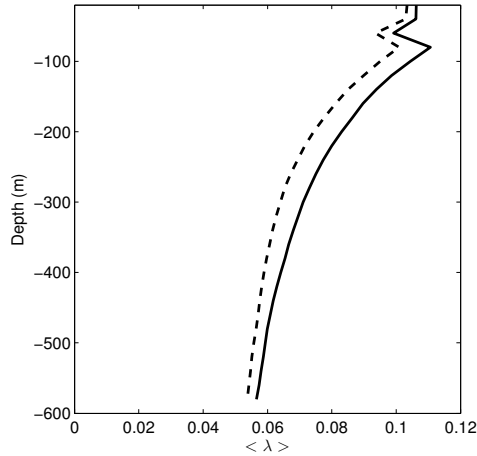


Figure 4.2: Vertical profile of 30 day average backward and forward FSLE. The 30 day average field was spatially averaged at each layer over the FSLE calculation area to produce the vertical profiles. The backward FSLE average is shown in continuous and the forward FSLE is shown in dashed.

Figure 4.2 displays the vertical profile of the average FSLE for the 30 day period. There are small differences between the backward and the forward values due to the different intervals of time involved in their calculation. But both profiles have a similar shape and show a general decrease with depth. There is a notable peak in the profiles at about 100 m depth that indicates increased mesoscale variability (and transport, as shown in Sect. 4.3.2 at that depth).

A snapshot of the attracting LCSs for day 1 of the calculation period is shown in figure 4.3. As expected, the structures appear as thin vertical curtains, most of them extending throughout the depth of the calculation domain. The area is populated with LCS, denoting the intense mesoscale activity in the Benguela region. As already mentioned, in three dimensions the ridges are not easily seen, since they are hidden in the volume data. However the horizontal slices of the field in figure 4.3 show that the attracting LCS fall on the maximum backward FSLE field lines of the 2d slices. The repelling LCS (not shown) also fall on the maximum forward FSLE field lines of the 2d slices.

Since the λ value of a point on the ridge and the ridges strength α_3 are only related through the expressions (2.52) and (2.53), the relationship between the two quantities is not direct. This creates a difficulty in choosing the appropriate strength threshold for the extraction process. A too small value of s will result

CHAPTER 4. OCEANIC 3D STRUCTURES

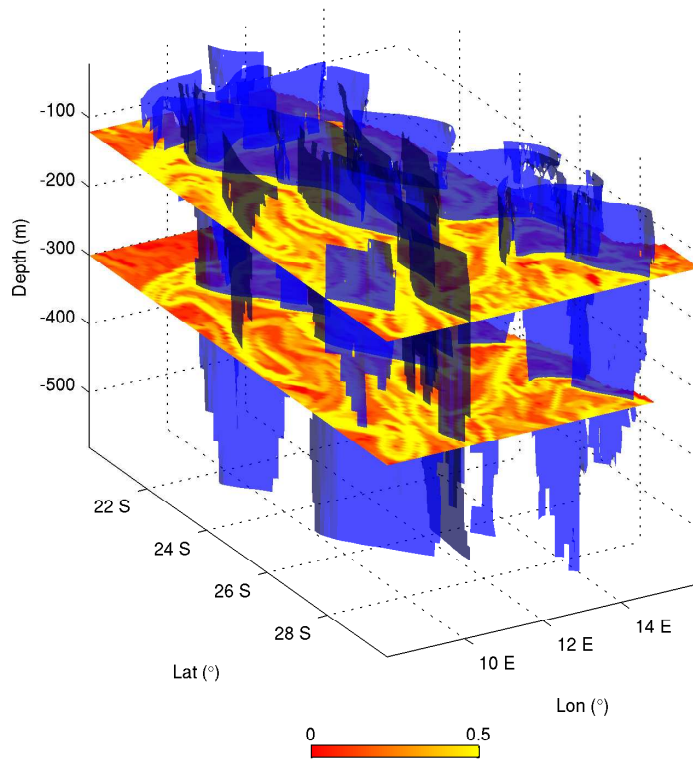


Figure 4.3: Attracting LCS (blue) for day 1 of the calculation period, together with horizontal slices of the backward FSLE field at 120 m and 300 m depth. Colorbar refers to colormap of horizontal slices. The units of the colorbar are day^{-1} .

4.3. RESULTS

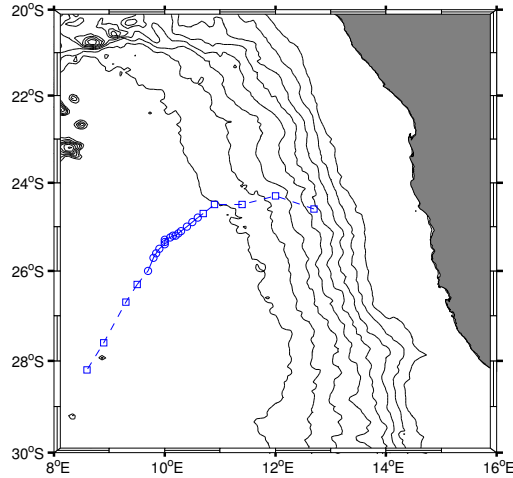


Figure 4.4: Trajectory (advancing from NE to SW) of the eddy center inside the calculation domain. Circles indicate the center location during the 30 day FSLE calculation period, and squares previous and posterior positions. Bathymetric lines same as in figure 4.1.

in very small LCS that appear to have little influence on the dynamics, while a greater value will result in only a partial rendering of the LCS, limiting the possibility of observing their real impact on the flow. Computations with several values of s lead us to the optimum choice $s = 20 \text{ day}^{-1} \text{ m}^{-2}$, meaning that grid nodes with $\alpha_3 < -20 \text{ day}^{-1} \text{ m}^{-2}$ were filtered out from the LCS triangulation.

We have seen in this section an example of how the ridges of the $3d$ FSLE field, the LCS, distribute in the Benguela ocean region. Their ubiquity shows their impact on the transport and mixing properties. In the next section we concentrate on the properties of a single $3d$ mesoscale eddy.

4.3.2 Study of the dynamics of a relevant mesoscale eddy

Let us study a prominent cyclonic eddy observed in the data set. The trajectory of the center of the eddy was tracked and it is shown in figure 4.4. The eddy was apparently pinched off at the upwelling front. At day 1 of the FSLE calculation period its center was located at latitude 24.8°S and longitude 10.6°E , leaving the continental slope, and having a diameter of approximately 100 km. One may ask: what is its vertical size? is it really a barrier, at any depth, for particle transport?

CHAPTER 4. OCEANIC 3D STRUCTURES

To properly answer these questions the eddy, in particular its frontiers, should be located. From the Eulerian point of view it is commonly accepted that eddies are delimited by closed contours of vorticity and that the existence of strong vorticity gradients prevent the transport in and out of the eddy. Such transport may occur when the eddy is destroyed or undergoes strong interactions with other eddies [78]. In a Lagrangian view point, however, an eddy can be defined as a region delimited by intersections and tangencies of LCS, whether in 2d or 3d space. The eddy itself is an elliptic structure [51, 65, 124]. In this Lagrangian view of an eddy, the transport inhibition to and from the eddy is now related to the existence of these transport barriers delimiting the eddy region, which are known to be quasi impermeable.

Using the first approach, i.e., the Eulerian view, the vertical distribution of the Q -criteria [81, 130] was used to determine the vertical extension of the mesoscale eddy. The Q criterion is a 3d version of the Okubo-Weiss criterion [131, 132] and measures the relative strength of vorticity and straining. In this context, eddies are defined as regions with positive Q , with Q the second invariant of the velocity gradient tensor

$$Q = \frac{1}{2}(\|\boldsymbol{\Omega}\|^2 - \|\mathbf{S}\|^2), \quad (4.4)$$

where $\|\boldsymbol{\Omega}\|^2 = \text{tr}(\boldsymbol{\Omega}\boldsymbol{\Omega}^T)$, $\|\mathbf{S}\|^2 = \text{tr}(\mathbf{S}\mathbf{S}^T)$ and $\boldsymbol{\Omega}$, \mathbf{S} are the antisymmetric and symmetric components of $\nabla\mathbf{u}$. Using $Q = 0$ as the Eulerian eddy boundary, it can be seen from Fig. 4.5 that the eddy extends vertically down to, at least, 600 m.

Let us move to the Lagrangian description of eddies, which is much in the spirit of our study, and will allow us to study particle transport: eddies can be defined as the *region bounded by intersecting or tangent repelling and attracting LCS* [65, 124]. Using this criterion, and first looking at the surface located at 200 m depth, we see in Fig. 4.6 that certainly the Eulerian eddy seems to be located inside the area defined by several intersections and tangencies of the LCS. This eddy has an approximate diameter of 100 km. In the south-north direction there are two intersections that appear to be hyperbolic points (H1 and H2 in figure 4.6). In the West-East direction, the eddy is closed by a tangency at the western boundary, and a intersection of lines at the eastern boundary. The eddy core is devoid of high FSLE lines, indicating that weak stirring occurs inside [54]. As additional Eulerian properties, we note that near or at the intersections H1 and H2 the Q -criterion indicates straining motions. In the case of H2, figure 4.5 (right panel) indicates high shear up to 200 m depth. The fact that the hyperbolic regions H1 and H2 lie in strain dominated regions of the flow ($Q < 0$) highlights the connection between hyperbolic particle behavior and instantaneous hyperbolic regions of the flow. The ridges of the FSLE field, however, do not

4.3. RESULTS

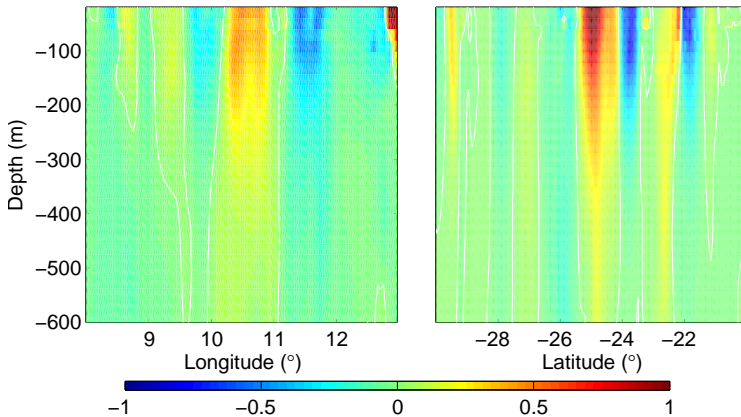


Figure 4.5: Colormap of Q -criterion. White contours have $Q = 0$. Day 1 of the 30 day FSLE calculation period. Left panel: Latitude 24.5°S ; Right panel: Longitude 10.5°E . Colorbar values are $Q \times 10^{10} \text{ s}^{-2}$.

remain in the negative Q regions but cross into rotation dominated regions with $Q > 0$. This indicates that there are some differences between the Eulerian view (Q) and the Lagrangian view (FSLE). It is the latter that can be understood in terms of particle behaviour as limiting regions of initial conditions (particles) that stay away from hyperbolic regions for long enough time [51].

In 3d, the eddy is also surrounded by a set of attracting and repelling LCS (figure 4.7), calculated as explained in section 2.10.2. The lines identified in figure 4.6 are now seen to belong to the vertical of these surfaces.

Note that the vertical extent of these surfaces is in part determined by the strength parameter used in the LCS extraction process, so their true vertical extension is not clear from the results presented here. On the south, the closure of the Lagrangian eddy boundary extends down to the maximum depth of the calculation domain, but moving northward it is seen that the LCS shorten their depth. Probably this does not mean that the eddy is shallower in the North, but rather that the LCS are losing strength (lower $|\alpha_3|$) and portions of it are filtered out by the extraction process. In any case, it is seen that as in two-dimensional calculations, the LCS delimiting the eddy do not perfectly coincide with its Eulerian boundary [105], and we expect the Lagrangian view to be more relevant to address transport questions.

In the next paragraphs we analyze the fluid transport across the eddy boundary. Some previous results for Lagrangian eddies were obtained by [124] and [65]. Ap-

CHAPTER 4. OCEANIC 3D STRUCTURES

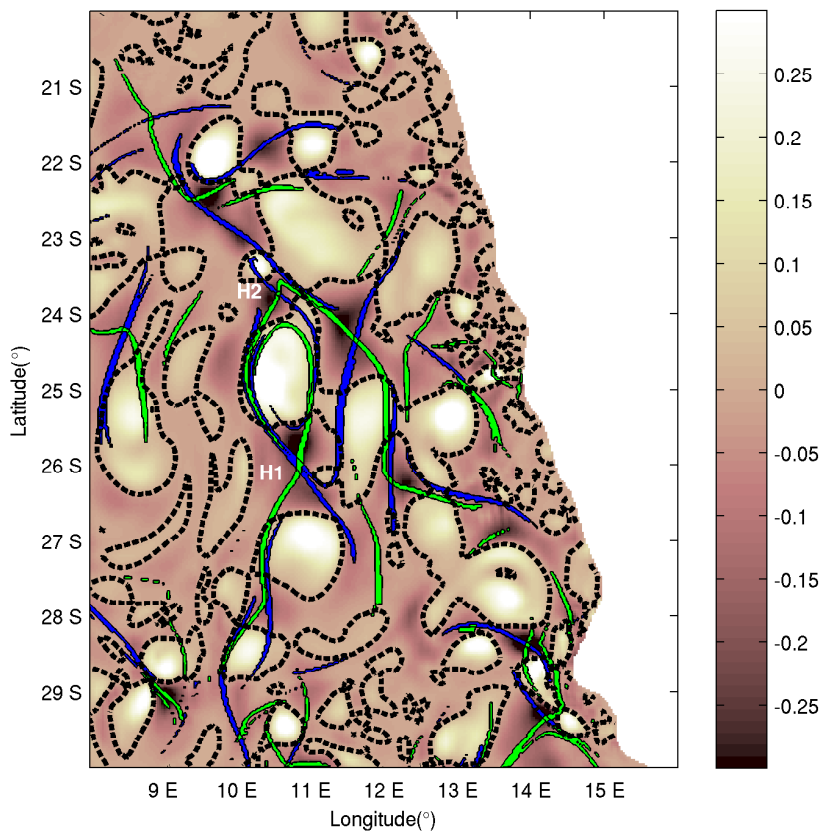


Figure 4.6: Q -criterion map at 200 m depth together with patches of backward (blue) and forward (green) FSLE values. Black dashed lines have $Q = 0$. FSLE patches contain the highest 60% of FSLE values. Colorbar values are $Q \times 10^{10} \text{ s}^{-2}$. The eddy we study is the clear region in between points H1 and H2.

4.3. RESULTS

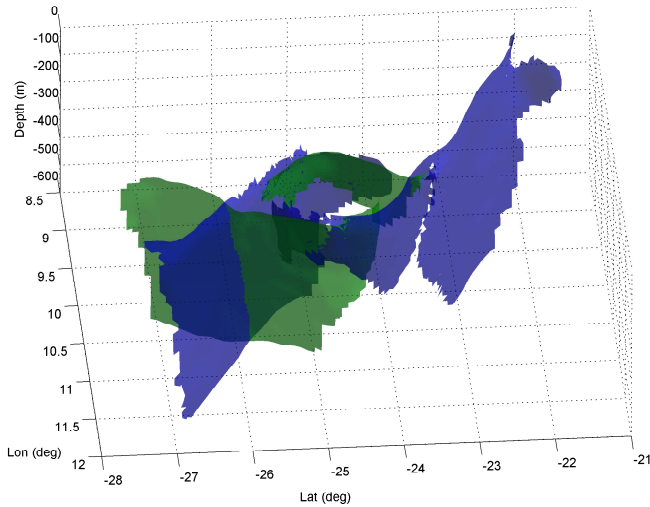


Figure 4.7: 3d LCSs around the mesoscale eddy at day 1 of the 30 day FSLE calculation period. Green: repelling LCS; Blue: attracting LCS.

plying the methodology of lobe dynamics and the turnstile mechanism to eddies pinched off from the Loop Current, [124] observed a net fluid entrainment near the base of the eddy, and net detrainment near the surface, being fluid transport in and out of the eddy essentially confined to the boundary region. Let us see what happens in our setting.

We consider six sets of 1000 particles each, that were released at day 1 of the FSLE calculation period, and their trajectories integrated by a fourth-order Runge-Kutta method with a integration time step of 6 hours. The sets of particles were released at depths of 50, 100, 200, 300, 400 and 500 m. In figure 4.8 we plot the particle sets together with the Lagrangian boundaries of the mesoscale eddy viewed in 3d. A top view is shown in figure 4.9. As expected, vertical displacements are small.

At day 3 (top left panel of figures 4.8 and 4.9) it can be seen that there is a differential rotation (generally cyclonic, i.e. clockwise) between the sets of particles at different depths. The shallower sets rotate faster than the deeper ones. This differential rotation of the fluid particles could be viewed, in a Lagrangian perspective, as the fact that the attracting and repelling strength of the LCS that limit the eddy varies with depth. Note that the six sets of particles are released

CHAPTER 4. OCEANIC 3D STRUCTURES

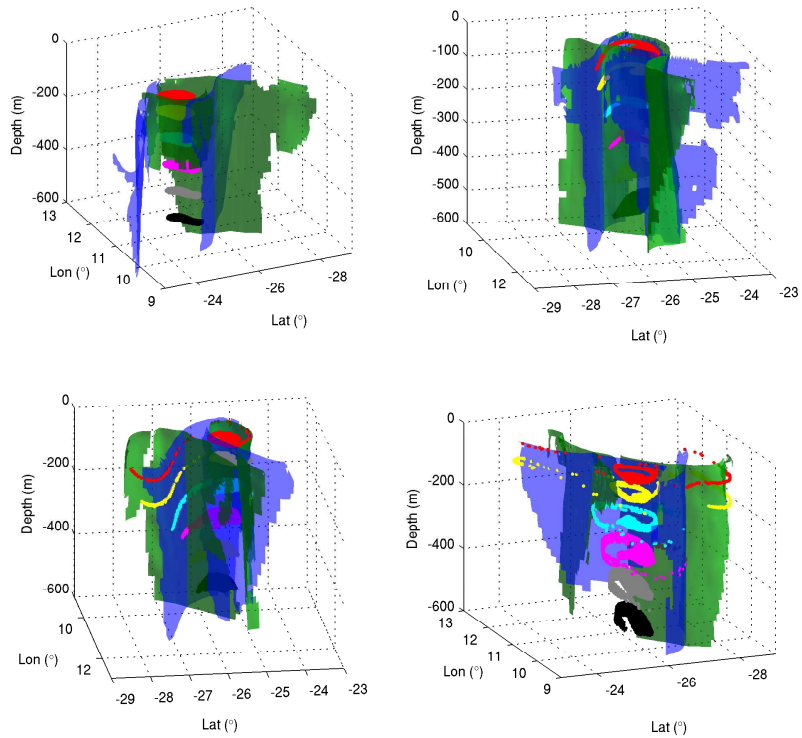


Figure 4.8: Three dimensional view of the evolution of elliptic patches released at different depths inside of the eddy at day 1 of the 30 day FSLE calculation period. Top left: day 3; Top right: day 13; Bottom left: day 19; Bottom right: day 29. Red: 40 m; Yellow: 100 m; Cyan: 200 m; Magenta: 300 m; Grey: 400 m; Black: 500 m. Attracting LCS are shaded in blue while repelling LCS are shaded in green.

4.4. DISCUSSION.

at the same time and at the same horizontal positions, and thereby their different behavior is due to the variations of the LCS properties along depth.

At day 13 the vortex starts to expel material through filamentation (Figs.4.8 and 4.9, top right panels). A fraction of the particles approach the southern boundaries of the eddy from the northeast. Those to the west of the repelling LCS (green) turn west and recirculate inside the eddy along the southern attracting LCS (blue). Particles to the east of the repelling LCS turn east and leave the eddy forming a filament aligned with an attracting (blue) LCS. At longer times trajectories in the south of the eddy are influenced by additional structures associated to a different southern eddy. At day 29 (bottom right panels) the same process is seen to have occurred in the northern boundary, with a filament of particles leaving the eddy along the northern attracting (blue) LCS. The filamentation seems to begin earlier at shallower waters than at deeper ones since the length of the expelled filament diminishes with depth. However all of the expelled filaments follow the same attracting LCS. Figure 4.10 shows the stages previous to filamentation in which the LCS structure, their tangencies and crossings, and the paths of the particle patches are more clearly seen. Note that the LCS do not form fully closed structures and the particles escape the eddy through their openings. The images suggest lobe-dynamics processes, but much higher precision in the LCS extraction would be needed to really see such details.

This filamentation event seems to be the only responsible for transport of material outside of the eddy, since the rest of the particles remained inside the eddy boundaries. To get a rough estimate of the amount of matter expelled in the filamentation process we tracked the percentage of particles leaving a circle of diameter 200 km centered on the eddy center. In Fig. 4.11 the time evolution of this percentage is shown for the particle sets released at different depths. The onset of filamentation is clearly visible around days 9-12 as a sudden increase in the percentage of particles leaving the eddy. The percentage is maximum for the particles located at 100 m depth and decreases as the depth increases. At 400 and 500 m depth there are no particles leaving the circle. There is a clear lag between the onset of filamentation between the different depths: the onset is simultaneous for the 40 m and 100 m depths but occurs later for larger depths.

4.4

Discussion.

The spatial average of FSLEs defines a measure of stirring and thus of horizontal mixing between the scales used for its computation. The larger the average, the

CHAPTER 4. OCEANIC 3D STRUCTURES

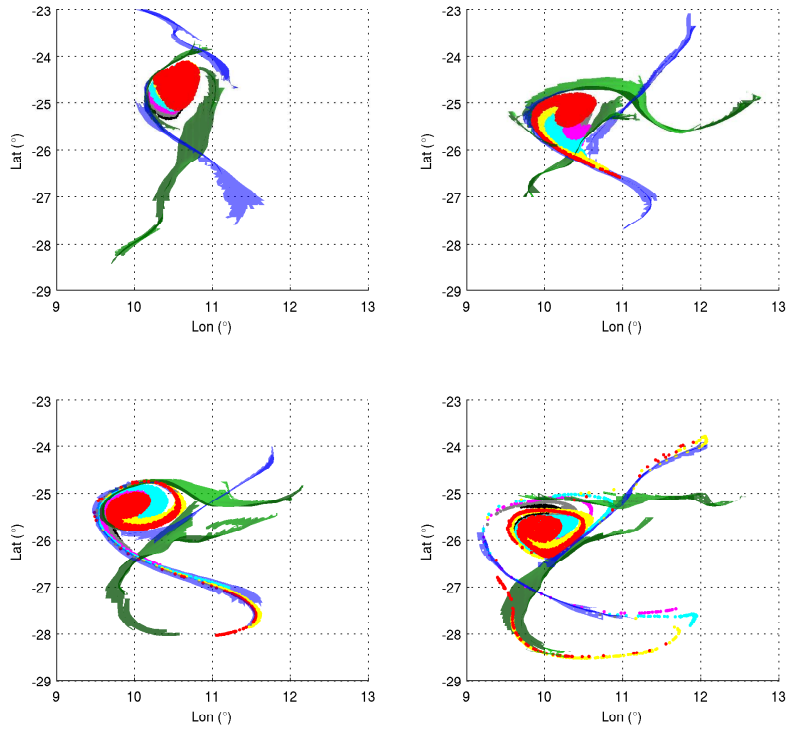


Figure 4.9: Top view of the evolution of particle patches and LCSs shown in Fig. 8. Top left: day 3; Top right: day 13; Bottom left: day 19; Bottom right: day 29. Colors as in figure 4.8.

4.4. DISCUSSION.

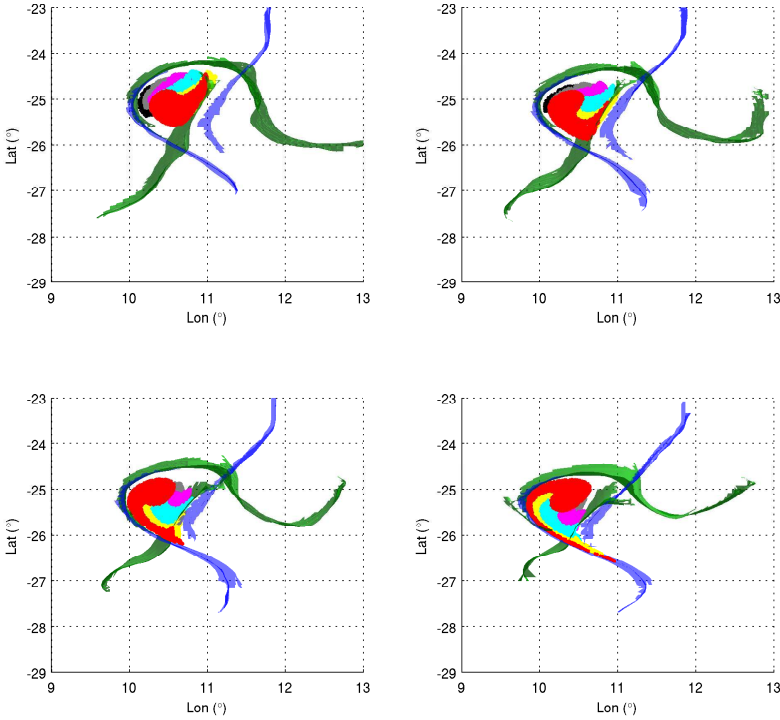


Figure 4.10: Top view of the initial stages of evolution of the particle patches and LCSs of Figs. 8 and 9. Top left: day 7; Top right: day 9; Bottom left: day 11; Bottom right: day 13. Colors as in figure 4.8.

CHAPTER 4. OCEANIC 3D STRUCTURES

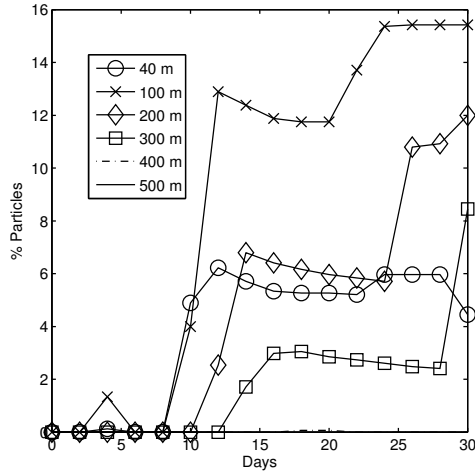


Figure 4.11: Percentage of particles outside a 200 km diameter circle centered at the eddy center, as a function of time.

larger the mixing activity [54]. The general trend in the vertical profiles of the average FSLE (Fig. 4.3) shows a reduction of mesoscale mixing with depth. There is however a rather interesting peak in this average profile occurring at 100 m, i.e. close to the thermocline. It could be related to submesoscale processes that occur alongside the mesoscale ones. Submesoscale is associated to filamentation (the thickness of filaments is of the order of 10 km or less), and we have seen that the filamentation and the associated transport intensity (Fig. 4.11) is higher at 100 m depth. It is not clear at the moment what is the precise mechanism responsible for this increased activity at around 100 m depth (perhaps associated to instabilities in the mixed layer), but we note that the intensity of shearing motions (see the Q plots in 4.5) is higher in the top 200 meters. Less intense filamentation could be caused by reduction of shear in depths larger than these values.

From an Eulerian perspective, it is thought that vortex filamentation occurs when the potential vorticity (PV) gradient aligns itself with the compressional axis of the velocity field, in strain coordinates [133, 134]. This alignment is accompanied by exponential growth of the PV gradient magnitude. The fact that the filamentation occurs along the attracting LCS seems to indicate that this exponential growth of the PV gradient magnitude occurs across the attracting LCS.

4.4. DISCUSSION.

In the specific spatiotemporal area we have studied, and in particular, for the eddy on which we focused our analysis, we have confirmed that the structure of the LCSs is “curtain-like”, so that the strongest attracting and repelling structures are quasi vertical surfaces. Their vertical extension would depend of the physical transport properties, but it is also altered by the particular threshold parameter selected to extract the LCSs. These observations imply that transport and stirring occurs mainly on the horizontal, which is a reasonable result considering the disparity between horizontal and vertical velocities in the ocean, and its stratification. However, we should mention that our results are not fully generalizable to all ocean situations, and that any ocean area or oceanic event should be studied in particular to reveal the shape of the associated 3d LCS.

Some comments follow about the nature of vertical transport structures. FSLEs are suited to the identification of hyperbolic structures (structures that exhibit high rates of transversal stretching or compression in their vicinity). The question is if one can expect that structures responsible for vertical transport will also exhibit substantial (vertical) stretching. This is not so clear in the ocean for the reasons already indicated. If one considers the case (relevant to our work) of purely isopycnal flow, then strong vertical stretching would be associated with a rapid divergence of isopycnic surfaces. In the case of coastal upwelling, for instance, the lifted isopycnic surfaces move vertically in a coherent fashion, so one should not expect strong vertical divergence of particles flowing along neighboring isopycnic surfaces. This is just an example of the fact that it is possible that coherent vertical motions do not imply the presence of hyperbolic coherent structures such as those the FSLE may indicate.

Another possible limitation worth mentioning is the velocity field resolution and its relation to the intensity of the vertical velocity. It is accepted that in fronts or in the eddy periphery, vertical velocities are significantly greater than, for instance, in the eddy interior. These zones of enhanced vertical transport correspond to submesoscale features that were not adequately captured in the velocity field used in this work due to its coarse resolution, since submesoscale studies usually have resolutions < 10 km (the literature on this subject is quite large, so we refer the reader to [16] and [20]).

In any case, a most important point for the LCS we have computed is that in 3d, as in 2d, they act as pathways and barriers to transport, so that they provide a skeleton organizing the transport processes.

Conclusions

Three dimensional Lagrangian Coherent Structures were used to study stirring processes leading to dispersion and mixing at the mesoscale in the Benguela ocean region. We have computed 3d Finite Size Lyapunov Exponent fields, and LCSs were identified with the ridges these fields. LCSs appear as quasi vertical surfaces, so that horizontal cuts of the FSLE fields gives already a quite accurate vision of the 3d FSLE distribution. These quasi vertical surfaces appear to be coincident with the maximal lines of the FSLE field (see fig. 4.3) so that surface FSLE maps could be indicative of the position of 3d LCS, as long as the vertical shear of the velocity does not result in a significant deviation of the LCS with respect to the vertical. Average FSLE values generally decrease with depth, but we find a local maximum, and thus enhanced stretching and dispersion, at about 100 m depth.

We have also analyzed a prominent cyclonic eddy, pinched off the upwelling front and study the filamentation dynamics in 3d. Lagrangian boundaries of the eddy were made of intersections and tangencies of attracting and repelling LCS that apparently emanating from two hyperbolic locations North and South of the eddy. The LCS are seen to provide pathways and barriers organizing the transport processes and geometry. This pattern extends down up to the maximum depth were we calculated the FSLE fields (~ 600 m), but the exact shape of the boundary is difficult to determine due to the decrease in ridge strength with depth. This caused some parts of the LCS not to be extracted. The inclusion of a variable strength parameter in the extraction process is an important step to be included in the future.

The filamentation dynamics, and thus the transport out of the eddy, showed time lags with increasing depth. This arises from the vertical variation of the flow field. However the filamentation occurred along all depths, indicating that in reality vertical sheets of material are expelled from these eddies.

Many more additional studies are needed to further clarify the details of the geometry of the LCSs, their relationships with finite-time hyperbolic manifolds and three dimensional lobe dynamics, and specially their interplay with mesoscale and submesoscale transport and mixing processes.

We thank the LEGOS group for providing us with 3D outputs of the velocity fields from their coupled BIOBUS/ROMS climatological simulation.

Mesoscale stirring in the Peru Oxygen Minimum Zone

This chapter is based on

João H. Bettencourt, Cristóbal López, Emilio Hernández-García, Ivonne Montes, Joël Sudre, Boris Dewitte, Aurélien Paulmier, and Véronique Garçon. Mesoscale eddies as barriers to mixing in the Eastern Tropical Pacific Oxygen Minimum Zone. *Nature Geosciences*, Submitted.

The oxygen content of sea water is a major factor affecting marine fauna and biogeochemical cycles. Zones where an oxygen deficit is present in the water column represent significant portions of the total area and volume of the world oceans and are thought to be increasing. In the Eastern Tropical Pacific an Oxygen Minimum Zone is found. The area is populated by numerous mesoscale eddies whose role on the exchange of water mass properties remains largely unknown. We study this problem from a modeling approach and a Lagrangian point of view, characterizing pathways and barriers to transport and mixing of oceanic regions with distinct concentrations of dissolved oxygen. Our results show that, at certain depths, mesoscale structures have a relevant and dual role: On the one hand their mean positions and paths are important to maintain the Oxygen Minimum Zone frontiers. On the other their fluctuations eventually entrain oxygen across these frontiers as eddy fluxes, that we estimate.

Introduction

Low concentrations of dissolved O_2 in the world coastal waters have severe consequences to marine life. Hypoxic levels ($O_2 < 88 \mu M$) [135] are lethal to about half of marine benthic species and a fraction of them exhibits extreme sensitivity to hypoxia with lethal concentrations as high [136] as $140 \mu M$. O_2 deficiency also has profound impacts on marine biogeochemical cycles since denitrification only occurs in O_2 poor waters so it is a contributor to the fixed nitrogen deficit together with the anammox process [137, 138]. Regions of the ocean where O_2 deficiency in the water column can be found are called Oxygen Minimum Zones (OMZs). The OMZs are differentiated in the vertical by three distinct layers: the oxycline (upper O_2 gradient), the core (with typically $O_2 < 20 \mu M$) and the lower O_2 gradient. The total area and volume of the known OMZs amount to 8% and 7% of the global ocean, respectively [139]. It is believed that these values might increase in the future due to rising temperatures which decrease O_2 solubility, in addition to the enhancing of the stratification [140, 141].

The Eastern Tropical South Pacific (ETSP) contains one of the three major permanent OMZ, with an oxycline layer extending from the upper 10 to 170 meters, followed by a core with a thickness of 340 meters [139]. The lower oxygen gradient (values larger than $0.1 \mu M/m$) extends to about 3700 meters [139]. This OMZ is maintained by the combination of significant rates of biological production and decomposition of sinking organic material [142] at the upwelling region off Peru, and weak circulation in the shadow zone of the eastern Southern Pacific subtropical gyre. The circulation is then dominated by the equatorial and eastern boundary current systems [143]. Mesoscale eddies and filaments are ubiquitous in this area [144]. In contrast to the oligotrophic regions of the ocean where eddies can sustain biological productivity [38], in upwelling regions stirring by eddies tends to reduce biological production [31, 32]. Recent observations off Peru confirmed that coastal eddies are acting as hotspots of nitrogen loss [145, 146], whereas open water and cyclonic eddies seem to be of reduced importance or even negligible, respectively, as hotspots of active nitrogen loss. In the ETSP the role played by mesoscale eddies in the distribution of O_2 within the OMZ remains unclear and we approach this problem by analyzing data coming from a coupled physical-biogeochemical high-resolution model of the regional ETSP OMZ [147], and characterizing mesoscale transport and stirring by means of Finite-size Lyapunov exponent (FSLE) fields [54, 96]. Maxima in these fields form filamentary structures, the so-called Lagrangian Coherent Structures (LCSs) [51, 54, 55] identifying the most active mesoscale regions and acting as barriers for fluid transport across them.

In this chapter we focus in the transport aspects of the mesoscale-OMZ interaction, particularly in the OMZ boundaries, and the fluxes across them. Then we do not address the biogeochemical processes occurring inside the OMZ which are certainly determinant in the area dynamics (and are included in our regional simulation model) but we gauge instead the physical effects of the mesoscale structures on the OMZ dynamics. This is done by: a) computing correlations between the (statistically averaged over time) O_2 concentration and FSLE at layers located at different depths; b) studying events of O_2 rich-waters entrainment into the OMZ; c) calculating the (temporally averaged) O_2 normal fluxes across the northern and southern frontiers of the OMZ as a function of the depth and its correlation with the average mixing measurement obtained from FSLE. The relationship between the FSLE characterization and other Lagrangian diagnosis provided by residence times is also discussed.

5.2

Data

5.2.1 Circulation and Oxygen Minimum Zone modeling

The circulation and OMZ modeling in the Eastern Tropical Pacific was accomplished by the combination of the hydrodynamic model ROMS [115] (Regional Ocean Modeling System) and the biogeochemical model developed [148] for the Eastern Boundary Upwelling Systems (BioEBUS). The Eastern Tropical Pacific configuration covers the region from 4° N to 20° S and from 70° to 90° W with an horizontal resolution of $1/9^\circ$ degrees (≈ 12 km) and 32 terrain-following vertical levels with variable vertical resolution (higher in the upper ocean). The coupled model is run in a climatological configuration previously validated [149] for the Eastern Tropical South Pacific, and the present configuration has been recently validated and a sensitivity analysis was performed [147]. The model was forced by the QuickSCAT [150] wind stress monthly climatology and by heat and fresh water fluxes from the COAD [151] monthly climatology. The dynamical variables at the three open ocean boundaries are provided by a monthly climatology computed from the Simple Ocean Data Assimilation reanalysis [152]. For the biogeochemical model, boundary conditions of nitrate and oxygen concentrations are taken from CSIRO Atlas of Regional Seas (CARS 2009, <http://www.cmar.csiro.au/cars>) and chlorophyll a concentration from SeaWiFS (<http://oceancolor.gsfc.nasa.gov/>). The simulations were performed for a 22-year period. The first 13 years were run with the physics only and the following 9-years were run with the physi-

CHAPTER 5. STIRRING IN THE PERU OMZ

cal/biological coupling. The coupled model reached a statistical equilibrium after 4 years and model outputs were stored every 3 days (averaged).

5.2.2 3d FSLE fields

We computed daily three-dimensional (3d) fields of backward FSLE for simulation year 21. This was done by setting up a regular 3d latitude-longitude-depth grid of initial conditions with spacing in the two horizontal directions of $\delta_0 = 1/27^\circ$ (i.e. ≈ 4 km) and 30 vertical layers with variable vertical spacing. The grid covered the ETSP from 88° W to 70° W and 18° S to 2° N. Vertically, the grid extended from 10 to 1100 m depth and was clustered in the upper 500 m of ocean. To obtain the FSLE field, $\lambda(\mathbf{x}, t)$, at location \mathbf{x} and time t , one particle is released at time t from each grid node at location \mathbf{x} and the separation to the particles released from neighboring nodes is monitored. τ is the time needed for the first of these separations to reach the value δ_f (that in this study was set at 100 km). Trajectories were integrated backward in time for 6 months with a Runge-Kutta 4th order method. If at the end of this interval the separations are smaller than δ_f , or if the particles leave the domain or hit the shore, then the FSLE for the release location is set to zero.

5.3

Results

5.3.1 Backward FSLE 3d fields

Maximum values of FSLEs computed backwards in time can be interpreted as fronts of advected tracers, since they delineate the lines along with the tracers are stretched and folded by the fluid flow.

A map of instantaneous backward FSLE is shown in Fig. 5.1 for different depths. In the upper layer (Fig. 5.1 A) we observe that below 4° S the FSLE field is organized in thin filamental features with high FSLE value superimposed on a low FSLE background. Above 4° S, we see a larger density of small-scale features, that represent the change in dynamical regime [153] as we approach the equator. Time scales associated with the Lagrangian dynamics at this depth vary from 4 to 10 days (the FSLE is roughly an inverse time scale). At higher depths (Fig. 5.1 B, C and D) the features of the instantaneous FSLE field are maintained although the intensity is reduced from its values at the surface. The area near the equator with dense small-scale structure is reduced at 113 m depth

5.3. RESULTS

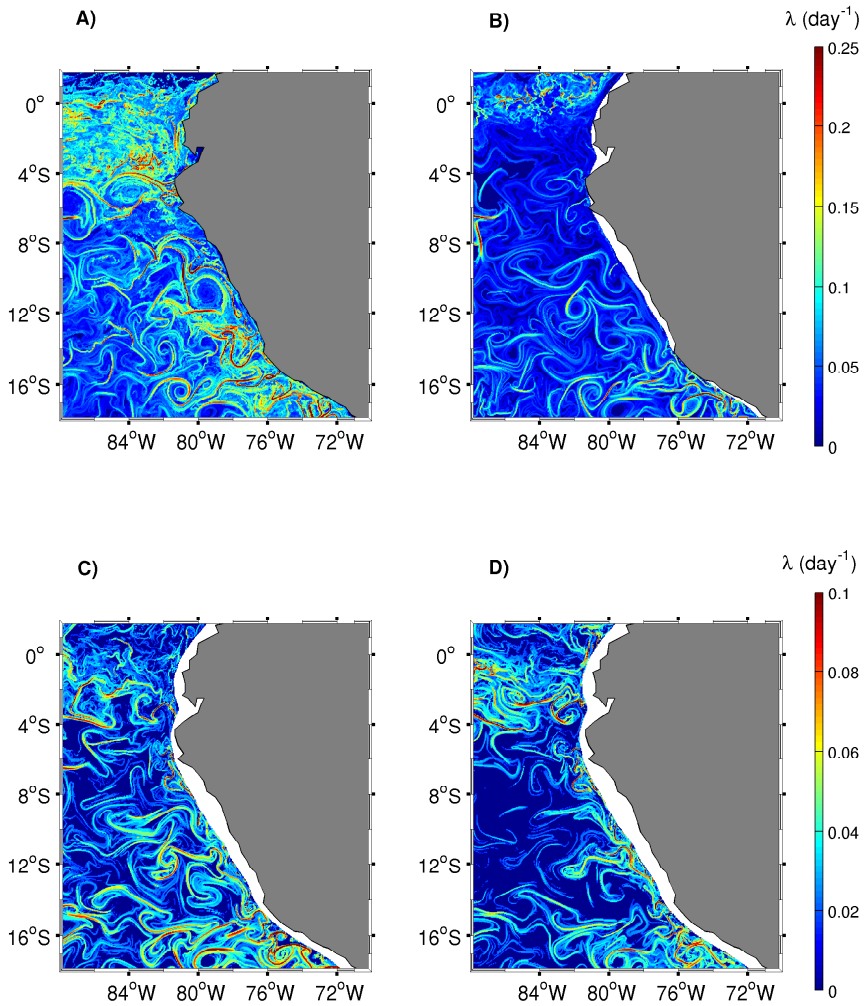


Figure 5.1: Map of backward FSLE for the 1st of January of year 21. A) 10 m depth. B) 113 m depth. C) 410 m depth. D) 592 m depth. Note the different colorbar at different depths.

CHAPTER 5. STIRRING IN THE PERU OMZ

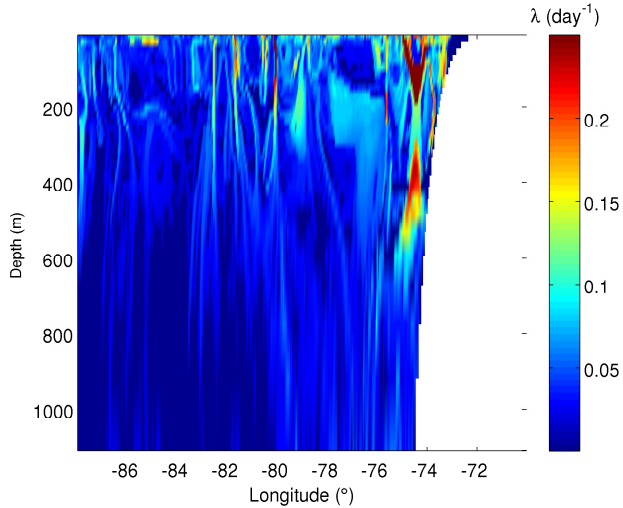


Figure 5.2: Vertical map of backward FSLE for the 1st of January of year 21, at 16.45° S.

and qualitatively different or non-existent at 410 and 592 m depth (Fig. 5.1 B, C and D, respectively). At all depths shown, the high FSLE lines are more common near the coast, which in this region is the main source of mesoscale variability due to instability of coastal currents and the associated upwelling regime [144, 154].

The vertical structure of the instantaneous FSLE field is shown in Fig. 5.2 for the same date and a cut at 16.45° S. The thin filamental structures appearing in the horizontal maps have a vertical extension of about 400 m from the surface down. The structures oriented parallel to the zonal axis reveal this *curtain* like shape, as can be observed between 76° W and 78° W and 100 and 300 m depth. Such shape has already been observed (in 3d) in similar calculations for the Benguela upwelling zone [113] and can be justified theoretically [65]. Dynamical studies with particle trajectories showed that the most intense *curtains* can be related to Lagrangian eddy boundaries.

The temporal-mean horizontal maps of the backward FSLE fields are shown in Figure 5.3 for four depths: 10, 113 and 410 and 592 m. One can observe the most persistent patterns of mixing, in particular, the northern and southern strips delineating the frontiers of the OMZ. The depth profile of horizontally averaged mean FSLE field for simulation year 21 (Figure 5.4) shows the decrease in stirring with depth, with a subsurface peak at ≈ 30 m depth. This decrease of stirring with depth, as measured by the FSLE, was also found in a study of the Benguela

5.3. RESULTS

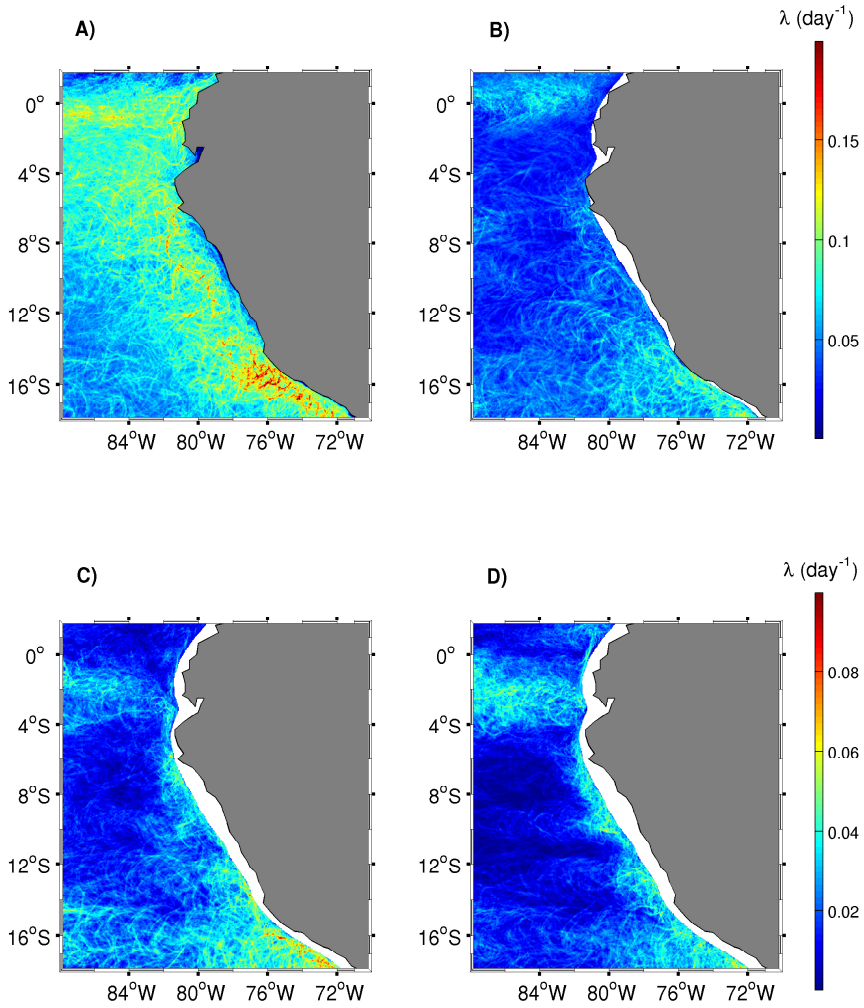


Figure 5.3: Horizontal maps of backward FSLE temporally averaged for year 21. A) 10 m depth. B) 113 m depth. C) 410 m depth. D) 592 m depth. Note the different colorbar at different depths.

CHAPTER 5. STIRRING IN THE PERU OMZ

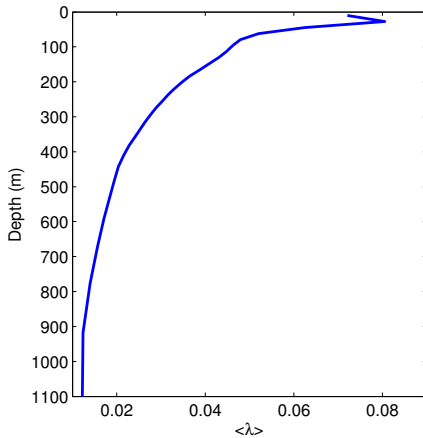


Figure 5.4: Time mean of the horizontally averaged depth profile of the backward FSLE field $\langle \lambda \rangle$ (in day^{-1}) for year 21.

upwelling region [113]. Its origin could be simply the overall smaller velocities found at deeper layers, and also the decrease in the nonlinearity of the mesoscale eddies (as indicated for example by its ratio between rotation and propagation velocities) that occurs with depth [144].

5.3.2 Exit times

Residence times (RT) are a tool to study fluid exchange between two regions. Although the OMZ does not constitute a geographically determined region such as a basin or bay, it is still possible to define appropriate limits to the OMZ (as we have done all along this chapter) so that fluid exchange between the OMZ and its exterior may be studied with RT distributions [155, 156]. They are Lagrangian diagnosis complementary to the FSLE methods. The RT of a fluid particle is defined as the time it spends inside a certain region before crossing a particular boundary. Here we compute the RT in the OMZ as the time the particle remains with a O_2 content below $20 \mu M$. The results obtained are similar if instead the exit is computed from the average OMZ core region, i.e. the volume in which the temporally averaged O_2 concentration is smaller than $20 \mu M$. Trajectories can be integrated forward in time (and then the computed time is properly an exit time) or backward in time (so that one is calculating then the residence time the particle has been in the region before present).

5.3. RESULTS

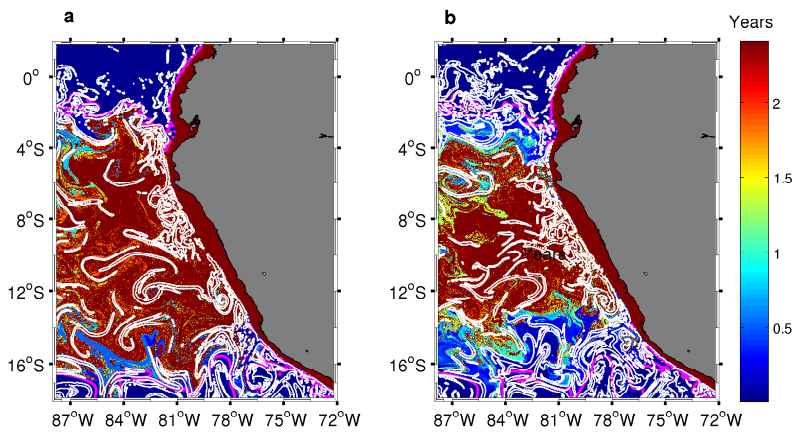


Figure 5.5: Residence times (RT) at 410 m depth for 1st July of year 20. A) Backward RT. Superimposed white lines are 0.035 day^{-1} backward FSLE isolines. B) Forward RT. Superimposed white lines are 0.038 day^{-1} forward FSLE isolines. The magenta lines bound the region inside which the concentration of O_2 was smaller than $20 \mu M$ already at the initial time, so that outside these lines the exit times are zero. The red color associated to a residence time of 2.5 years is in fact associated also to all residence times larger than this duration.

CHAPTER 5. STIRRING IN THE PERU OMZ

We show in Fig. 5.5 the RT distribution at 410 meters depth for the 1st of July of simulation year 20. Similar results are observed at other depths. To obtain this distribution, particles were released from the same horizontal regular grid described in the previous section and the trajectories were integrated backward and forward for 2.5 years (the need to use such large integration times forced us to use as initial time year 20 instead of year 21 as in other calculations, since the simulation dataset contains only 22 years). Backward and forward FSLE fields were also computed for this date and location for comparison purposes.

The RT are larger than 2.5 years in most of the area identified as the OMZ core. In contrast with this rather homogeneous distribution in the centre, at the OMZ boundaries the RT distribution assumes quite complex shapes, where several reentrant zones of low RT and sharp transitions to low RT. Additionally, there are several cases of thin regions of low RT intruding in to the high RT central zone. These sharp boundaries between high and low RT coincide in some areas with high FSLE values. This coincidence is a feature observed with the RT distributions of passive particles in a given geographical region [156]. Since passive particles are Lagrangian tracers, we conclude that in the areas of matching RT changes and FSLE lines, the O_2 content is conserved along particle trajectories and local changes in O_2 occur mostly due to advection. The long residence times found are consistent with the low ventilation regime needed for the biogeochemistry in the area to reduce oxygen concentrations to hypoxic levels.

5.3.3 Correlations between mean FSLE and O_2 fields

The 20 μM isosurface of the annual mean O_2 field for simulation year 21 (Fig. 5.6a gives an OMZ core with maximal meridional extension at approximately 400 m depth extending between 3° S and 16° S. The higher O_2 concentrations north of 2° S are associated to subsurface eastward equatorial currents carrying relatively oxygen-rich water [157], while the southern increase of O_2 (14° S to 17° S) is adjacent to the northern part of the subtropical gyre. Figure 5.6a displays also the annual mean backward FSLE field at 410 m depth, which shows a remarkable relation to the mean O_2 field delineating the limits of the OMZ core. The FSLE mean field is structured as zonal bands coincident with the north and south OMZ boundaries with relatively high FSLE values when compared to the core region. Both bands are signals of the eddies released from their formation region near the continental shelf and advected offshore [144, 158]. This indicates that the enhanced mesoscale activity in those areas delineate the limits of the average OMZ region at core depths. To further quantify the relationship between mesoscale dynamics and the frontiers of the OMZ we note that since LCSs (that we locate as maximum values of FSLEs) act as transport barriers, large gradients of O_2

5.3. RESULTS

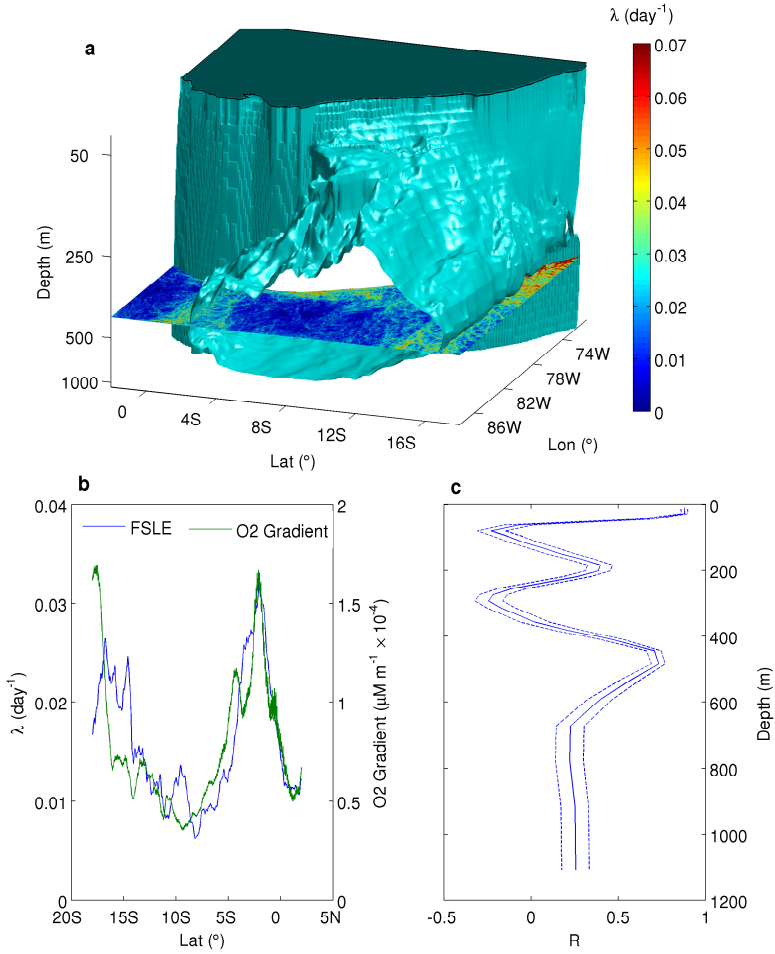


Figure 5.6: Mean O_2 and FSLE fields and correlations for simulation year 21. a) $20 \mu\text{M}$ isosurface of mean O_2 concentration rendered together with an horizontal plane at 410 meters depth displaying the mean FSLE field. The vertical scale is nonlinear and stretched in the upper 500 m depth. The solid volume with the flat top is the Peruvian coast. b) Zonally averaged mean FSLE and O_2 gradient, averaged between 380 m and 600 m depth. c) Pearson correlation coefficient (R) between zonally averaged mean FSLE and O_2 gradient as a function of depth (solid line). Upper and lower bounds of R give the Fisher 95% confidence interval (dashed-lines).

CHAPTER 5. STIRRING IN THE PERU OMZ

should occur across such structures [159]. Thus we expect to find a relationship between the stirring intensity as measured by the FSLE and the O_2 gradient norm (in the following any mention to the O_2 gradient should be understood as referring to its modulus or norm). The relationship between both averaged fields is quantified in Fig. 5.6 B where we plot the meridional profiles of mean FSLEs and O_2 gradient averaged in a part of the OMZ core, showing the coincidence in the maxima of both quantities: the maxima of FSLE indicating the positions of the LCSs and the maxima of the gradients of O_2 signalling the northern and southern frontiers of the OMZ. This correlation is not equally strong at all depths as it is shown in Fig. 5.6 C, where we plot the vertical profile of the Pearson correlation coefficient, R , between the zonally averaged mean FSLE and mean gradient of O_2 concentration. Roughly, we can distinguish two areas in the OMZ core: a) between 190 – 350 meters where these quantities show correlations of alternating sign; and b) between 380 – 600 meters where the correlation is large and positive (with an average R of 0.748). It is in this subarea of the OMZ where the mesoscale dynamics contributes more intensely to determine its boundaries.

To explore further the relationship between FSLE and O_2 horizontal gradients, first we observe in Fig. 5.7 A) how the lines of high FSLE values determine instantaneous (at depth 410 m) fronts for the O_2 concentrations. These are located in the northern and southern frontiers of the OMZ as has been discussed all along the text. In Fig. 5.7 B) it is shown how the high-FSLE lines coincide with the largest horizontal gradients of O_2 .

In Fig. 5.8 A) and B) we show FSLE and O_2 gradient maps, respectively, averaged temporally (for simulation year 21) and vertically in the mid-depth range of the OMZ (between 350 and 600 m). We do not discuss the relationship between the high values of FSLE and of O_2 gradients found very close to the coast, since that region has a very different dynamics and biogeochemistry, and it is influenced by the presence of coastal currents. The maps clearly show the high gradient zones north and south of a central basin with low average O_2 gradient that coincides with the OMZ. The northern band is located approximately at an interface between an eastward mean zonal flow relatively rich in O_2 [143, 157] and a southern adjacent westward mean flow. This flow configuration at middepth present in our simulation data shows similarities with ADCP data [158] taken in February 2009 that show a eastward flow and an adjacent westward flow with velocities about 2.5 *cm/s*. The mean FSLE field for the same depth range (Figure 5.8 A) shows that the band between 0° and 4° S is a zone of high FSLE. On the southern boundary, high O_2 gradients are located close to the equatorward edge of the southern subtropical gyre, along a zonal band below 16° S. In this region, we also find high values of the mean FSLE but these are distributed along a wider zonal region, poleward from 14° S.

5.3. RESULTS

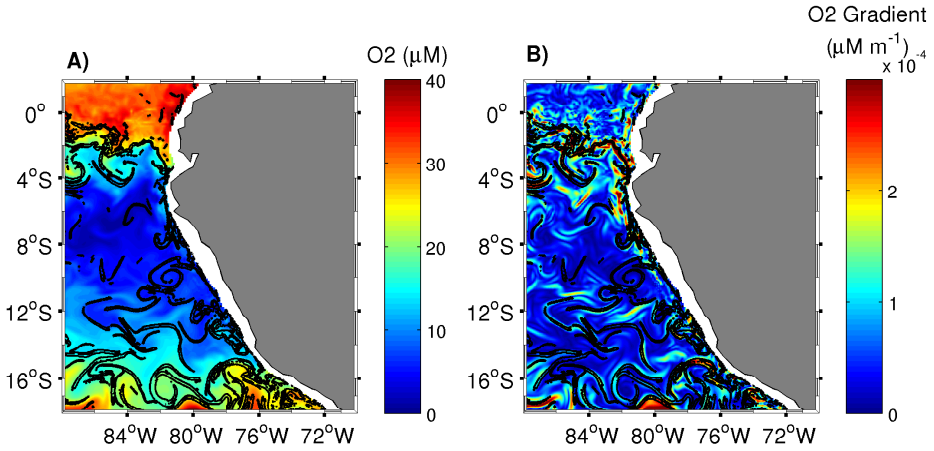


Figure 5.7: Lines of high FSLE values ($> 0.04 \text{ day}^{-1}$, black) superimposed on instantaneous O_2 and O_2 gradient fields on 1st of March of year 21 at 410 m depth. A) O_2 concentration. B) O_2 horizontal gradient.

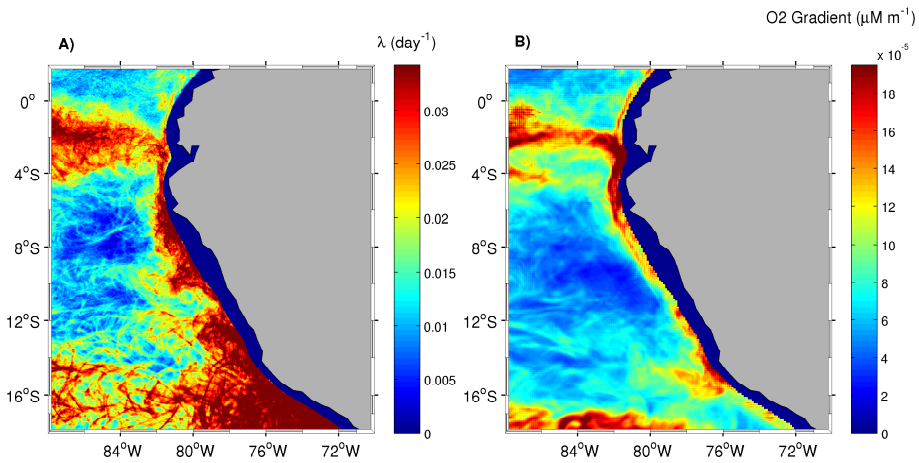


Figure 5.8: Mean fields averaged over 300–600 meters depth and during year 21. A) FSLE. B) O_2 horizontal gradient.

CHAPTER 5. STIRRING IN THE PERU OMZ

The center of the OMZ forms a basin of low O_2 gradients and also low FSLE. The low values of O_2 are found due to low or inexistent ventilation (as quantified by large residence times) of this region coupled to the respiration of sinking organic matter. The low FSLE distribution is due to the absence of significant mesoscale activity at this depth. Although this region is located offshore of the Peru upwelling strip, and receives anticyclonic eddies formed in instabilities of the coastal currents [160], mesoscale activity as measured by eddy intensity decreases as we move offshore [144], and it is only intense in the two strips surrounding the OMZ.

5.3.4 Ventilation by eddies and eddy fluxes

Besides mean behaviour, individual events are also of maximum relevance, since mesoscale eddies are able to transport waters with different biogeochemical properties with respect to surrounding areas, and to entrain water around them. This could give rise to sporadic episodes of high O_2 patches inside the OMZ. In Fig. 5.9 we show one of these temporal sequence where an eddy dipole (with borders signalled by maxima of FSLE at 410 meters) entrains water with large oxygen content (the red-yellow tongue at $80 - 82^\circ\text{W}$) towards the interior of the OMZ. This episode had a duration of approximately 3 months (from the 9th of September to the 1st of December of simulation year 21; in the figure only the first month is displayed) and our calculations show that during this period the entrainment of these waters carried 0.4×10^6 mol of O_2 per meter of depth into the OMZ at this depth. We characterize the eventual entrainment of water across the OMZ boundaries by displaying in Fig. 5.10 Hovmöler plots of the time evolution of the O_2 anomaly at the North (panel A) and South (panel B) OMZ $20\mu\text{M}$ boundaries at 410 m depth. The anomaly is the actual O_2 concentration minus the mean at that location ($20\mu\text{M}$). Since the overall eddy fluxes point towards the OMZ interior, positive anomalies indicate oxygenated water entering into the OMZ. The slopes in the Hovmöler plots indicate overall westward propagation.

O_2 anomalies are more variable for the northern boundary (standard deviation of $4.8 \mu\text{M}$) than for the southern boundary (standard deviation of $3.1 \mu\text{M}$). This difference is probably related to the fact that at the North boundary, the O_2 content of northern adjacent waters is much higher than the OMZ levels while at the South boundary this difference is not so strong. Additionally, at the North boundary the O_2 front is more stable meaning that there is an available pool of O_2 rich waters readily available to be entrained into to the OMZ by propagating mesoscale structures. At the southern boundary the O_2 anomaly seems to be dependent on the actual O_2 content of traveling eddies that occasionally approach the boundary.

5.3. RESULTS

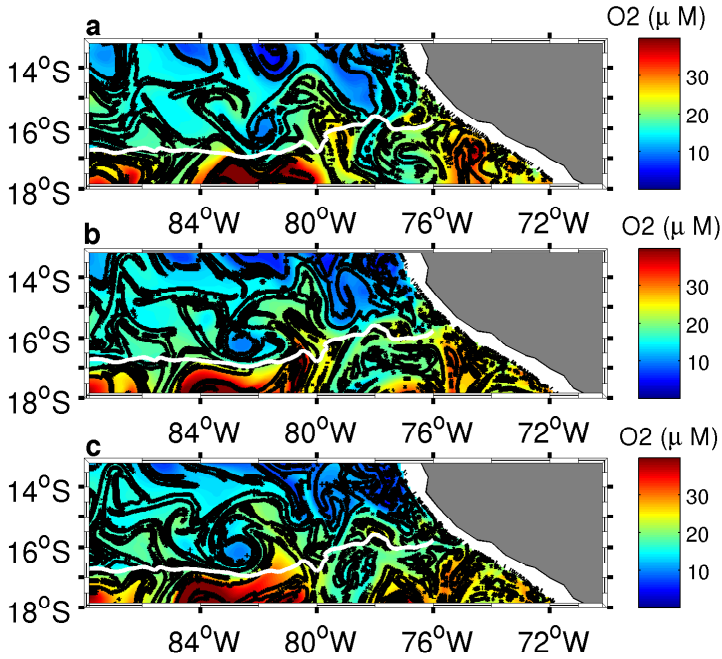


Figure 5.9: Entrainment of O_2 rich waters into the OMZ due to LCS motion. Color codifies O_2 at 410 m depth and the lines are the 0.075 day^{-1} FSLE isolines. a) 16 September; b) 7 October; c) 25 October; all of simulation year 21. Note the oxygen-rich tongue entering the OMZ at $80 - 82^\circ W$. White continuous line is the $20 \mu M$ mean isocline at 410 m depth (corresponding to the southern OMZ frontier).

CHAPTER 5. STIRRING IN THE PERU OMZ

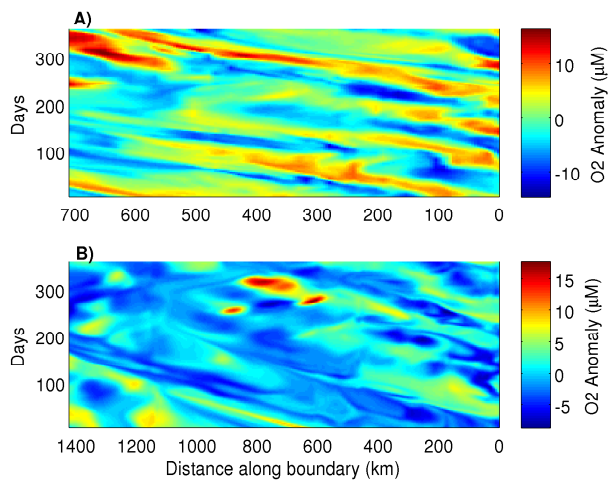


Figure 5.10: Hovmöller plots of O_2 concentration anomalies at OMZ boundaries at 410 m depth during simulation year 21. A) Northern boundary. B) Southern boundary. Anomaly measured relative to $20 \mu M$ level. Distance along boundary increases towards offshore. So, coast is at the right and the anomalies propagate offshore.

5.3. RESULTS

At the northern boundary the anomalies last longer than at the southern one and remain more coherent during their propagation offshore. In the South, ventilation events are more intermittent. However, during the year under analysis, the greatest episode of O_2 anomaly crossing the OMZ at this depth occurred in the southern boundary with peak O_2 anomaly of $\sim 17 \mu M$ around day 300 and between 600 and 800 km from the coast (this is the episode depicted in Figure 5.9).

The observation of ventilation events into the OMZ by eddy activity are important to elucidate the physical mechanisms that promote them, but a composite picture of their effect can only be achieved by a statistical analysis of several events during a relevant time period. A quantification of the mean amount of O_2 entering through the OMZ frontiers due to turbulent processes was carried out by the computation of eddy fluxes of O_2 normal to the northern and southern boundaries. We computed O_2 eddy (or turbulent) fluxes by using the Reynolds transport theorem and the decomposition of the velocity and O_2 concentration fields in their mean and fluctuating components. We calculate them across the mean $20 \mu M$ level boundary between 200 and 600 meters of depth during simulation year 21. Eddy fluxes are computed from the covariance between horizontal velocity anomalies and O_2 concentration anomalies. The eddy flux across each of the mean $20 \mu M$ north and south boundaries was computed by averaging the product of the fluctuating velocity component normal to the boundary and the fluctuating O_2 concentration component. We choose signs so that positive fluxes are towards the interior of the OMZ, and negative fluxes point towards the outside. At the northern boundary the eddy flux profile is mainly positive (Fig. 5.11a, red line), meaning that the O_2 variance due to horizontal turbulent fluxes is bringing O_2 into the OMZ. The highest eddy fluxes are reached at core depths between 350 and 500 meters which is close to the depth range where the higher FSLE mean values at the boundary are obtained (Fig. 5.11a, blue line), although the maximum value of this latter quantity appears deeper than the eddy flux maximum (350 vs 480 meters). Above 300 meters the normal eddy fluxes are small and the minimum is obtained around 300 meters, where the FSLE is minimum also.

The profiles of mean and eddy fluxes across the $20 \mu M$ OMZ boundaries for depths between 200 and 600 meters were computed for simulation year 21 and shown in Fig. 5.12. The fluxes are averaged also along the horizontal extension of the boundary at each depth. Blue lines are for the northern boundary and red for the southern one. Overall, the mean fluxes are much smaller than the eddy ones. In the northern boundary, eddy fluxes and mean fluxes and both positive up to about 250 m depth. At deeper locations the eddy flux is again positive, and the mean flow slightly negative (i.e. pointing outside the OMZ). At the southern boundary the eddy flux is positive above 380 m, becoming negligible further down.

CHAPTER 5. STIRRING IN THE PERU OMZ

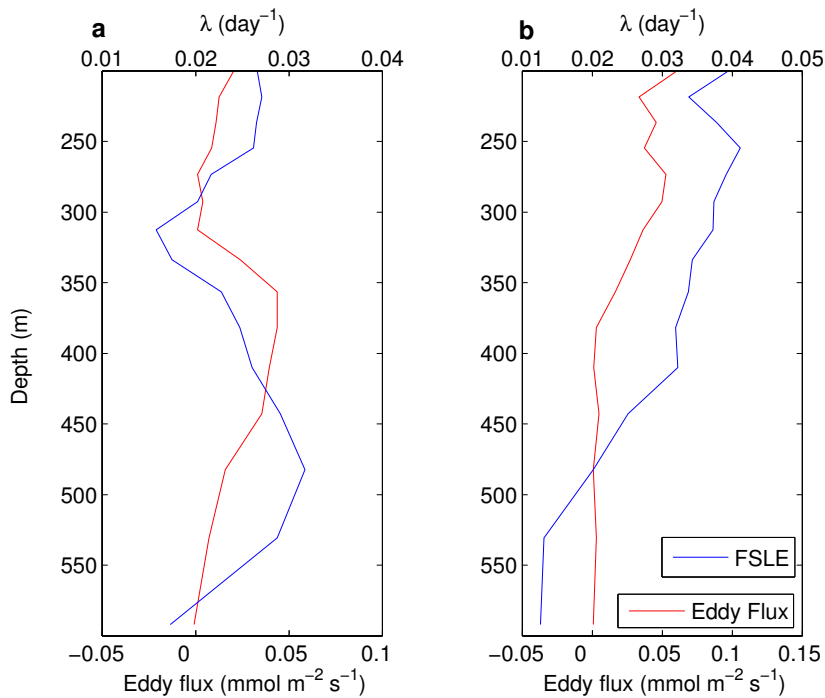


Figure 5.11: Vertical profiles of mean FSLE and normal eddy flux averaged along the northern and southern OMZ boundaries from the coast until 88° W for each depth. Blue lines are for FSLE values and red lines for eddy fluxes. a) Northern boundary. b) Southern boundary.

5.3. RESULTS

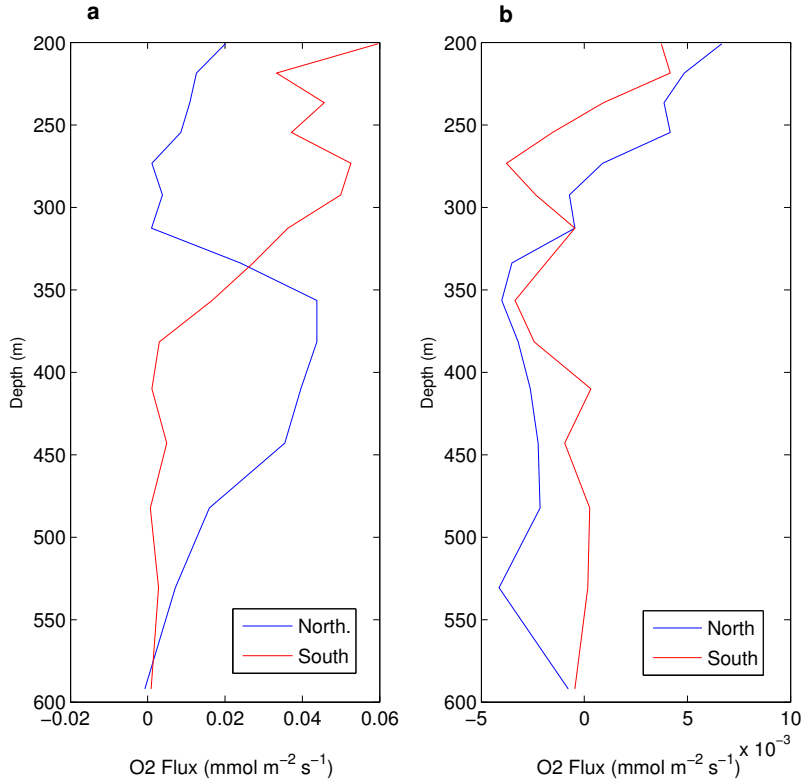


Figure 5.12: Vertical profiles of O₂ fluxes at the 20 μM OMZ mean boundaries between 200 and 600 m depth. The fluxes have been averaged along the horizontal extension of the boundary (from coast to 88°W) for each depth, and during year 21. A) Eddy flux profile (these are the red curves in Fig. 5.11). B) Mean flux profile (note the much smaller values as compared with the eddy fluxes.)

CHAPTER 5. STIRRING IN THE PERU OMZ

Boundary	Eddy flux ($\mu\text{mol s}^{-1}$)	Mean flux ($\mu\text{mol s}^{-1}$)
Northern	6.1526×10^6	-2.0080×10^5
Southern	1.0038×10^7	-3.5625×10^5

Table 5.1: Eddy and mean O_2 flow rates across the $20 \mu\text{M}$ mean boundaries from 200 to 600 m depth and from coast to 88°W .

The mean flux is positive above about 230 m, being negative or negligible below. Globally integrated between 200-600 m depth and along the northern $20 \mu\text{M}$ boundary from coast until 88°W , the eddy turbulent flow rate towards the OMZ interior is of $6.15 \times 10^6 \mu\text{mol s}^{-1}$ whereas the mean flow rate is $2 \times 10^5 \mu\text{mol s}^{-1}$ and directed outwards. At the southern $20 \mu\text{M}$ mean boundary, eddy fluxes are also positive (red line in Fig.5.11b along the range of depths considered, being fairly constant from 200 to 300 m, and nearly vanishing between 400 to 600 m depth. Integrated between 200-600 m and from coast to 88°W , the eddy turbulent flow rate towards the OMZ interior is of $1 \times 10^7 \mu\text{mol s}^{-1}$ whereas the mean flow rate is $3.56 \times 10^5 \mu\text{mol s}^{-1}$ and directed outwards. At both OMZ boundaries, eddy flows tend to bring O_2 into the OMZ at a much higher rate than the mean flow removes O_2 from the OMZ. At the southern boundary computed flows are higher than at the northern boundary probably due to the longer horizontal extension of the southern boundary. In both boundaries eddy fluxes are more than one order of magnitude larger than mean fluxes which shows the importance of mesoscale variability in the OMZ.

5.3.5 Cross-wavelet spectra

As an alternative methodology to quantify correlations between O_2 concentrations and the stirring measure provided by FSLE we conducted a cross-wavelet analysis between the O_2 concentration and backward FSLE times series from our simulation dataset at three particular locations in order to identify the dominant timescales of co-variability. The locations were: BNDNORTH, located on the northern OMZ boundary ($84^\circ\text{W}, 3^\circ\text{S}$) and 75 m depth; CORE, located in the OMZ core ($84^\circ\text{W}, 3^\circ\text{S}$) at 410 m depth; and BNDSOUTH, in the southern boundary ($84^\circ\text{W}, 16^\circ\text{S}$) at 410 m depth.

The climatological wavelet spectra consist in a wavelet decomposition of the intraseasonal anomaly time series followed by a calculation of the climatology of the wavelet power coefficient at each frequency. Wavelet spectra of O_2 and backward FSLE signals were computed following [161] at the three geographical locations. The time span of the signal is 4 years, from 1st July of simulation year 18 to

5.4. CONCLUSIONS

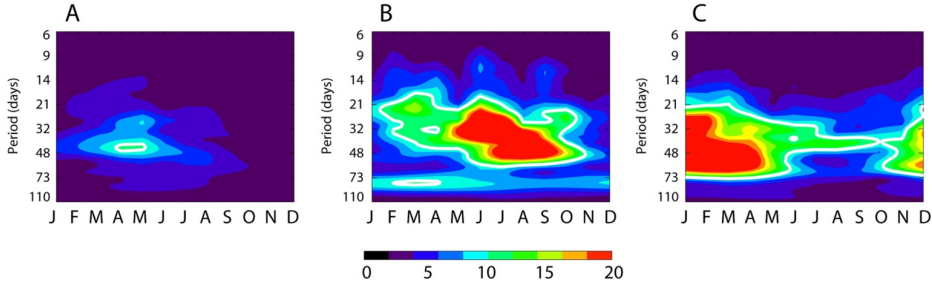


Figure 5.13: Climatological normalized cross-wavelet spectrum of O_2 concentration and FSLE time series at (A) CORE, (B) BNDSOUTH and (C) BNDNORTH. The horizontal axis indicates the calendar month. Units of the colorbar are $0.8 \times 10^{-4} M \text{ day}^{-1}$. The white thick contour in all panels indicates the 95% confidence level.

30 June of simulation year 22. Intraseasonal anomalies were estimated as the departures from the monthly mean. Wavelet power was normalized following Eq. 14 of [161] in order to compare the magnitude of the wavelet power at different frequencies. The mother wavelet used was the Morlet wavelet [161].

The climatology of the resulting cross-wavelet power is shown in Fig. 5.13. The plots indicate where the energy is dominant, i.e. where is a significant covariance between O_2 and FSLE, as a function of calendar month. Large energy is found in the intraseasonal frequency band with significant peak energy around 45 days. The marked seasonality of the intraseasonal activity indicates a link with the seasonal modulation of the baroclinic instability of the coastal currents (i.e. the Peru undercurrent) during Austral summer and in the South during Austral winter.

5.4

Conclusions

To conclude, in this chapter we have addressed the role of mesoscale structures that populate the OMZ in the ETSP, which are originated from the coastal upwelling areas of Peru and are advected offshore by a combination of mean currents and self-propagation. We identify the relevant parts of these mesoscale eddies and fronts as LCSs that act as barriers to transport controlling fluid interchange in and out the OMZ. Comparison of the FSLE approach with an exit time characterization supports this view. We find that mesoscale dynamics plays a dual role,

CHAPTER 5. STIRRING IN THE PERU OMZ

which can be respectively associated with the average behaviour and with the turbulent fluctuations. The northern and southern boundaries of the OMZ core are well determined by the averaged mesoscale dynamics, in particular for depths between 300 and 600 meters, where a good correlation between average FSLE and O_2 gradients was found. At other depths the relation between FSLE and O_2 may not hold indicating stronger O_2 forcing by biogeochemical processes. Episodic events of OMZ ventilation are produced by turbulent eddy stirring where waters with high O_2 content are entrained into the OMZ by the action of mesoscale eddies. On the whole, between 200 and 600 m depth, eddy fluxes were found to bring O_2 inside the OMZ at both the northern and southern boundaries, while O_2 mean fluxes were much smaller and in the opposite direction. The biogeochemical processes occurring in the interior of the OMZ would provide the dominant oxygen consumption sink to close the O_2 budget.

Lagrangian structures in a coastal filament

The structure and dynamics of an upwelling filament in the Iberian upwelling system is analyzed. Three-dimensional Lagrangian coherent structures are computed from finite-size Lyapunov exponent fields.

6.1

Introduction

In the Western Iberia oceanic margin, mesoscale processes, rather than the large-scale variability, are the dominant factors controlling the ecosystem of the region. The regional oceanography reveals, first and foremost, a series of mesoscale structures such as jets, meanders, eddies and upwelling filaments, superimposed on the large scale seasonal patterns. At the ecosystem community level, dynamics with spatial scales of 10-100 km are determinant for larval retention or dispersal from general areas and more generally, for the marine plankton communities [162].

In the late Spring/early Summer, predominantly northerly winds start to blow off West Iberia, driving an offshore Ekman transport forcing the upwelling of colder, nutrient-rich subsurface waters along the coast. The Ekman transport is as deep as 30 m and the upwelled waters come from 200 m in a 10-20 km wide strip at a velocity of $\sim 10 \text{ m d}^{-1}$ [163]. One month after the initiation of the upwelling favorable winds, large filaments start to develop, associated with strong offshore currents ($\sim 0.5 \text{ cm s}^{-1}$) and can extend more than 200 km offshore

CHAPTER 6. STRUCTURE OF A COASTAL FILAMENT

[162]. The significant offshore mass transport along the major axis of a filament is larger than that possible by purely wind-driven Ekman dynamics [162] and the measured carbon export is 2.5 to 4.5 times the carbon export due to Ekman transport [164], so these features provide an important mechanism for exchange between coastal and offshore waters, especially of organic materials [165].

Several mechanisms have been proposed for the formation of upwelling filaments: instabilities of along-shore upwelling jets [166]; wind-stress curl [167]; meandering of the equatorward jet [168] and topographic forcing [169]. While most of the filaments in Western Iberia occur associated with important capes [162], there are some exceptions where the mechanism seems to be dynamic instability or mesoscale eddies [168].

Observations *in situ* have elucidated some aspects of the physical and biological oceanography of upwelling filaments. The offshore flow was found to be limited to a thin surface layer with substantial onshore flow occurring below 50 m in the center of the filament, while the strongest and deepest offshore flow was found at the boundaries [170, 171]. Within the filament, water has been found to be relatively homogeneous but well isolated from the surroundings [171]. Weak mixing in the core but enhanced at the boundaries has been reported [170]. On one occasion, opposite rotating eddies were found at the base and tip of the filament, promoting its generation and fast offshore development. Mesoscale eddies at the ocean side of the upwelling front, resulting from the interaction of the poleward flow, topography and upwelling jet were indicated as contributing to the filament development [172]. A low salinity plume has been mentioned as a possible input of buoyancy to the filamentary structure, promoting its offshore elongation [171, 172]. Unlike the pulsating offshore Ekman transport, filaments provide a permanent offshore displacement of water masses and are responsible for enhanced transport of chlorophyll [171], while surface waters within filaments have been found to be depleted of nitrogen [165].

In this chapter we use Lagrangian tools to study the 3d structure of an upwelling filament in a regional ocean simulation of the Western Iberian shelf and adjacent ocean using realistic forcing. We compute 3d fields of FSLE during the late summer/early Autumn of 2007 and extract the 3d boundaries of the filament as ridges of the 3d FSLE fields. Synthetic tracers are released and tracked numerically in order to characterize the dynamics of the water masses inside the filament.

Data

6.2.1 Simulation of the Western Iberian shelf

The oceanic simulation were done using the Regional Ocean Modeling System (ROMS, <http://myroms.org>, [115]). ROMS is a free-surface terrain-following model which solves the primitive equations using the Boussinesq and hydrostatic approximations. This state-of-the-art model is highly configurable for realistic applications and has been applied to a wide variety of space and time scales across the world [116].

The model domain covers the Portuguese and Galician region, extending well beyond the shelf break (13.25°W to 7.5°W and 356°N to 45°N) with horizontal resolution of 2 km in South-North direction and 1 km in the West-East direction. The vertical discretization used 30 s-layers, stretched to result in increased resolution near the surface and bottom. The bathymetry was interpolated from ETOPO and smoothed to satisfy topographic stiffness-ratio of 0.2 [173]. The minimum depth used was 3 m. The configuration used a fourth-order horizontal advection scheme for tracers, a third-order upwind advection scheme for momentum, and the turbulence closure scheme for vertical mixing by [174].

The simulations were initiated from November 2003, using realistic initial and boundary conditions from the global model HYCOM, which provides daily data from this date. HYCOM [175] has horizontal resolution of $1/12^{\circ}$ and the data is available at 33 vertical layers. This model assimilates observations from several sources including satellite altimetry, satellite and in situ temperatures, and vertical temperature and salinity profiles from XBTs and ARGO buoys. The offline nesting procedure employed used a nudging region of 40 km along the model boundaries. In this layer, the 3d model variables (temperature, salinity and currents) were nudged towards the HYCOM data with a time scale of 8h. The nudging was set maximum at the boundaries, decaying sinusoidally to zero inside the nudging layer. At the boundaries, radiation conditions [176] were used for the baroclinic variables. Sea surface height and barotropic currents from the parent models were imposed at the boundaries as [177] and [178] boundary conditions.

ROMS has been applied in many coastal modeling works in the region. For example in studies of dispersion and recruitment of larvae [179], river plumes [180] and pollution transport [181]. These studies have been typically based on climatological open boundary conditions. In the current work, where high realism was desired, offline nesting has been adopted. It has been shown that using an assimilated parent model improves the ROMS skill [182], even when parent and

CHAPTER 6. STRUCTURE OF A COASTAL FILAMENT

child are forced with different atmospheric data [183]. Other works have used the same nesting procedure and HYCOM as parent model, for example [184–187].

At the surface heat and freshwater fluxes from ERA-INTERIM were used [188] with a resolution of 0.75° . As wind forcing, it was used data from the Cross-Calibrated Multi-Platform (CCMP) Ocean Surface Wind Vector Analyses [189]. CCMP uses a variational analysis method to combine data from satellite sources, producing 0.25° gridded winds every 6 h. This product provides high quality data from 1987 to 2011 with a spatial and temporal resolution that makes it one the best global wind products available.

The main rivers from Portugal and Galicia were incorporated in the modeling configuration. River discharges were obtained from the national institutes and estimated using the procedures described by [190]. The main rivers, like Douro and Minho, come from measurements in the studied period, others are used as monthly climatologies, due to absence of data. River temperatures were set as equal to the climatological surface air temperature for the region from [191].

6.2.2 3d FSLE fields

The 3d FSLE fields were computed following the method outlined in the previous chapters, using twice the horizontal resolution of the ROMS grid. The calculation area of the FSLE fields is shown in Figure 6.1. The vertical resolution is variable with 30 levels between 5 and 200 m depth, clustered near the surface. The final distance threshold δ_f was set at 100 km and the particles were integrated for 90 days with the 3d velocity field. The period of calculation of FSLE fields went from late August to early October where filament activity is stronger [168], with fields computed daily. Both forward and backward fields were computed.

6.3

Results

6.3.1 FSLE fields and mesoscale structures

In this section we describe the structure and distribution of the FSLE fields. The dynamics in the FSLE calculation region is dominated by a complex pattern of mesoscale and submesoscale features. At the 24th of September 2007, the dominant structure is a large anticyclonic eddy located at 42°N and $10^\circ30'\text{W}$ with a diameter of ~ 100 km (Figure 6.3, top left panel). Westward of this anticyclonic

6.3. RESULTS

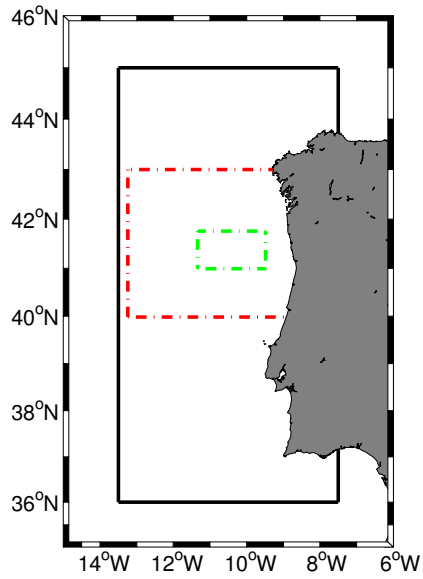


Figure 6.1: Western Iberia domain. Black full line: ROMS simulation domain; Red dash-dot line: FSLE fields domain; Green dash-dot line: Ridge extraction domain.

CHAPTER 6. STRUCTURE OF A COASTAL FILAMENT

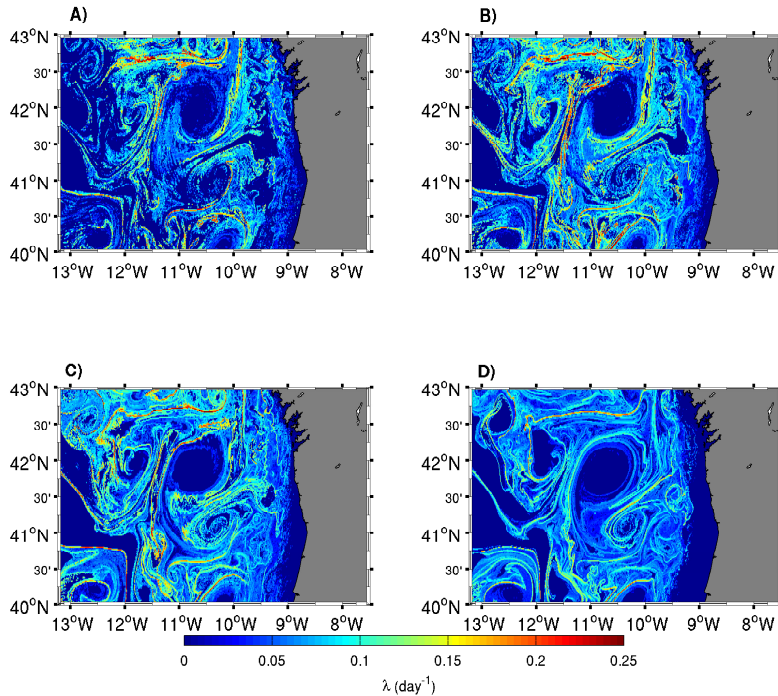


Figure 6.2: Backward FSLE field at 24th of September 2007. A) 9.8 m depth; B) 17.1 m depth; C) 31.8 m depth; D) 96.8 m depth.

eddy we find a cyclonic eddy forming a dipole structure. Between these eddies, a large straining region can be found, signaled by the concentration of high FSLE lines. The dipole is pulling fluid from the south along its axis that is aligned in the meridional direction. South of this second cyclonic eddy we find an additional anticyclonic eddy forming a second dipole with the cyclonic eddy of the first dipole, a not unusual situation, previously observed [192]. This second dipole has an axis directed along the zonal direction and is pulling fluid towards the shelf. The fluid pulled zonally by this second dipole is slightly colder (see Figure 6.3, top left panel) than the waters in the dipole's eddy cores and thus shows as a colder water tongue along the dipole axis, that is deflect southward when it encounters the axis of the first dipole, perpendicular to it.

High FSLE lines populate the region, but are found mainly on the boundaries of the dominant mesoscale structures. The field at the surface layers is markedly

6.3. RESULTS

noisy, while the deeper levels show less small scale noise. The coastal strip (around $9^{\circ}30'$ W) is characterized by patches of low FSLE and zones where the FSLE is zero. These last regions are characterized by weak dispersion of fluid elements and the one centered around $41^{\circ}30'$ N and $9^{\circ}30'$ W at 9.8 m depth (Figure 6.2, top left panel) can be seen to have a thin offshore extension that forms an pathway to the transfer of coastal waters to the offshore. The fact that these regions have zero FSLE means that the fluid particles released for those regions will evolve, backward in time, along close trajectories with very small divergence between particle pairs. In other words, nearby particles passing through these regions come from nearby initial positions. Observing the lower levels in Figure 6.2, we can see that the zero FSLE patch is present at 17 m depth (Figure 6.2, top right panel) and at 32 m depth (Figure 6.2, bottom left panel), with smaller extension as we move deeper. This is a signal of an upwelling center, i. e., a region through which fluid is being raised to the surface (and moved to the offshore, as is shown in section 6.3.2). Note that this does not imply that the upwelled fluid mass ultimately originates at the same region, instead, it is more likely that fluid converges to these regions at deeper levels and then is raised to the surface along this upwelling channel.

There are other areas where the FSLE is essentially zero. The large anticyclonic eddy has zero FSLE in its core along all depths shown in Figure 6.2. Note however that the eddy is not completely enclosed by high FSLE lines and at the northeast and southwest sectors the FSLE exhibits non zero values. At the northeast sector we find an "avenue" of low FSLE surrounded by two lines of high FSLE. The one to the left (further offshore), descending from the North, curves to the right forming the North barrier to the eddy and the other descending also from the North, forms an eastern eddy boundary. The boundaries also signal the pathways through which fluid enters the anticyclonic eddy. The eastern boundary closer to the shore, brings fluid from the coastal region that turns right into the eddy along its southern boundary, while between both high FSLE lines, there is a pathway to fluid entering the eddy from the north.

Other regions void of FSLE can be seen further offshore, indicating areas through which the fluid is passing without significant divergence. These areas maintain their configuration from the surface at least up to 100 m depth.

6.3.2 Formation and evolution of a coastal filament

In this section we analyse the evolution of the filament since its formation. The filament studied in this chapter was formed around the 2nd half of September 2007 and was perfectly noticeable at the 20th of September (Figure 6.3, top right

CHAPTER 6. STRUCTURE OF A COASTAL FILAMENT

panel) as a cold water tongue connecting the coastal cold upwelled water above $40^{\circ}30'$ N with a cyclonic recirculation cell centered around 41° N and $10^{\circ}30'$ W. The filament evolved from a cold water pool entrained in the warm water region just offshore of the upwelling area. This pool is visible at the 09th of September centered at $41^{\circ}15'$ N and $9^{\circ}30'$ W (Figure 6.3, top left panel). Adjacent to this cold water intrusion and centered slightly to the southwest we find the cyclonic recirculation, still in an initial stage. The formation of the filament is a result of the interaction between the anticyclonic eddy and the coast topography. Indeed, several observational and numerical studies of the interaction between anticyclonic eddies and shelf topography have showed that this interaction results in the formation of secondary cyclonic eddies and cross-shore water exchange [193–195]. In particular, [195] showed, through numerical simulations, the formation of an cyclonic secondary circulation to a anticyclonic eddy, fed by shelf water with high potential vorticity that ultimately grows until it forms a dipole with the anticyclonic eddy.

The dynamics of the filament is determined by this cyclonic eddy but also by the larger anticyclonic eddy located northward. At the 20th of September the cyclonic eddy has grown and the water temperature is lower than the surrounding waters due to the feeding of upwelled cold water by the filament. Four days later (Figure 6.3, bottom left panel) the filament has an almost straight axis and is still exporting colder water offshore but in to the cyclonic eddy. Remarkably, there is a parallel offshore motion of warmer water, north of the cold water filament, that is recirculating inside the large anticyclonic eddy. The filament is separated from the warm water adjacent region by a line of high FSLE. While the action of the cyclonic eddy is evident, the effect of the anticyclonic eddy is not so. It could be also pulling cold water through the filament, but it seems to be isolated from the cold upwelled waters by a series of barriers signaled by the high FSLE lines that are visible around its periphery in the contact zone with the upwelling front (Figure 6.2, top panels).

The filament dynamics continues and a few day later, at the 06th of October, we find that a coastal dipole has been formed by the cyclonic and anticyclonic circulations that now have approximately the same size. Meanwhile the temperature differences have diminished, especially due to the cooling of the waters in the anticyclonic eddy. This cooling is due mainly to an upwelling event occurring during from the 25th to the 30th of September that supplied the filament with cold water. The filament continues to evolve further, but its signature is significantly reduced due to this cooling event.

6.3. RESULTS

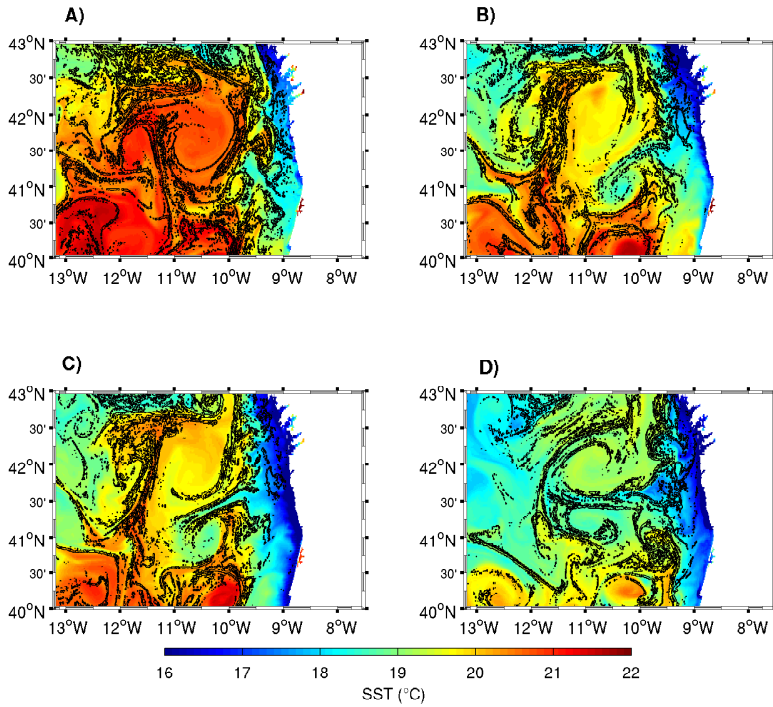


Figure 6.3: Filament evolution. A) Sea surface temperature and backward FSLE contours (0.1 day^{-1}) at 09/09/2007; B) 20/09/2007; C) 24/09/2007; D) 06/10/2007.

CHAPTER 6. STRUCTURE OF A COASTAL FILAMENT

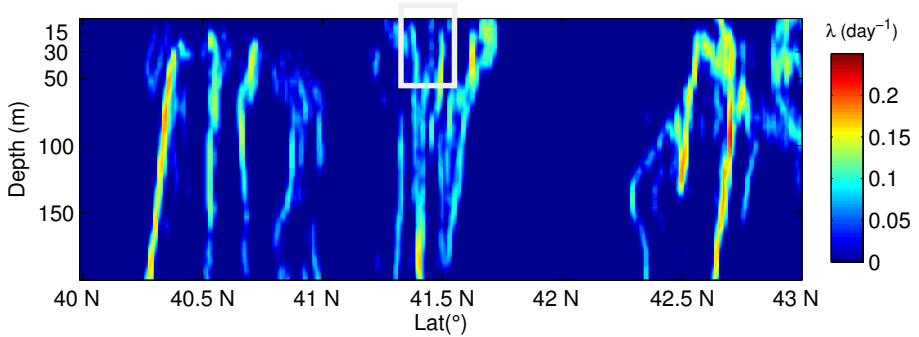


Figure 6.4: Vertical section of backward FSLE taken at $10^{\circ}15'$ W at the 24/09/2007. The FSLE field was smoothed and filtered to improve clarity. The filament area is highlighted in the white rectangle.

6.3.3 Lagrangian structure and transport in the filament

In this section we look at the transport structure inside the filament. The filament appears as a thin elongated region of zero backward FSLE, visible in Figure 6.2 at 9.8 m and 17.1 m depth (top panels). The signature is absent on deeper levels, indicating the shallow nature of this corridor transporting shelf water to the offshore. A vertical section through the backward FSLE field for the 24th of September 2007 (Figure 6.4) shows its vertical extent to be at most 50 m. Adjacent to the north boundary of the filament, there is a shallow strip that constitutes the corridor through which the northern waters recirculating around the anticyclonic eddy enter it at the south border. The boundaries of the anticyclonic eddy intersect the figure plane northward of the filament and it is visible that the eddy is slanted toward the north, principally at its northern boundary that is also the strongest. The cyclonic eddy is seen south of the filament and, contrary to the anticyclonic eddy, its center, at 41° N shows small but nonzero FSLE.

A profile of the filament was taken for the same date (see Figure 6.5). FSLE, temperature and salinity fields were interpolated linearly along the filament from the surface to 200 m depth. The variations in FSLE, temperature and salinity along the filament are shown in Figure 6.6.

The filament appears as a shallow feature in the FSLE field with a central portion not deeper than 25 m. At the root, the depth increases beyond 50 m but the width diminishes. This vertical variation is also visible in the FSLE maps of Figure 6.2, where we can observe the progressive closing of the zero FSLE area at

6.3. RESULTS

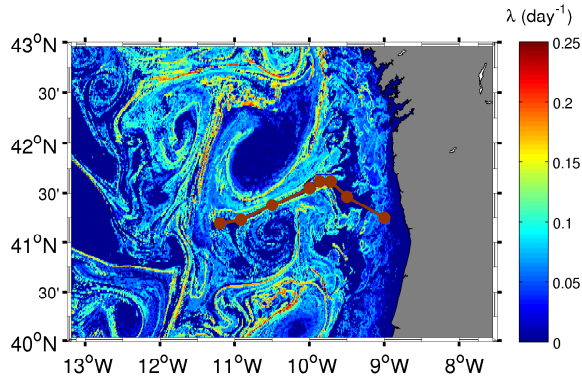


Figure 6.5: Location of the profile path taken along the filament at the 26/09/2007. FSLE map at 14.7 m depth. Brown circles are the nodes of the profile.

the root of the filament as depth increases. To the offshore, the filament becomes shallower until it is closed at ~ 200 km. We can observe that before reaching the end of the filament, the zero FSLE region has curved southward to adhere to the cyclonic eddy that is supplied by the water flowing through the filament. Temperature variation in the profile indicate that the filament is supplied with upwelled water that increases its temperature as it flows through the filament. There is a sharp temperature gradient located 30-50 m below the surface. Salinity in the profile shows a salient pool of fresh water located at the root of the filament up to a depth of 50 m. The salinity gradually increases along the profile until reaching a maximum at 140 km offshore from the filament root. Between 140 and 180 km there is a clear uplifting of isotherms caused by the presence of the cyclonic circulation to the south, that is adjacent to the profile at this distance range. This uplifting may also be noticed in the FSLE distribution (panel A)).

Offshore advection by the filament was further investigated by computing particle trajectories released at the filament root at various depths. Particles were released at $9^{\circ}30'$ W at the 26th of September 2007 at 7, 12, 24, 29 and 34 m depth. At each depth, seven particles were released along a line between $41^{\circ}30'$ N and $41^{\circ}35'$ N, inside the filament root. Particle trajectories were integrated until the year's end. Only the particles that traveled offshore of $10^{\circ}30'$ W were considered in the following analysis.

CHAPTER 6. STRUCTURE OF A COASTAL FILAMENT

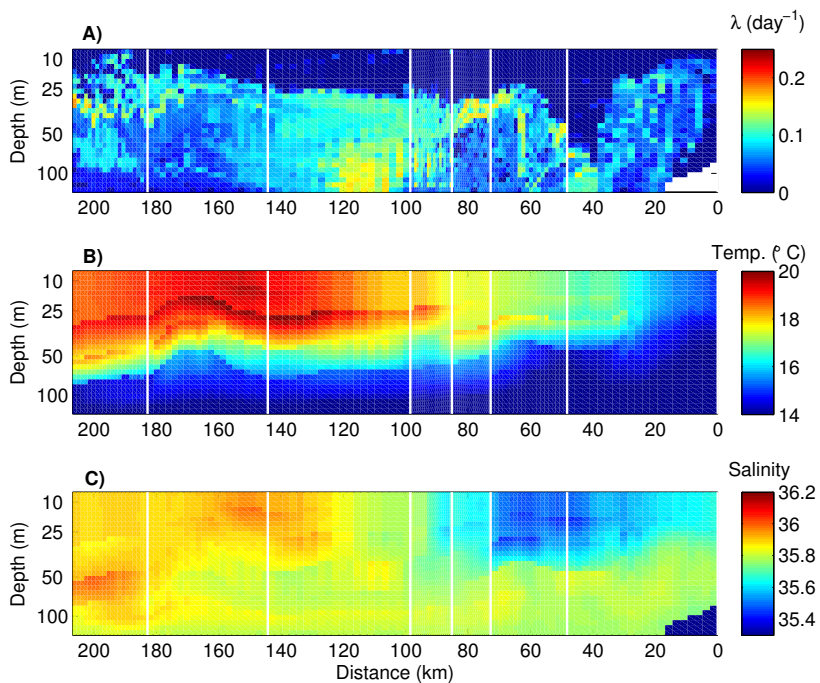


Figure 6.6: Profiles along filament at 26/09/2007. A) Backward FSLE; B) Temperature; C) Salinity. White vertical lines represent locations of profile nodes. Fields were interpolated linearly in between nodes. Distance along profile increases towards the offshore.

6.3. RESULTS

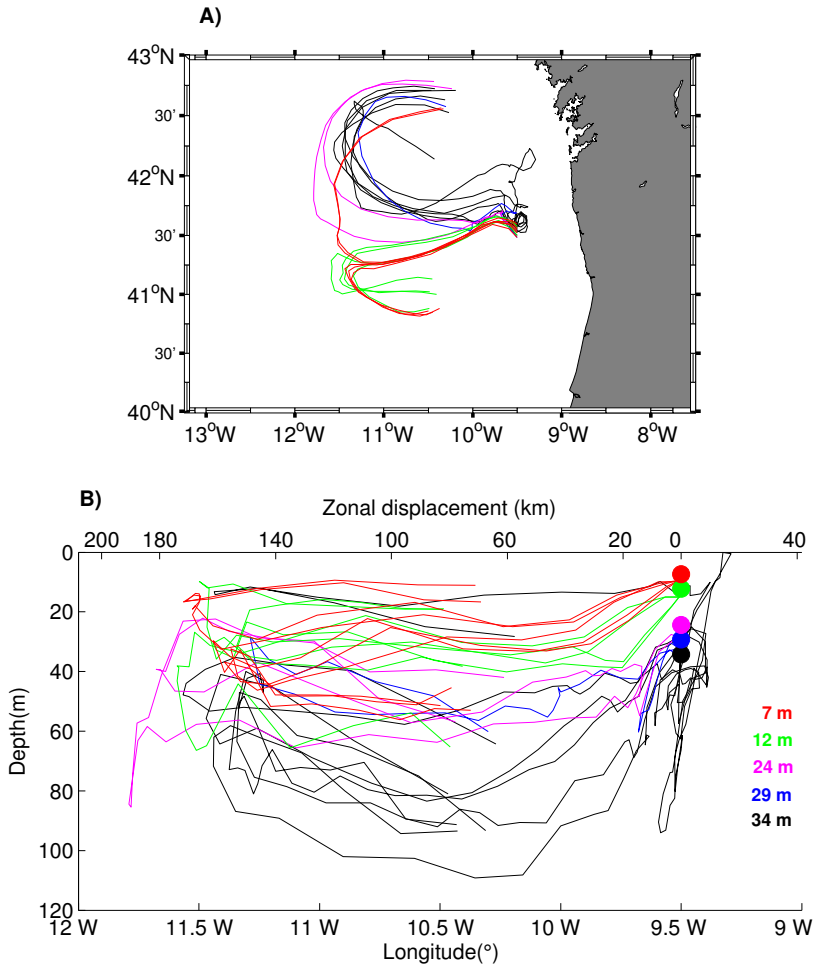


Figure 6.7: Trajectories of particles released at the root of the filament. A) Horizontal trajectories; B) Vertical and longitudinal displacement along the particles trajectories. Particles were released at 9°30' W at 26/09/2007 at 7, 12, 24, 29 and 34 m depth and were integrated until year's end. Only the particles that traveled offshore of 10°30' W are shown, until they crossed the same longitude in the opposite direction.

CHAPTER 6. STRUCTURE OF A COASTAL FILAMENT

The horizontal trajectories (Figure 6.7 A)) clearly separate the particle sets in two groups depending on the depth at which they were released: shallower releases (7 and 12 m) take the particles through the filament into the cyclonic circulation to the south while deeper releases take the particles towards the anticyclonic eddy north of the filament. Nevertheless, some particles released at 7 m follow the filament but end up circulating around the anticyclonic eddy. A particle released from 34 m depth travels northward before entering the anticyclone. Observing the horizontal trajectories of the 7 and 12 m group of particles that flow through the filament, it is clear that the filament is not completely vertical and possesses an northward inclination in the vertical. Furthermore, from the horizontal trajectories it is seen that the only the shallower waters from the filament root are fed to the cyclonic circulation, while the deeper waters seem to enter the anticyclone. This can be also observed in Figure 6.2 where at 17 m depth the filament already is reduced in its length and does not connect to the cyclone. Another feature of this set of trajectories is that many of them eventually return to the inshore region through recirculation inside the eddies.

The maximum zonal displacement is ~ 200 km (Figure 6.7 B)), similar to the filament extension. The shallower particles, that go through the filament, experience a subduction in the initial phase and reach the deepest ~ 60 km from the release location. They then begin to rise briefly until the 100 km mark. After this the "red" particles enter the cyclonic circulation and sink, while the "green" particles remain approximately at the same depth. The two red particles that enter the anticyclonic circulation eventually rise when their trajectories curve anticyclonically to the north. The different behavior of the green and red particles is most likely caused by the fact that red particles, circulating further from the cyclone's center will tend to follow deeper isotherms than the green particles. The deeper particles curve anticyclonically to the north. Those released at 24 and 29 m, sink sharply in the first 20 km but then follow a relatively horizontal path until entering the anticyclonic circulation. The deepest set of particles show a much greater depth variation along its path and some particles sink abruptly immediately after the release and then are upwelled and move a short distance towards the shore before being advected offshore.

The temperature-salinity (T-S) diagram of the particles is shown in Figure 6.8. The T-S data for the initial locations is marked by crosses. The salinity at the release locations varies little across the release depths, but temperature can vary as much as 1°C . The coldest water is found at 24 m depth and the warmer at 29 m depth, warmer than the more shallow release locations. This is caused by the location of the sharp temperature gradient at the bottom of the mixed layer in the filament root. The temperature profile (Figure 6.6 B)) shows that this gradient is located at the depths of the two deeper sets of particles and that the

6.3. RESULTS

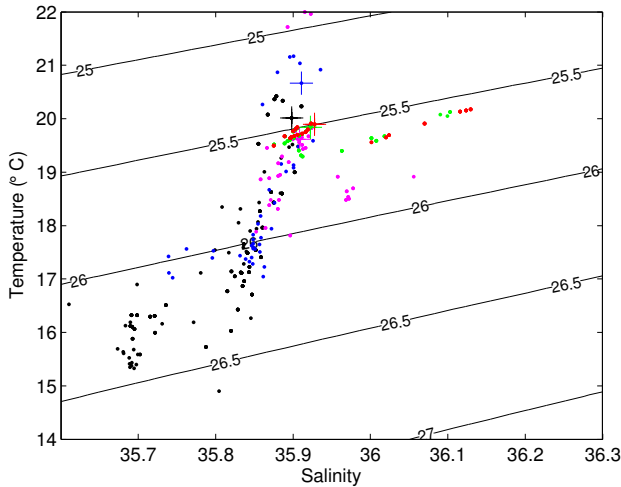


Figure 6.8: Temperature-Salinity (T-S) diagram of particles released at the root of the filament. Black lines in the diagram are constant density lines. Crosses indicate the T-S properties at the release location.

waters at these depths can be slightly warmer than surface waters (note that the second node from shore used to define the profile is located at $9^{\circ}30'$ W). The two shallower sets then evolve mainly in a path where they conserve density as the T-S diagram shows. The remaining sets show a contrasting evolution of their T-S relation, exhibiting relatively strong changes to their temperature. While there are differences between the three sets, there is a general tendency to cool when sinking (less pronounced in the "pink" particles and stronger for the "black" particles) and then to warm again when they enter the anticyclone. The final temperature is higher for the particles close to the anticyclone's core (blue and black) than for the pink particles that remain towards the periphery.

6.3.4 3d Lagrangian structure of the filament

The 3d Lagrangian structure of the filament was investigated by extracting regions of the 3d backward FSLE field. These ridges approximately coincide with attracting Lagrangian coherent structures (LCS) of the flow. To avoid unnecessary computational effort, the extraction process was limited to a subregion of the FSLE domain between $11^{\circ}20'$ W and $9^{\circ}30'$ W, 41° N and $41^{\circ}45'$ N and 7 and 70 m depth, see Figure 6.1. In order to extract the ridges by the method outlined

CHAPTER 6. STRUCTURE OF A COASTAL FILAMENT

in section 2.10.2, the FSLE field was smoothed [196, 197] and high-pass filtered to remove most of the small scale noise.

The relevant ridges for the 26th of September 2007, defining the Lagrangian dynamics at the filament area are those that make the boundary of the anticyclone, the boundary of the cyclone and the Lagrangian structure that separates the fluid exported offshore that enters the anticyclone from that that enters the cyclone through the filament (Figure 6.9). Levels of the 3d FSLE field are plotted together with the 3d ridges at 20 m depth (Figure 6.9 A) and at 45 m (Figure 6.9 B)). As was already discussed in previous chapters the ridges fall on the high FSLE lines but the ridge strength is only indirectly linked to the FSLE field.

Fluid elements flow along attracting ridges of the FSLE field, so the blue ridge is moving fluid offshore from the filament root. The green ridge, on the other hand is separating the fluid inside the anticyclone from the fluid that is outside but flows around the eddy. Note that, at least at the surface, this fluid is warmer than the filament fluid (Figure 6.3 C)) so there should be a barrier separating these two streams and preventing them from mixing. In the 20 m depth FSLE map of Figure 6.9 A) there is a line of high FSLE separating these regions, but the extraction process did not find an ridge there. It is possible that the ridge extraction threshold was set too high for the intensity of this ridge at this depth. On the other hand, at 45 m depth there is a ridge separating both streams.

The separating (SP) ridge shape is clearly depicted in Figure 6.10, where it can be seen that it is connected to the anticyclonic (AC) ridge by an horizontal “bridge” located slightly below 20 m depth. The surface section of the AC ridge ends at this same depth and there is an hiatus until a second portion of the AC ridge begins, the SP ridge has vertical continuity in the range of depths were the ridge extraction was done. The hiatus is probably an artifact of the ridge extraction process and results from a smaller intensity of the AC ridge in that depth range. The cyclonic (CC) ridge also has continuity in the vertical except at the root of the filament where there is an interruption between 30 m and 40 m depth. Additionally it is clear that the extension of the CC ridge in the filament root diminishes with depth, an effect of the contraction of the filament root pool observed in Figure 6.2.

The thermohaline structure of the filament is depicted in Figure 6.10 where vertical maps of temperature and salinity are shown perpendicular to the filament axis. There is a clear temperature difference between surface and subthermocline waters and, furthermore, between the cyclone where isotherms are raised and the anticyclone where these are depressed. The 3d ridges are located in the transition between both mesoscale structures. Contrary to what could be expected, the CC ridge is not adjacent to the cold filament – visible in Figure 6.10 A) as a lower

6.3. RESULTS

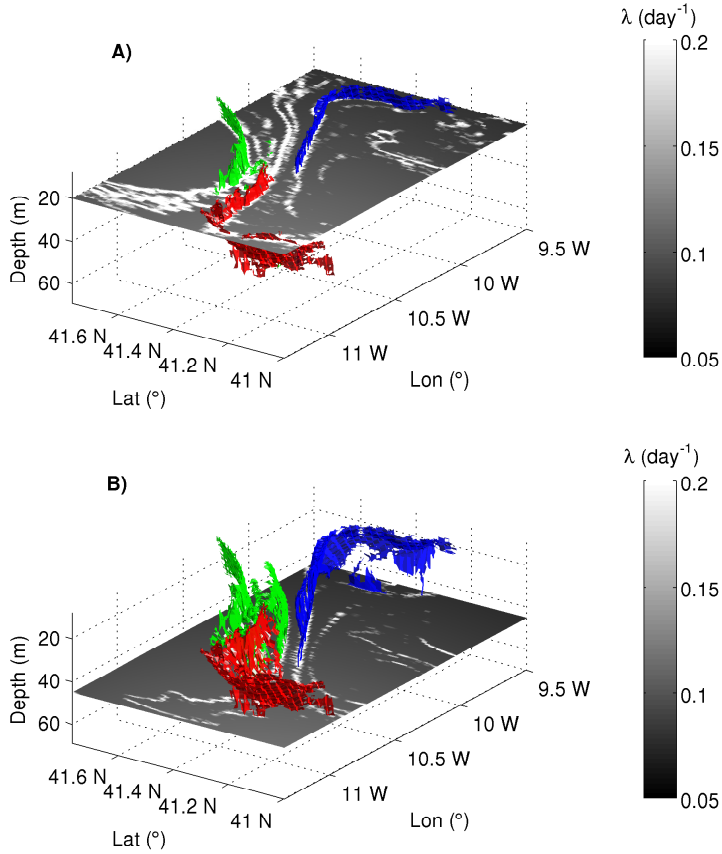


Figure 6.9: Ridges of the 3d FSLE field defining the filament. Ridges extracted the 26/09/2007. Green: boundary of the anticyclone; Blue: boundary of the cyclone; Red: Ridge separating the two dipoles mention earlier in section 6.3.1. A) Horizontal FSLE field at 20 m depth; B) Horizontal FSLE field at 45 m depth.

CHAPTER 6. STRUCTURE OF A COASTAL FILAMENT

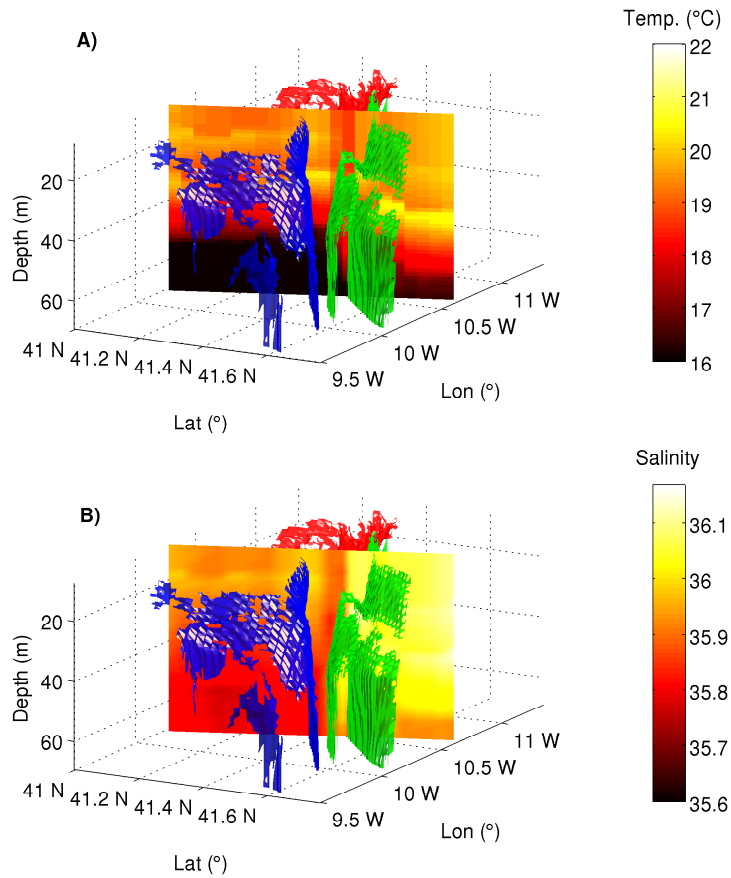


Figure 6.10: Ridges of the 3d FSLE field defining the filament. Ridges extracted the 26/09/2007. Green: boundary of the anticyclone; Blue: boundary of the cyclone; Red: Ridge separating the two dipoles mention earlier in section 6.3.1. A) Temperature. B) Salinity. Temperature and salinity are shown in a vertical plane normal to the filament axis that passes through $10^{\circ}27'$ W.

6.4. CONCLUSIONS

temperature strip apparently coincident with the SP ridge location – but slightly deviated. The reason for this is visible in Figure 6.3 B) and C), where a tongue of warm water can be observed between the cyclone and the colder coastal waters. This tongue is pulled offshore by the cyclonic circulation and forms a boundary between the cyclone and the filament. Since both masses are flowing offshore, their divergence is minimal and the CC ridge instead separates the cyclonic circulation from the tongue of warm water that it is pulling offshore. The salinity structure (Figure 6.10 B)) shows the distinct origins of the anticyclone and cyclone. The first has warm, salty water while the second has colder and fresher waters supplied by the filament from the nearshore. The salinity front is located at the SP ridge location.

6.4

Conclusions

Coastal upwelling filaments are ubiquitous features of coastal circulation and they play a very important role in the cross-shelf exchange of water masses. In upwelling regions this role assumes even greater importance due to the biological relevance of such regions. The Iberian peninsula upwelling region is populated by these structures, that achieve maximum activity in late summer. Using outputs of a numerical simulation of the ocean circulation in the western Iberian coast, we studied the 3d dynamics of a coastal filament using Lagrangian methods.

The filament was generated in September 2007 by the interaction between an anticyclone and the shelf circulation. This interaction generated a secondary cyclone that was fed by upwelled water from the shelf by a filament structure with ~ 200 km of extension. The 3d FSLE fields computed in the region show intense mesoscale activity in the form of mesoscale eddies and submesoscale fronts that organize transport. The high FSLE lines present in the region allowed us to identify the major barriers and pathways of fluid transport. The filament itself appears as a thin region of zero FSLE values, indicating that the fluid moves unidirectionally in its interior, towards the offshore. The 3d distribution of FSLE also showed that the water that forms the filament is upwelled from below.

Particle trajectories released at the filament root at several depths showed that the filament is limited to the first 20 m of depth, where its waters end up feeding the cyclonic circulation. Below, the waters flowing offshore feed the anticyclone, but both water masses end up returning to the shelf by the circulation of the two eddies. Waters in the filament maintain constant density, while those below the filament cool during their advection offshore. To elucidate further the 3d

CHAPTER 6. STRUCTURE OF A COASTAL FILAMENT

structure and transport of the filament, 3d ridges of the backward FSLE fields were extracted. These ridges are proxies to 3d Lagrangian structures that induce coherent fluid motion. The filament is limited by the 3d Lagrangian boundaries of both the anticyclone and the cyclone and by an additional barrier that separates waters that flow around the anticyclone from those that feed the cyclone with cold, upwelled waters. The Lagrangian structures that form the boundaries of the eddies adjacent to the filament, provide the necessary 3d barriers to mixing that prevent the filament water from losing its distinct characteristics during its offshore advection.

Conclusions

General Conclusions

Dynamical systems theory has provided powerful tools to the Lagrangian study of turbulence and fluid motion, especially through the concepts of chaotic advection, invariant manifolds and Lyapunov exponents. These concepts and tools have been applied in the literature to the study of various aspects of oceanic transport by coherent structures, but they have been mostly limited to the surface, in a two-dimensional fashion. This leaves the 3rd dimension and vertical processes out of the scope of these novel techniques. The importance of the vertical motions in the ocean and the fact that they are deeply associated with mesoscale phenomena that were previously successfully addressed motivated this work where we extended the application of Lagrangian techniques, especially the concept of coherent structures to three dimensional (3d) oceanic motions.

Measures of material stretching and dispersion in fluid flows such as the finite-size Lyapunov exponent (FSLE) have been used to identify Lagrangian coherent structures in flows. The rationale behind this is that maxima of these measures identify regions of the flow where the fluid behaves coherently, i. e., it behaves in such a fashion that lasts long enough to be observed.

In two dimensions, the maxima of the FSLE are readily identifiable as these occur along lines in the domain of the flow, but in 3d the maxima are hidden in the volume data and they can only be fully visualized by extraction. The concept of ridge is very useful in this respect because it provides rigorous mathematical conditions to identify points lying on ridges of scalar fields. We have used this concept to extract the ridges of the 3d FSLE fields and thus locate the 3d Lagrangian structures responsible for coherent motions of fluid particles.

The first step was to identify 3d Lagrangian structures in a canonical turbulent flow, widely studied, and whose coherent structures have been thoroughly inves-

CHAPTER 7. CONCLUSIONS

tigated in the Eulerian perspective. The 3d structures educed in the turbulent channel flow studied in chapter 3 exhibited analogies with their Eulerian counter parts and were mostly associated with 3d vortical motions. However, unlike the Eulerian coherent structures, these Lagrangian coherent structures provided a clear separation between the near-wall turbulent region of the flow and the more quiescent outer region. The 3d Lagrangian structures moved with the flow and thus had a clearly material nature and, furthermore, had a very complex shape, evolving in all three space dimensions.

The 3d Lagrangian structures in an oceanic setting, the Benguela upwelling region, were then studied (chapter 4) and they were found to be almost vertical, with a "curtain" shape. This is the result of the almost 2-dimensionality of oceanic motions, that dominate stretching of material lines and stirring of tracers in the ocean. Mesoscale eddies have 3d barriers around them that prevent the mixing of waters between the eddy interior and the exterior. These 3d barriers are Lagrangian in nature and control the transport inside and outside of the eddy. Both attracting and repelling 3d Lagrangian structures were found to define an mesoscale eddy and the process of filamentation is related to the dynamics of these barriers. A decreased in intensity of these 3d Lagrangian structures with depth was found to occur.

The effect of stirring of oceanic tracers by the Lagrangian structures of the flow was studied for the Oxygen Minimum Zone that develops off the Peruvian coast (chapter 5). Large average gradients of dissolved O_2 were found to be coincident with high stirring areas, identified as regions with high average values of FSLE. This relationship occurs more strongly at mid-depth ranges in the core of the OMZ. The turbulent fluxes of O_2 across the boundaries of the OMZ are enhanced by the stirring caused by Lagrangian coherent structures and mesoscale eddies with distinct O_2 concentrations in their interior can penetrate the OMZ and cause ventilation events of non-negligible magnitude. Overall, between 200 and 600 meters depth, turbulent eddy fluxes of O_2 into the OMZ are one order of magnitude higher than mean eddy fluxes.

A coastal filament in the Western Iberia peninsula was studied in chapter 6. The cold water filament was found to be characterized by zero FSLE values, indicating that the water mass that constitutes the filament is not subject to large straining or divergence. The offshore transport inside the filament is dependent on depth, with the position of the ridges of the 3d FSLE field along the depth determining the ultimate fate of the transported water masses. The structure of the 3d FSLE ridges show that the filament is limited by the 3d Lagrangian boundaries of adjacent mesoscale eddies and by the overall 3d mesoscale configuration of the flow in the region.

Appendices

Numerical Methods

Numerical methods used in this work are described here. The bulk of the methods used were methods to integrate ordinary differential equations to obtain particle trajectories (section A.1.3), to perform interpolation of 2d and 3d scalar fields defined in regular and irregular grids (section A.1) and to differentiate such fields (section A.2). The stretched vertical layer distribution used in some FSLE field calculations is described in section A.3.

A.1

Interpolation in the ROMS grid

In this work extensive use was made of interpolation techniques, especially in the particle trajectory integration. Generally speaking, interpolation was necessary when the position of the particle did not coincide with any grid node in the velocity grid. The velocity and scalar fields utilized in this thesis were mainly 3d and time dependent obtained from simulations with the ROMS hydrodynamic model so here we present the techniques used for interpolation in this kind of data grids.

A.1.1 The ROMS curvilinear, terrain following grid

The ROMS model uses a 3d curvilinear, terrain following grid (Figure A.1). The curvilinear horizontal grid is orthogonal and boundary fitted with laterally variable resolution. The horizontal grid node locations are integer values of the

APPENDIX A. NUMERICAL METHODS

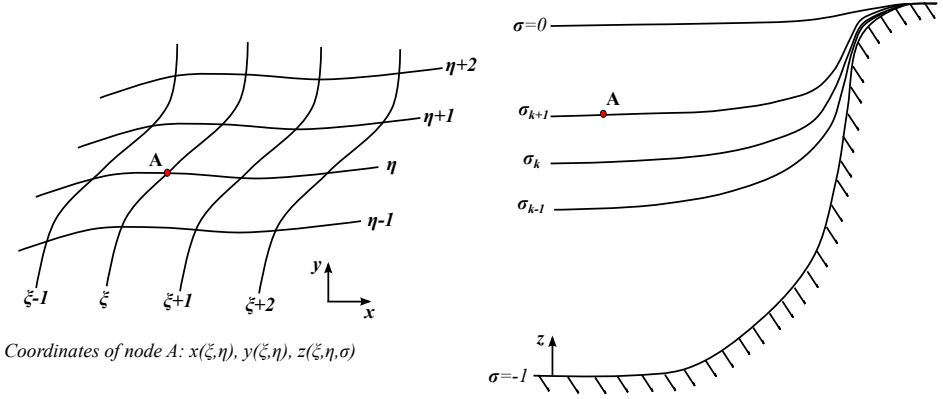


Figure A.1: Left: curvilinear horizontal ROMS grid; Right: Vertical terrain following grid.

grid coordinates (ξ, η) . Thus the first coordinate of the particle position, ξ , varied from 1 to M , where M is the maximum index of the grid coordinate in the direction of ξ . Similarly, for the 2nd and 3rd coordinates η and σ , their values lay in the interval between 1 and the respective grid dimensions N and L .

A.1.2 Interpolation procedure

To find the value of a scalar variable ϕ anywhere in the ROMS grid it is necessary to interpolate the scalar values stored in the grid nodes. Given a point $P(x_p, y_p, z_p)$ inside the ROMS grid, the interpolation proceeds by first determining the grid nodes that surround P , such that $x(\xi, \eta) < x < x(\xi + 1, \eta)$ and $y(\xi, \eta) < y < y(\xi, \eta + 1)$ (Figure A.2). Then, at each of the four horizontal grid nodes $W_1 = (\xi, \eta)$, $W_2 = (\xi + 1, \eta)$, $W_3 = (\xi + 1, \eta + 1)$ and $W_4 = (\xi, \eta + 1)$ we compute the σ'_k levels such that $z(W_k, \sigma'_k) = z_p$. At each point $P_k = (W_k, \sigma'_k)$, the value of the scalar field ϕ_k is computed by 1d interpolation along the water column located at W_k , i.e., $\phi_k = I(\phi(W_k, :))$, where I is a generic 1d interpolant (linear, cubic, spline, etc.). At this moment we possess scalar values in a regular grid square with corners P_k so that we may find the value ϕ_p by any method of 2d interpolation. If in both interpolation steps, linear interpolation is used then the procedure reduces to using trilinear interpolation in a regular 3d grid (ξ, η, σ) .

A.1. INTERPOLATION IN THE ROMS GRID

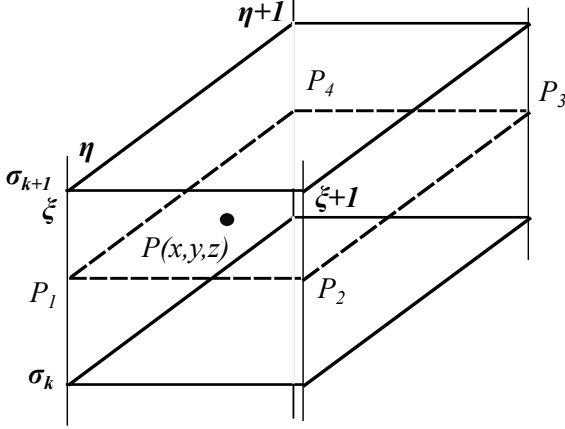


Figure A.2: Interpolation of scalar ϕ in the ROMS curvilinear grid.

A.1.3 Trajectory integration in curvilinear coordinates

In the case where the full grid information was available (the ROMS grid information file) the particle trajectories were described using the grid coordinates instead of the actual underlying physical coordinates (distances in meters or degrees). The advantage of this approach is that, in what concerns interpolation, the particles are moving in a regular 3d grid, instead of the original curvilinear, terrain-following ROMS grid.

In order to use this regular (ξ, η, σ) grid, the velocity components that are computed by the model in physical units (u, v, w) must be transform to grid units $(\tilde{u}, \tilde{v}, \tilde{w})$. This is accomplished by multiplying the velocity vector by the grid metric:

$$\tilde{u} = u \frac{\partial \xi}{\partial x}, \quad (\text{A.1})$$

$$\tilde{v} = v \frac{\partial \eta}{\partial y}, \quad (\text{A.2})$$

$$\tilde{w} = w \frac{\partial \sigma}{\partial z}. \quad (\text{A.3})$$

All grid metric terms are approximated as finite differences, e.g., $\frac{\partial \sigma}{\partial z} \approx \frac{\Delta \sigma}{\Delta z}$.

APPENDIX A. NUMERICAL METHODS

A.2

Differentiation of scalar fields

The differentiation of scalar fields was used to obtain gradient vector components. The scalar fields were differentiated in a curvilinear grid either in the ROMS format or a simple latitude-longitude grid, which is curvilinear in an (x, y) frame. Moreover, differentiation was carried out in constant depth horizontal (z level) or in variable depth horizontal grids (σ level) such as in the case of the ROMS grid.

To differentiate a scalar field ϕ in the ROMS grid, i.e. to find the partial derivatives $\partial\phi/\partial x$, $\partial\phi/\partial y$ and $\partial\phi/\partial z$, we must first find the derivatives with respect to the grid coordinates (ξ, η, σ) – $\partial\phi/\partial\xi$, $\partial\phi/\partial\eta$ and $\partial\phi/\partial\sigma$ – that are readily available using any finite difference differentiation formula.

The relationship between both sets of partial derivatives is given by

$$\frac{\partial\phi}{\partial x} = \frac{\partial\phi}{\partial\xi} \frac{\partial\xi}{\partial x} + \frac{\partial\phi}{\partial\eta} \frac{\partial\eta}{\partial x} + \frac{\partial\phi}{\partial\sigma} \frac{\partial\sigma}{\partial x}, \quad (\text{A.4})$$

$$\frac{\partial\phi}{\partial y} = \frac{\partial\phi}{\partial\xi} \frac{\partial\xi}{\partial y} + \frac{\partial\phi}{\partial\eta} \frac{\partial\eta}{\partial y} + \frac{\partial\phi}{\partial\sigma} \frac{\partial\sigma}{\partial y}, \quad (\text{A.5})$$

$$\frac{\partial\phi}{\partial z} = \frac{\partial\phi}{\partial\xi} \frac{\partial\xi}{\partial z} + \frac{\partial\phi}{\partial\eta} \frac{\partial\eta}{\partial z} + \frac{\partial\phi}{\partial\sigma} \frac{\partial\sigma}{\partial z}. \quad (\text{A.6})$$

Using an indicial notation for simplicity, let x_i be a cartesian coordinate and ξ_j a grid (curvilinear) coordinate, then we have

$$\frac{\partial\phi}{\partial x_i} = \frac{\partial\phi}{\partial\xi_j} \frac{\partial\xi_j}{\partial x_i} = \frac{\partial\phi}{\partial\xi_j} \beta^{ij}, \quad (\text{A.7})$$

where J is the Jacobian

$$J = \det(G_{ij}) = \det\left(\frac{\partial x_i}{\partial \xi_j}\right), \quad (\text{A.8})$$

and β^{ij} is the cofactor of G_{ij} . In the ROMS terrain following curvilinear grid, the following terms are zero: $\partial x/\partial\sigma$, $\partial y/\partial\sigma$.

In the case of constant z levels, the differentiation is simplified by the fact that the terms $\partial z/\partial\xi$ and $\partial z/\partial\eta$ vanish and the σ and z coordinates coincide ($\partial z/\partial\sigma = 1$).

A.3. THE STRECHED VERTICAL NODE DISTRIBUTION

A.3

The streched vertical node distribution

In the FSLE grid definition, a vertical level distribution with variable spacing was used in some calculations. This distribution is defined by a clustering length parameter h_θ and clustering parameter θ_s such that the k level's depths is given by:

$$z_k = h_\theta \sigma_k + (z_s - (z_b + h_\theta)) C_k - z_b , \quad (\text{A.9})$$

where $\sigma_k, k = 1, \dots, N_z$ is a linearly varying variable between -1 and 0; h_θ is a depth above which the density of nodes increases and C_k is the clustering function given by

$$C_k = \frac{1 - \cosh(\theta_s \sigma_k)}{\cosh \theta_s - 1} . \quad (\text{A.10})$$

The surface and bottom depths are z_s and z_b respectively. The bottom is assumed to be flat so that the levels are horizontal.

List of Tables

3.1	Simulation parameters. Quantities with ⁺ refer to wall units. L_x , 2δ and L_z are the domain sizes in the x , y and z directions. Δx^+ , Δy^+ and Δz^+ are the respective spatial resolutions (given at the first point above the wall for the y case), and n_x , n_y and n_z the corresponding number of grid points. $Re = U\delta/\nu$ is the Reynolds number based on the channel center mean speed, whereas $Re_\tau = u_\tau\delta/\nu$ is the viscous Reynolds number. The nominal value is an input to the computer code, and the actual value comes by using Eq. (3.4) for the computed mean profile $U(y)$	50
3.2	FSLE calculation parameters. dt is the integration time step and Δt the maximum integration time.	53
5.1	Eddy and mean O_2 flow rates across the $20 \mu M$ mean boundaries from 200 to 600 m depth and from coast to $88^\circ W$	108

List of Figures

1.1	Time and space scales of oceanic processes. Adapted from [3]. . . .	5
1.2	Mechanical energy balance for the world's oceans in TW [4]. KE – Kinetic Energy. GPE – Gravitational Potential Energy.	6
1.3	Global map of SSH on 28 August 1996 constructed from the merged T/P and ERS-1 data after spatially high-pass filtering with half-power filter cutoffs of 20° of longitude by 10° of latitude [13].	8
1.4	Ekman transport divergence near the equator driven by easterly trade winds. Top: Ekman transports; Bottom: Meridional cross-section showing effect on the thermocline and surface temperature. Adapted from [23].	9
1.5	Coastal upwelling system due to an alongshore wind with offshore Ekman transport (Northern Hemisphere). Adapted from [23]. . . .	10
2.1	Stable E^s and unstable E^u invariant subspaces of a fixed point x^* in 2d phase-space. Trajectories $\mathbf{a}(t)$ and $\mathbf{b}(t)$ approach the fixed point along E^s and leave along E^u at exponential rates.	17
2.2	Energy cascade in 3d turbulence. $E(k)$ is the turbulent kinetic energy spectrum as function of wavenumber k . The large scale mean flow has characteristic length scale L and η is the length scale at which viscous dissipation of turbulent fluctuations occurs.	21

LIST OF FIGURES

2.3	Energy and enstrophy cascade in 2d turbulence. $E(k)$ is the turbulent kinetic energy spectrum as function of wavenumber k . Energy is supplied at $k = 1/l_e$ and dissipated at the large scale mean flow has $k = 1/L$ by friction.	24
2.4	Coherent structures in an 3d turbulent boundary layer (from [84]).	26
2.5	Vorticity field from a numerical simulation of freely decaying two-dimensional turbulence (from [78]). Bright and dark tones indicate negative and positive vorticity respectively.	27
2.6	Gradient of a conserved scalar q . The scalar isolines q and $q+dq$ are also material lines. As \mathbf{ds} grows or decays the norm of the scalar gradient decays or grows. Fast growth of the gradient norm is found when particles diverge exponentially in the direction normal to the gradient orientation.	32
2.7	Time evolution of a fluid patch (gray) in the vicinity of attracting (blue) and repelling (green) coherent structures. A) Forward in time. B) Backward in time. Arrows indicate forward in time direction of trajectories <i>on</i> the coherent structure.	38
2.8	Computational setup for the calculation of the FSLE field in 3d. The FSLE at the location of the central particle (\circ) is a measure of the time it takes for any of the neighbor particles (\bullet) to diverge from the central particle by a distance greater than δ_f	41
3.1	Mean velocity profile $U(y)/u_\tau$. Solid line: our simulations; squares: [119]; dashed line: logarithmic profile $U(y)/u_\tau = 2.5 \log(y^+) + 5.5$.	51
3.2	Reynolds stress $\overline{u'v'}$ profile at $Re_\tau = 180$. Solid line: our simulations; squares: [119] (given up to the channel centerline).	52
3.3	Instantaneous FSLE field at $t = 420$ shown on a streamwise/wall-normal plane in the turbulent channel. Walls are at the top and bottom of the figure. Mean velocity is in the streamwise direction from left to right.	54
3.4	FSLE profile averaged over (x, z) , as a function of the cross-stream normalized coordinate y^+ . Only half of the channel is shown since the profile is quasi-symmetric about the channel centerline.	54

LIST OF FIGURES

3.5	Streamwise correlation function $R_{xx}(y^+; \bar{x}^+)$ as a function of the streamwise separation \bar{x}^+ , at four distances from the lower wall: Continuous line: $y^+ = 4$; dashed line $y^+ = 12.2$; dash-dot line $y^+ = 28.4$; dotted line: $y^+ = 122.1$	56
3.6	Spanwise correlation function $R_{zz}(y^+; \bar{z}^+)$ as a function of the spanwise separation \bar{z}^+ , at four distances from the lower wall: Continuous line: $y^+ = 4$; dashed line $y^+ = 12.2$; dash-dot line $y^+ = 28.4$; dotted line: $y^+ = 122.1$	56
3.7	Instantaneous FSLE field in plane parallel to the wall at $y^+ = 4$. The time is the same as in figure 3.3	57
3.8	Mechanism for the rapid separation of fluid from the near wall viscous sublayer. The mean flow is into the page.	58
3.9	FSLE map in a (z, y) plane located at $x = 6.0$ ($x^+ = 1034$). The time of the map is $t = 413.8$. together with a set of particles initially located in rectangular region $z^+ \in [345, 380]$ and $y^+ \in [3.4, 13.8]$. The particles were released at $t = 409$. Particle trajectories were integrated using only the spanwise and wall normal velocity components. The mean flow is moving out of the page.	59
3.10	Instantaneous turbulent velocity components at $x = 6.0$ ($x^+ = 1034$) and $t = 413.75$. Velocity vectors correspond to the inplane velocity components (w, v) , together with contours of streamwise turbulent velocity u . Dashed contours are negative u (into the paper) and continuous contours are positive u (from the paper). . .	60
3.11	Propagation velocity of FSLE field (V^+) and mean flow (U^+). . .	62
3.12	3d attracting LCS in the channel flow together with a FSLE map at the fixed plane $x = 6.0$ ($x^+ = 1034$). Time goes from top to bottom, at intervals of 0.1 time units. The flow direction is in the positive x direction in each panel, and a wall is at the bottom. The sequence shows how one of the flow structures is advected and passes through the $x = 6.0$ plane.	63
4.1	Benguela ocean region. The velocity field domain is limited by the continuous black line. The FSLE calculation area is limited by the dash-dot black line. Bathymetric contour lines are from ETOPO1 global relief model [125] starting a 0 m depth up to 4000 m at 500 m interval.	71

LIST OF FIGURES

4.2	Vertical profile of 30 day average backward and forward FSLE. The 30 day average field was spatially averaged at each layer over the FSLE calculation area to produce the vertical profiles. The backward FSLE average is shown in continuous and the forward FSLE is shown in dashed.	75
4.3	Attracting LCS (blue) for day 1 of the calculation period, together with horizontal slices of the backward FSLE field at 120 m and 300 m depth. Colorbar refers to colormap of horizontal slices. The units of the colorbar are day^{-1}	76
4.4	Trajectory (advancing from NE to SW) of the eddy center inside the calculation domain. Circles indicate the center location during the 30 day FSLE calculation period, and squares previous and posterior positions. Bathymetric lines same as in figure 4.1.	77
4.5	Colormap of Q -criterion. White contours have $Q = 0$. Day 1 of the 30 day FSLE calculation period. Left panel: Latitude $24.5^{\circ}S$; Righth panel: Longitude $10.5^{\circ}E$. Colorbar values are $Q \times 10^{10} s^{-2}$	79
4.6	Q -criterion map at 200 m depth together with patches of backward (blue) and forward (green) FSLE values. Black dashed lines have $Q = 0$. FSLE patches contain the highest 60% of FSLE values. Colorbar values are $Q \times 10^{10} s^{-2}$. The eddy we study is the clear region in between points H1 and H2.	80
4.7	3d LCSs around the mesoscale eddy at day 1 of the 30 day FSLE calculation period. Green: repelling LCS; Blue: attracting LCS.	81
4.8	Three dimensional view of the evolution of elliptic patches released at different depths inside of the eddy at day 1 of the 30 day FSLE calculation period. Top left: day 3; Top right: day 13; Bottom left: day 19; Bottom right: day 29. Red: 40 m; Yellow: 100 m; Cyan: 200 m; Magenta: 300 m; Grey: 400 m; Black: 500 m. Attracting LCS are shaded in blue while repelling LCS are shaded in green.	82
4.9	Top view of the evolution of particle patches and LCSs shown in Fig. 8. Top left: day 3; Top right: day 13; Bottom left: day 19; Bottom right: day 29. Colors as in figure 4.8.	84
4.10	Top view of the initial stages of evolution of the particle patches and LCSs of Figs. 8 and 9. Top left: day 7; Top right: day 9; Bottom left: day 11; Bottom right: day 13. Colors as in figure 4.8.	85
4.11	Percentage of particles outside a 200 km diameter circle centered at the eddy center, as a function of time.	86

LIST OF FIGURES

5.1	Map of backward FSLE for the 1 st of January of year 21. A) 10 m depth. B) 113 m depth. C) 410 m depth. D) 592 m depth. Note the different colorbar at different depths.	93
5.2	Vertical map of backward FSLE for the 1 st of January of year 21, at 16.45° S.	94
5.3	Horizontal maps of backward FSLE temporally averaged for year 21. A) 10 m depth. B) 113 m depth. C) 410 m depth. D) 592 m depth. Note the different colorbar at different depths.	95
5.4	Time mean of the horizontally averaged depth profile of the backward FSLE field $\langle \lambda \rangle$ (in day ⁻¹) for year 21.	96
5.5	Residence times (RT) at 410 m depth for 1 st July of year 20. A) Backward RT. Superimposed white lines are 0.035 day ⁻¹ backward FSLE isolines. B) Forward RT. Superimposed white lines are 0.038 day ⁻¹ forward FSLE isolines. The magenta lines bound the region inside which the concentration of O ₂ was smaller than 20μM already at the initial time, so that outside these lines the exit times are zero. The red color associated to a residence time of 2.5 years is in fact associated also to all residence times larger than this duration.	97
5.6	Mean O ₂ and FSLE fields and correlations for simulation year 21. a) 20 μM isosurface of mean O ₂ concentration rendered together with an horizontal plane at 410 meters depth displaying at the mean FSLE field. The vertical scale is nonlinear and stretched in the upper 500 m depth. The solid volume with the flat top is the Peruvian coast. b) Zonally averaged mean FSLE and O ₂ gradient, averaged between 380 m and 600 m depth. C) Pearson correlation coefficient (R) between zonally averaged mean FSLE and O ₂ gradient as a function of depth (solid line). Upper and lower bounds of R give the Fisher 95% confidence interval (dashed-lines).	99
5.7	Lines of high FSLE values (> 0.04 day ⁻¹ , black) superimposed on instantaneous O ₂ and O ₂ gradient fields on 1 st of March of year 21 at 410 m depth. A) O ₂ concentration. B) O ₂ horizontal gradient.	101
5.8	Mean fields averaged over 300 – 600 meters depth and during year 21. A) FSLE. B) O ₂ horizontal gradient.	101

LIST OF FIGURES

- 5.9 Entrainment of O_2 rich waters into the OMZ due to LCS motion. Color codifies O_2 at 410 m depth and the lines are the $0.075day^{-1}$ FSLE isolines. a) 16 September; b) 7 October; c) 25 October; all of simulation year 21. Note the oxygen-rich tongue entering the OMZ at $80 - 82^\circ W$. White continuous line is the $20 \mu M$ mean isoline at 410 m depth (corresponding to the southern OMZ frontier). . . . 103
- 5.10 Hovmöller plots of O_2 concentration anomalies at OMZ boundaries at 410 m depth during simulation year 21. A) Northern boundary. B) Southern boundary. Anomaly measured relative to $20 \mu M$ level. Distance along boundary increases towards offshore. So, coast is at the right and the anomalies propagate offshore. 104
- 5.11 Vertical profiles of mean FSLE and normal eddy flux averaged along the northern and southern OMZ boundaries from the coast until $88^\circ W$ for each depth. Blue lines are for FSLE values and red lines for eddy fluxes. a) Northern boundary. b) Southern boundary. 106
- 5.12 Vertical profiles of O_2 fluxes at the $20\mu M$ OMZ mean boundaries between 200 and 600 m depth. The fluxes have been averaged along the horizontal extension of the boundary (from coast to $88^\circ W$) for each depth, and during year 21. A) Eddy flux profile (these are the red curves in Fig. 5.11). B) Mean flux profile (note the much smaller values as compared with the eddy fluxes.) 107
- 5.13 Climatological normalized cross-wavelet spectrum of O_2 concentration and FSLE time series at (A) CORE, (B) BNDSOUTH and (C) BNDNORTH. The horizontal axis indicates the calendar month. Units of the colorbar are $0.8 \times 10^{-4} M day^{-1}$. The white thick contour in all panels indicates the 95% confidence level. . . 109
- 6.1 Western Iberia domain. Black full line: ROMS simulation domain; Red dash-dot line: FSLE fields domain; Green dash-dot line: Ridge extraction domain. 115
- 6.2 Backward FSLE field at 24th of September 2007. A) 9.8 m depth; B) 17.1 m depth; C) 31.8 m depth; D) 96.8 m depth. 116
- 6.3 Filament evolution. A) Sea surface temperature and backward FSLE contours ($0.1 day^{-1}$) at 09/09/2007; B) 20/09/2007; C) 24/09/2007; D) 06/10/2007. 119

LIST OF FIGURES

6.4	Vertical section of backward FSLE taken at $10^{\circ}15'$ W at the 24/09/2007. The FSLE field was smoothed and filtered to improve clarity. The filament area is highlighted in the white rectangle.	120
6.5	Location of the profile path taken along the filament at the 26/09/2007. FSLE map at 14.7 m depth. Brown circles are the nodes of the profile.	121
6.6	Profiles along filament at 26/09/2007. A) Backward FSLE; B) Temperature; C) Salinity. White vertical lines represent locations of profile nodes. Fields were interpolated linearly in between nodes. Distance along profile increases towards the offshore.	122
6.7	Trajectories of particles released at the root of the filament. A) Horizontal trajectories; B) Vertical and longitudinal displacement along the particles trajectories. Particles were release at $9^{\circ}30'$ W at 26/09/2007 at 7, 12, 24, 29 and 34 m depth and were integrated until year's end. Only the particles that traveled offshore of $10^{\circ}30'$ W are shown, until they crossed the same longitude in the opposite direction.	123
6.8	Temperature-Salinity (T-S) diagram of particles released at the root of the filament. Black lines in the diagram are constant density lines. Crosses indicate the T-S properties at the release location.	125
6.9	Ridges of the 3d FSLE field defining the filament. Ridges extracted the 26/09/2007. Green: boundary of the anticyclone; Blue: boundary of the cyclone; Red: Ridge separating the two dipoles mention earlier in section 6.3.1. A) Horizontal FSLE field at 20 m depth; B) Horizontal FSLE field at 45 m depth.	127
6.10	Ridges of the 3d FSLE field defining the filament. Ridges extracted the 26/09/2007. Green: boundary of the anticyclone; Blue: boundary of the cyclone; Red: Ridge separating the two dipoles mention earlier in section 6.3.1. A) Temperature. B) Salinity. Temperature and salinity are shown in a vertical plane normal to the filament axis that passes through $10^{\circ}27'$ W.	128
A.1	Left: curvilinear horizontal ROMS grid; Right: Vertical terrain following grid.	138
A.2	Interpolation of scalar ϕ in the ROMS curvilinear grid.	139

Bibliography

Bibliography

- [1] H. Tennekes and J. L. Lumley, *A First Course in Turbulence*, The MIT Press, 1972.
- [2] P. Müller and C. Garrett *Oceanography* **15**(3), pp. 12–19, 2002.
- [3] T. D. Dickey *Journal of Marine Systems* **40–41**(0), pp. 5–48, 2003.
- [4] R. Huang *Encyclopedia of Energy* **4**, pp. 497–509, 2004.
- [5] A. C. de Verdier, “On the oceanic thermohaline circulation,” in *Modelling Oceanic Climate Interactions*, pp. 151–183, Springer, 1993.
- [6] R. X. Huang *Journal of Physical Oceanography* **29**(4), pp. 727–746, 1999.
- [7] W. Munk and C. Wunsch *Deep Sea Research Part I: Oceanographic Research Papers* **45**(12), pp. 1977–2010, 1998.
- [8] J. Luyten, J. Pedlosky, and H. Stommel *Journal of Physical Oceanography* **13**(2), pp. 292–309, 1983.
- [9] B. Qiu and R. X. Huang *Journal of Physical Oceanography* **25**(10), pp. 2374–2390, 1995.
- [10] A. Gill, J. Green, and A. Simmons, “Energy partition in the large-scale ocean circulation and the production of mid-ocean eddies,” in *Deep Sea Research and Oceanographic Abstracts*, **21**, pp. 499–528, Elsevier, 1974.
- [11] D. B. Chelton, M. G. Schlax, R. M. Samelson, and R. A. de Szoeke *Geophysical Research Letters* **34**(15), 2007.
- [12] D. B. Chelton and M. G. Schlax *Science* **272**(5259), pp. 234–238, 1996.
- [13] D. B. Chelton, M. G. Schlax, and R. M. Samelson *Progress in Oceanography* **91**(2), pp. 167–216, 2011.
- [14] P. Le Traon and R. Morrow *International Geophysics* **69**, pp. 171–xi, 2001.
- [15] L. Thomas, A. Tandon, and A. Mahadevan, “Submesoscale ocean processes and dynamics,” in *Ocean Modeling in an Eddying Regime, Geophysical Monograph 177*, M. Hecht and H. Hasume, eds., pp. 17–38, American Geophysical Union, 2008.

BIBLIOGRAPHY

- [16] P. Klein and G. Lapeyre *Annual Review of Marine Science* **1**, pp. 351–375, 2009.
- [17] A. Bakun, *Patterns in the ocean. Ocean processes and marine population dynamics*, California Sea Grant College System, NOAA and Centro de Investigaciones Biológicas del Noroeste, La Paz, BCS México, 1996.
- [18] V. C. Garçon, A. Oschlies, S. C. Doney, D. McGillicuddy, and J. Waniek *Deep Sea Research Part II: Topical Studies in Oceanography* **48**(10), pp. 2199–2226, 2001.
- [19] M. Lévy, P. Klein, and A.-M. Treguier *Journal of Marine Research* **59**(4), pp. 535–565, 2001.
- [20] M. Lévy *Lecture Notes in Physics* **744**, pp. 219–261, 2008.
- [21] D. A. Byrne, A. L. Gordon, and W. F. Haxby *J. Phys. Oceanogr.* **25**, pp. 902–917, 1995.
- [22] Y. Lehahn, F. d’Ovidio, M. Lévy, Y. Amitai, and E. Heifetz *Geophys. Res. Lett.* **38**, p. L16610, 2011.
- [23] L. D. Talley, G. L. Pickard, W. J. Emery, and J. H. Swift, *Descriptive physical oceanography: an introduction*, Academic Press, 2011.
- [24] V. Rossi, C. López, J. Sudre, E. Hernández-García, and V. Garçon *Geophys. Res. Lett.* **35**, p. L11602, 2008.
- [25] D. Pauly and V. Christensen *Nature* **374**, pp. 255–257, 1995.
- [26] K. Brink *Progress in Oceanography* **12**(3), pp. 223–257, 1983.
- [27] J. Kurian, F. Colas, X. Capet, J. C. McWilliams, and D. B. Chelton *Journal of Geophysical Research: Oceans (1978–2012)* **116**(C8), 2011.
- [28] A. Chaigneau, G. Eldin, and B. Dewitte *Progress in Oceanography* **83**(1), pp. 117–123, 2009.
- [29] F. Colas, X. Capet, J. C. McWilliams, and Z. Li *Journal of Physical Oceanography* **43**(6), pp. 1073–1095, 2013.
- [30] X. Capet, J. McWilliams, M. Molemaker, and A. Shchepetkin *Journal of Physical Oceanography* **38**(1), pp. 29–43, 2008.
- [31] N. Gruber, Z. Lachkar, H. Frenzel, P. Marchesiello, M. Munnich, J. McWilliams, T. Nagai, and G. Plattner *Nature Geoscience* **4**(11), pp. 787–792, 2011.

BIBLIOGRAPHY

- [32] V. Rossi, C. López, E. Hernández-García, J. Sudre, V. Garçon, and Y. Morel *Nonlinear Processes Geophys* **16**, pp. 557–568, 2009.
- [33] A. Doglioli, B. Blanke, S. Speich, and G. Lapeyre *Journal of Geophysical Research C: Oceans* **112**(5), p. C05043, 2007.
- [34] A. Rubio, B. Blanke, S. Speich, N. Grima, and C. Roy *Progress In Oceanography* **83**(1–4), pp. 288–295, 2009.
- [35] A. Nurser and J. Zhang *Journal of Geophysical Research: Oceans (1978–2012)* **105**(C9), pp. 21851–21868, 2000.
- [36] G. Lapeyre and P. Klein *Journal of Marine Research* **64**(6), pp. 835–851, 2006.
- [37] D. J. McGillicuddy, A. R. Robinson, D. A. Siegel, H. W. Jannasch, R. Johnson, T. D. Dickey, J. McNeil, A. F. Michaels, and A. H. Knap *Nature* **394**, pp. 263–266, 1998.
- [38] A. Oschlies and V. Garçon *Nature* **394**, pp. 266–269, 1998.
- [39] P. Calil and K. Richards *Journal of Geophysical Research: Oceans (1978–2012)* **115**(C2), 2010.
- [40] P. G. Falkowski, D. Ziemann, Z. Kolber, and P. K. Bienfang *Nature* **352**, pp. 55–58, jul 1991. 10.1038/352055a0.
- [41] D. A. Siegel, D. J. McGillicuddy, and E. A. Fields *Journal of Geophysical Research: Oceans (1978–2012)* **104**(C6), pp. 13359–13379, 1999.
- [42] A. P. Martin and K. J. Richards *Deep Sea Research Part II: Topical Studies in Oceanography* **48**(4), pp. 757–773, 2001.
- [43] D. McGillicuddy, L. Anderson, S. Doney, and M. Maltrud *Global Biogeochemical Cycles* **17**(2), 2003.
- [44] D. J. McGillicuddy, L. A. Anderson, N. R. Bates, T. Bibby, K. O. Buesseler, C. A. Carlson, C. S. Davis, C. Ewart, P. G. Falkowski, S. A. Goldthwait, et al. *Science* **316**(5827), pp. 1021–1026, 2007.
- [45] D. Elhmaidi, A. Provenzale, and A. Babiano *J. Fluid Mech.* **257**, pp. 533–558, 1993.
- [46] B. Hoskins, I. Draghici, and H. Davies *Quarterly Journal of the Royal Meteorological Society* **104**(439), pp. 31–38, 1978.

BIBLIOGRAPHY

- [47] R. T. Pollard and L. A. Regier *Journal of Physical Oceanography* **22**, pp. 609–625, 1992.
- [48] A. J. Mariano, A. Griffa, T. Özgökmen, and E. Zambianchi *J. Atmos. Oceanic Technol.* **19**, pp. 1114–1126, 2002.
- [49] J. Lacasce *Progress in oceanography* **77**, pp. 1–29, 2008.
- [50] G. Haller *Chaos* **10**(1), pp. 99–108, 2000.
- [51] G. Haller and G. Yuan *Physica D* **147**, pp. 352–370, 2000.
- [52] G. Boffetta, G. Lacorata, G. Radaelli, and A. Vulpiani *Physica D* **159**(1-2), pp. 58–70, 2001.
- [53] G. Haller *Phys. Fluids* **A14**, pp. 1851–1861, 2002.
- [54] F. d’Ovidio, V. Fernández, E. Hernández-García, and C. López *Geophysical Research Letters* **31**(17), 2004.
- [55] F. d’Ovidio, J. Isern, C. López, E. Hernández-García, and E. García-Ladona *Deep-Sea Res. I* **56**, pp. 15–31, 2009.
- [56] A. M. Mancho, D. Small, and S. Wiggins *Phys. Rep.* **437**, pp. 55–124, 2006.
- [57] E. Tew Kai, V. Rossi, J. Sudre, H. Weimerskirch, C. López, E. Hernández-García, F. Marsac, and V. Garçon *Proc. Natl. Acad. Sci. U.S.A.* **106**(20), pp. 8245–8250, 2009.
- [58] M. Olascoaga *Nonlinear processes in geophysics* **17**(6), p. 685, 2010.
- [59] P. du Toit and J. Marsden *J. Fixed Point Theory Appl.* **7**, pp. 351–384, 2010.
- [60] W. Tang, P. W. Chan, and G. Haller *Journal of Applied Meteorology and Climatology* **50**, pp. 325–338, 2011.
- [61] P. Tallapragada, S. D. Ross, and D. G. Schmale III *Chaos* **21**(3), p. 033122, 2011.
- [62] M. A. Green, C. W. Rowley, and G. Haller *J. Fluid Mech.* **572**, pp. 111–120, 2007.
- [63] G. Haller *Physica D* **149**, pp. 248–277, 2001.
- [64] M. Branicki and R. Malek-Madani *Nonlinear Processes in Geophysics* **17**(2), pp. 149–168, 2010.

BIBLIOGRAPHY

- [65] M. Branicki, A. M. Mancho, and S. Wiggins *Physica D* **240**, pp. 282–304, 2011.
- [66] S. Wiggins, *Introduction to Applied Nonlinear Dynamical Systems and Chaos, second edition*, Springer-Verlag, New York, 2003.
- [67] G. K. Batchelor, *An introduction to fluid dynamics*, Cambridge university press, 2000.
- [68] H. Tennekes and J. L. Lumley, *A first course in turbulence*, MIT press, 1972.
- [69] L. F. Richardson, *Weather prediction by numerical process*, Cambridge University Press, 1922.
- [70] G. I. Taylor *Proceedings of the Royal Society of London. Series A-Mathematical and Physical Sciences* **164**(919), pp. 476–490, 1938.
- [71] W. D. McComb, *The physics of fluid turbulence*, Oxford University Press, Dec. 1990.
- [72] A. N. Kolmogorov, “The local structure of turbulence in incompressible viscous fluid for very large Reynolds numbers,” in *Dokl. Akad. Nauk SSSR*, **30**(4), pp. 299–303, 1941.
- [73] A. N. Kolmogorov, “Dissipation of energy in locally isotropic turbulence,” in *Dokl. Akad. Nauk SSSR*, **32**(1), pp. 16–18, 1941.
- [74] J. G. Charney *Journal of the Atmospheric Sciences* **28**(6), pp. 1087–1095, 1971.
- [75] P. B. Rhines *Annual Review of Fluid Mechanics* **11**(1), pp. 401–441, 1979.
- [76] P. Tabeling *Physics Reports* **362**(1), pp. 1–62, 2002.
- [77] G. Boffetta and R. E. Ecke *Annu. Rev. Fluid Mech.* **44**, pp. 427–451, 2012.
- [78] A. Provenzale *Annu. Rev. Fluid Mech.* **31**, pp. 55–93, 1999.
- [79] H. Fiedler *Progress in Aerospace Sciences* **25**(3), pp. 231–269, 1988.
- [80] R. J. Adrian *Phys. Fluids* **19**, p. 041301, 2007.
- [81] J. Jeong and F. Hussain *J. Fluid Mech.* **285**, pp. 69–94, 1995.
- [82] J. Jeong, F. Hussain, W. Schoppa, and J. Kim *Journal of Fluid Mechanics* **332**, pp. 185–214, 1997.

BIBLIOGRAPHY

- [83] S. K. Robinson *Annu. Rev. Fluid Mech.* **23**, pp. 601–639, 1991.
- [84] M. Van Dyke and M. Van Dyke, *An album of fluid motion*, Parabolic Press Stanford, 1982.
- [85] J. C. McWilliams *Journal of Fluid Mechanics* **146**, pp. 21–43, 1984.
- [86] A. Bennett *Journal of the atmospheric sciences* **41**(11), pp. 1881–1886, 1984.
- [87] L. F. Richardson *Proceedings of the Royal Society of London. Series A, Containing Papers of a Mathematical and Physical Character*, pp. 709–737, 1926.
- [88] J.-T. Lin *Journal of the Atmospheric Sciences* **29**(2), pp. 394–396, 1972.
- [89] Z. Neufeld and E. Hernández-García, *Chemical and biological processes in fluid flows: a dynamical systems approach*, Imperial College Press, 2009.
- [90] C. Eckart *J. Mar. Res* **7**(3), pp. 265–275, 1948.
- [91] I. I. Rypina, L. J. Pratt, J. Pullen, J. Levin, and A. L. Gordon *Journal of Physical Oceanography* **40**(9), pp. 1988–2006, 2010.
- [92] M. Tabor and I. Klapper *Chaos, Solitons & Fractals* **4**(6), pp. 1031–1055, 1994.
- [93] S. Wiggins *Annu. Rev. Fluid Mech.* **37**, pp. 295–328, 2005.
- [94] J.-P. Eckmann and D. Ruelle *Reviews of modern physics* **57**(3), p. 617, 1985.
- [95] V. Artale, G. Boffetta, A. Celani, M. Cencini, and A. Vulpiani *Phys. Fluids* **9**, pp. 3162–3171, 1997.
- [96] E. Aurell, G. Boffetta, A. Crisanti, G. Paladin, and A. Vulpiani *J. Phys. A* **30**(1), pp. 1–26, 1997.
- [97] E. Aurell, G. Boffetta, A. Crisanti, G. Paladin, and A. Vulpiani *Physical review letters* **77**(7), p. 1262, 1996.
- [98] G. Lacorata, E. Aurell, and A. Vulpiani *Ann. Geophysicae* **19**, pp. 121–129, 2001.
- [99] I. Hernandez-Carrasco, C. López, E. Hernández-García, and A. Turiel *Ocean Modell.* **36**, pp. 208–218, 2011.
- [100] G. Haller and G. Yuan *Physica D* **147**(3-4), pp. 352–370, 2000.

BIBLIOGRAPHY

- [101] S. C. Shadden, F. Lekien, and J. E. Marsden *Physica D* **212**, pp. 271–304, 2005.
- [102] F. Lekien, S. C. Shadden, and J. E. Marsden *J. Math. Phys.* **48**, p. 065404, 2007.
- [103] G. Haller *Physica D* **240**, pp. 574–598, 2011.
- [104] G. Haller and F. J. Beron-Vera *Physica D* **241**, pp. 1680–1702, 2012.
- [105] B. Joseph and B. Legras *J. Atm. Sci.* **59**, pp. 1198–1212, 2002.
- [106] A. Molcard, A. Poje, and T. Özgökmen *Ocean Modell.* **12**, pp. 268–289, 2006.
- [107] M. Branicki and S. Wiggins *Nonlinear Processes Geophys* **17**(1), pp. 1–36, 2010.
- [108] F. Beron-Vera, M. J. Olascoaga, M. G. Brown, K. H., and I. I. Rypina *Chaos* **20**(1), p. 017514, 2010.
- [109] Z. Pouransari, M. Speetjens, and H. Clercx *J. Fluid Mech.* **654**, pp. 5–34, 2010.
- [110] T. Schultz, H. Theisel, and H.-P. Seidel *IEEE Transactions on Visualization and Computer Graphics* **16**, pp. 109–119, 2010.
- [111] D. Eberly, R. Gardner, B. Morse, S. Pizer, and C. Scharlach *Journal of Mathematical Imaging and Vision* **4**, pp. 353–373, 1994.
- [112] F. Sadlo and R. Peikert *IEEE Transactions on Visualization and Computer Graphics* **13**, pp. 1456–1463, 2007.
- [113] J. H. Bettencourt, C. Lopez, and E. Hernandez-Garcia *Ocean Modell.* **51**, pp. 73–83, 2012.
- [114] J. H. Ferziger and M. Perić, *Computational methods for fluid dynamics*, vol. 3, Springer Berlin, 2002.
- [115] A. Shchepetkin and J. McWilliams *Ocean Modelling* **9**(4), pp. 347–404, 2005.
- [116] D. B. Haidvogel, H. Arango, W. P. Budgell, B. D. Cornuelle, E. Curchitser, E. Di Lorenzo, K. Fennel, W. R. Geyer, A. J. Hermann, L. Lanerolle, *et al.* *Journal of Computational Physics* **227**(7), pp. 3595–3624, 2008.

BIBLIOGRAPHY

- [117] J. Holmes, J. L. Lumley, and G. Berkooz, *Turbulence, Coherent Structures, Dynamical Systems and Symmetry*, Cambridge Monographs on Mechanics, Cambridge University Press, 1998.
- [118] C. Pan, J. Wang, and C. Zang *Science in China Series G: Physics, Mechanics & Astronomy* **52**, pp. 248–257, 2009.
- [119] R. D. Moser, J. Kim, and N. N. Mansour *Phys. Fluids* **11**(4), pp. 943–945, 1999.
- [120] J. F. Gibson, “Channelflow: A spectral Navier-Stokes simulator in C++,” report, U. New Hampshire, 2012.
- [121] J. Kim, P. Moin, and R. Moser *Journal of Fluid Mechanics* **177**, pp. 133–166, 1987.
- [122] J. Kim and F. Hussain *Physics of Fluids* **5**, pp. 695–706, 1993.
- [123] T. Özgökmen, A. C. Poje, P. F. Fischer, and A. C. Haza *Ocean Modell.* **39**, pp. 311–331, 2011.
- [124] M. Branicki and A. Kirwan *Int. J. Eng. Sci.* **48**, pp. 1027–1042, 2010.
- [125] C. Amante and B. W. Eakins, “ETOPO1 1 Arc-Minute Global Relief Model: Procedures, Data Sources and Analysis,” NOAA Technical Memorandum NESDIS NGDC-24, 2009.
- [126] B. Le Vu, E. Gutknecht, E. Machu, I. Dadou, J. Veitch, J. Sudre, A. Paulmier, and V. Garçon *submitted to JMR*, 2011.
- [127] A. F. Shchepetkin and J. C. McWilliams *J. Geophys. Res.* **108**, p. 3090, 2003.
- [128] A. Mahadevan *Ocean Modell.* **14**(3–4), pp. 222–240, 2006.
- [129] K. Y. Yuan, Y. S. Huang, H. T. Yang, and T. H. H. Pian *Computational Mechanics* **14**, pp. 189–199, 1994.
- [130] J. C. R. Hunt, A. A. Wray, and P. Moin, “Eddies, Streams and Convergence Zones in Turbulent Flows,” Report CTR-S88, Center for Turbulence Research, Standford University, 1988.
- [131] A. Okubo *Deep-Sea Res. I* **17**, pp. 445–454, 1970.
- [132] J. Weiss *Physica D* **48**, pp. 273–294, 1991.
- [133] S. Louazel and B. L. Hua *Physics of Fluids* **16**, pp. 3079–3085, 2004.

BIBLIOGRAPHY

- [134] G. Lapeyre, P. Klein, and B. Hua *Phys. Fluids* **11**(12), pp. 3729–3737, 1999.
- [135] A. Gnanadesikan, J. Dunne, and J. John *Biogeosciences* **9**(3), pp. 1159–1172, 2012.
- [136] R. Vaquer-Sunyer and C. Duarte *Proceedings of the National Academy of Sciences of the United States of America* **105**(40), pp. 15452–15457, 2008.
- [137] P. Lam, G. Lavik, M. Jensen, J. van de Vossenbergh, M. Schmid, D. Wobken, G. Dimitri, R. Amann, M. Jetten, and M. Kuypers *Proceedings of the National Academy of Sciences of the United States of America* **106**(12), pp. 4752–4757, 2009.
- [138] B. Ward, A. Devol, J. Rich, B. Chang, S. Bulow, H. Naik, A. Pratihary, and A. Jayakumar *Nature* **461**(7260), pp. 78–81, 2009.
- [139] A. Paulmier and D. Ruiz-Pino *Progress in Oceanography* **80**(3-4), pp. 113–128, 2009.
- [140] L. Stramma, G. Johnson, J. Sprintall, and V. Mohrholz *Science* **320**(5876), pp. 655–658, 2008.
- [141] L. Bopp, C. Le Quere, M. Heimann, A. Manning, and P. Monfray *Global Biogeochemical Cycles* **16**(2), pp. 6–1–6–13, 2002.
- [142] F. Chavez and M. Messie *Progress in Oceanography* **83**(1-4), pp. 80–96, 2009.
- [143] I. Montes, F. Colas, X. Capet, and W. Schneider *Journal of Geophysical Research-Oceans* **115**, 2010.
- [144] A. Chaigneau, A. Gizolme, and C. Grados *Progress in Oceanography* **79**(2), pp. 106–119, 2008.
- [145] L. Stramma, H. W. Bange, R. Czeschel, A. Lorenzo, and M. Frank *Biogeosciences (BG)* **10**(11), pp. 7293–7306, 2013.
- [146] M. Altabet, E. Ryabenko, L. Stramma, D. Wallace, M. Frank, P. Grasse, and G. Lavik *Biogeosciences* **9**(12), pp. 4897–4908, 2012.
- [147] I. Montes, B. Dewitte, E. Gutknecht, A. Paulmier, I. Dadou, A. Oschlies, and V. Garçon *Journal of Geophysical Research: Oceans* , pp. n/a–n/a, 2014.
- [148] E. Gutknecht, I. Dadou, P. Marchesiello, G. Cambon, B. L. Vu, J. Sudre, V. Garçon, E. Machu, T. Rixen, A. Kock, *et al. Biogeosciences* **10**(6), pp. 4117–4135, 2013.

BIBLIOGRAPHY

- [149] I. Montes, W. Schneider, F. Colas, B. Blanke, and V. Echevin *Journal of Geophysical Research-Oceans* **116**, 2011.
- [150] W. T. Liu, W. Tang, and P. S. Polito *Geophysical Research Letters* **25**(6), pp. 761–764, 1998.
- [151] A. Da Silva, C. Young, and S. Levitus *US Dep. of Commer., Washington, DC*, 1994.
- [152] J. A. Carton and B. S. Giese *Monthly Weather Review* **136**(8), pp. 2999–3017, 2008.
- [153] J. Theiss *Journal of Physical Oceanography* **34**(7), pp. 1663–1678, 2004.
- [154] P. Penven, V. Echevin, J. Pasopera, F. Colas, and J. Tam *Journal of Geophysical Research: Oceans (1978–2012)* **110**(C10), 2005.
- [155] G. Buffoni, P. Falco, A. Griffa, and E. Zambianchi *Journal of Geophysical Research: Oceans* **102**(C8), pp. 18699–18713, 1997.
- [156] I. Hernández-Carrasco, C. López, A. Orfila, and E. Hernández-García *Non-linear Processes in Geophysics* **20**(5), pp. 921–933, 2013.
- [157] L. Stramma, G. Johnson, E. Firing, and S. Schmidtke *Journal of Geophysical Research-Oceans* **115**, 2010.
- [158] R. Czeschel, L. Stramma, F. Schwarzkopf, B. Giese, A. Funk, and J. Karstensen *Journal of Geophysical Research-Oceans* **116**, 2011.
- [159] Y. Lehahn, F. d’Ovidio, M. Lévy, and E. Heifetz *Journal of Geophysical Research: Oceans (1978–2012)* **112**(C8), 2007.
- [160] A. Chaigneau, M. Le Texier, G. Eldin, C. Grados, and O. Pizarro *Journal of Geophysical Research: Oceans (1978–2012)* **116**(C11), 2011.
- [161] C. Torrence and G. P. Compo *Bulletin of the American Meteorological society* **79**(1), pp. 61–78, 1998.
- [162] P. Relvas, E. D. Barton, J. Dubert, P. B. Oliveira, A. Peliz, J. Da Silva, and A. M. P. Santos *Progress in Oceanography* **74**(2), pp. 149–173, 2007.
- [163] E. Barton, *Canary and Portugal currents*, Academic press, 2001.
- [164] X. A. Álvarez-Salgado, J. Arístegui, E. D. Barton, D. A. Hansell, *et al.* *Limnology and oceanography* **52**(3), pp. 1287–1292, 2007.

BIBLIOGRAPHY

- [165] X. A. Álvarez-Salgado, M. Doval, A. Borges, I. Joint, M. Frankignoulle, E. Woodward, and F. Figueiras *Progress in Oceanography* **51**(2), pp. 321–337, 2001.
- [166] P. T. Strub, P. M. Kosro, and A. Huyer *Journal of Geophysical Research: Oceans (1978–2012)* **96**(C8), pp. 14743–14768, 1991.
- [167] M. L. Batteen, C. N. Lopes da Costa, and C. S. Nelson *Journal of marine systems* **3**(3), pp. 249–266, 1992.
- [168] R. Haynes, E. D. Barton, and I. Pilling *Journal of Geophysical Research: Oceans (1978–2012)* **98**(C12), pp. 22681–22692, 1993.
- [169] T. Meunier, V. Rossi, Y. Morel, and X. Carton *Ocean Modelling* **35**(4), pp. 277–303, 2010.
- [170] E. Barton, M. Inall, T. Sherwin, and R. Torres *Progress in Oceanography* **51**(2), pp. 249–267, 2001.
- [171] V. Rossi, V. Garçon, J. Tassel, J.-B. Romagnan, L. Stemmann, F. Jourdin, P. Morin, and Y. Morel *Continental Shelf Research* **59**, pp. 97–114, 2013.
- [172] Á. Peliz, T. L. Rosa, A. M. P. Santos, and J. L. Pissarra *Journal of Marine Systems* **35**(1), pp. 61–77, 2002.
- [173] D. B. Haidvogel and A. Beckmann, *Numerical Ocean Circulation Modeling*, World Scientific Publishing Company, Dec. 1999.
- [174] G. L. Mellor and T. Yamada *J Atmos Sci* **31**, pp. 1791–1806, 1974.
- [175] A. J. Wallcraft, E. J. Metzger, and S. N. Carroll, “HYCOM Design Description for the HYbrid Coordinate Ocean Model (HYCOM) Version 2.2,” tech. rep., Naval Research Laboratory, Stennis Space Center, MS, 2009.
- [176] P. Marchesiello, J. C. McWilliams, and A. Shchepetkin *Ocean Modelling* **3**(1–2), pp. 1–20, 2001.
- [177] D. Chapman *J Phys Oceanogr* **15**, pp. 1060–1075, 1985.
- [178] R. Flather *Mémoires de la Société Royale des Sciences de Liège* **6**, pp. 141–164, 1976.
- [179] M. Marta-Almeida, J. Dubert, Á. Peliz, A. dos Santos, and H. Queiroga *Canadian Journal of Fisheries & Aquatic Sciences* **65**, pp. 2253–2268, Oct. 2008.

BIBLIOGRAPHY

- [180] P. Otero, M. Ruiz-Villarreal, and A. Peliz *Journal of Marine Systems* **72**, pp. 238–255, July 2008.
- [181] M. Marta-Almeida, M. Ruiz-Villarreal, J. Pereira, P. Otero, M. Cirano, X. Zhang, and R. D. Hetland *Marine Pollution Bulletin* **71**, pp. 139–151, June 2013.
- [182] R. D. Hetland *Ocean Modelling* **11**, pp. 214–223, 2006.
- [183] Martinho Marta-Almeida, R. D. Hetland, and X. Zhang *Journal of Geophysical Research: Oceans* **118**, pp. 2476–2491, May 2013.
- [184] A. Barth, A. Alvera-Azcárate, and R. H. Weisberg *Cont Shelf Res* **28**, pp. 561–573, 2008.
- [185] X. Zhang, R. D. Hetland, M. Marta-Almeida, and S. F. DiMarco *Journal of Geophysical Research* **117**, Nov. 2012.
- [186] K. Fennel, J. Hu, A. Laurent, M. Marta-Almeida, and R. Hetland *Journal of Geophysical Research: Oceans* **118**, pp. 990–1002, Feb. 2013.
- [187] F. Amorim, M. Cirano, M. Marta-Almeida, J. Middleton, and E. Campos *Continental Shelf Research* **65**, pp. 121–140, Aug. 2013.
- [188] D. P. Dee, S. M. Uppala, A. J. Simmons, P. Berrisford, P. Poli, S. Kobayashi, U. Andrae, M. A. Balmaseda, G. Balsamo, P. Bauer, P. Bechtold, A. C. M. Beljaars, L. van de Berg, J. Bidlot, N. Bormann, C. Delsol, R. Dragani, M. Fuentes, A. J. Geer, L. Haimberger, S. B. Healy, H. Hersbach, E. V. Hólm, L. Isaksen, P. Kållberg, M. Köhler, M. Matricardi, A. P. McNally, B. M. Monge-Sanz, J.-J. Morcrette, B.-K. Park, C. Peubey, P. de Rosnay, C. Tavolato, J.-N. Thépaut, and F. Vitart *Quarterly Journal of the Royal Meteorological Society* **137**(656), pp. 553–597, 2011.
- [189] R. Atlas, R. N. Hoffman, J. Ardizzone, S. M. Leidner, J. C. Jusem, D. K. Smith, and D. Gombos *Bull. Amer. Meteor. Soc.* **92**, pp. 157–174, Oct. 2010.
- [190] P. Otero, M. Ruiz-Villarreal, Á. Peliz, and J. M. Cabanas *Scientia Marina* **74**, pp. 247–266, June 2010.
- [191] A. da Silva, A. C. Young, and S. Levitus, “Atlas of Surface Marine Data 1994, Volume 1: Algorithms and Procedures,” NOAA Atlas NESDIS 6, U.S. Department of Commerce, Washington, D.C., 1994.

- [192] K. Fedorov and A. Ginsburg, “Mushroom-Like Currents (Vortex Dipoles): One of the Most Widespread Forms of Non-Stationary Coherent Motions in the Ocean,” in *Mesoscale/Synoptic Coherent structures in Geophysical Turbulence*, J. Nihoul and B. Jamart, eds., *Elsevier Oceanography Series* **50**, pp. 1–14, Elsevier, 1989.
- [193] J. H. Churchill, P. C. Cornillon, and G. W. Milkowski *Journal of Geophysical Research: Oceans (1978–2012)* **91**(C8), pp. 9615–9623, 1986.
- [194] L.-Y. Oey and H. Zhang *Continental shelf research* **24**(18), pp. 2109–2131, 2004.
- [195] G. G. Sutyrin and R. Grimshaw *Ocean Modelling* **32**(1), pp. 25–35, 2010.
- [196] D. Garcia *Computational statistics & data analysis* **54**(4), pp. 1167–1178, 2010.
- [197] D. Garcia *Experiments in fluids* **50**(5), pp. 1247–1259, 2011.

Curriculum Vitae

João Paulo Horta Bettencourt

IFISC – Instituto de Física Interdisciplinar y Sistemas Complejos
Campus Universitat de les Illes Balears

E-07122 Palma de Mallorca

Spain

Phone: +34 647 57 82 62

email: joaob@ifisc.uib-csic.es

Research interests

Turbulence · Ocean dynamics · Dynamical systems · Numerical modeling of fluid flows · Ocean surface waves · Climate

Research background

My research experience started when I was still an undergraduate student in my bachelor studies of Naval Architecture and Marine Engineering with grant for introduction to research. During this grant my activities were related to the field of fluid mechanics of the sailing yacht and more specifically to the aerodynamics of sails. During this period I mostly wrote computer codes in FORTRAN to compute wind forces on sails based on potential flow theory. After my graduation, I started to work in the Unit of Marine Technology and Engineering as a graduate researcher and I also enrolled in my MSc. Studies. During this period I continued my research into sailing yacht aerodynamics and hydrodynamics, using computational methods of fluid dynamics (CFD) to compute fluid forces on keels of sailing yachts. Later I did experimental work on a rigid wing sail in a wind tunnel that led to my MSc dissertation. I worked for two years as a design engineer in Norway where I developed industry work in the field of marine propulsion analysis and design. After this two year interval I started my PhD in Physics at the Institute of Interdisciplinary Physics and Complex Systems (IFISC) in the field of dynamical systems and oceanic turbulent processes.

Current position

2009 PHD CAND. in Physics, IFISC, University of Balearic Islands-CSIC
Thesis project: Three-dimensional Lagrangian structures in turbulent flows:
applications to oceanic processes

IFISC (Institute for Cross-Disciplinary Physics and Complex Systems) is a joint research Institute of the University of the Balearic Islands (UIB) and the Spanish National Research Council (CSIC)

Past positions

2009 DESIGN ENGINEER at Liaaen Teknologi
2008 DESIGN ENGINEER at Brunvoll Thrusters
2003 RESEARCH ASSISTANT in Hydrodynamics, Technical University of Lisbon

Education

2009 MSc in Naval Architecture and Marine Engineering
Technical University of Lisbon

2003 LIC. in Naval Architecture and Marine Engineering
Technical University of Lisbon

Publications

Journal articles

João H Bettencourt, Cristóbal López, and Emilio Hernández-García. Characterization of coherent structures in three-dimensional turbulent flows using the finite-size Lyapunov exponent. *Journal of Physics A: Mathematical and Theoretical*, 46(25):254022, 2013.

João H. Bettencourt, Cristóbal López, and Emilio Hernández-García. Oceanic three-dimensional Lagrangian coherent structures: A study of a mesoscale eddy in the Benguela upwelling region. *Ocean Modelling*, 51(0):73–83, 2012.

S. Ponce de León, J.H. Bettencourt, and N. Kjerstad. Simulation of irregular waves in an offshore wind farm with a spectral wave model. *Continental Shelf Research*, 31(15):1541–1557, 2011.

Proceedings

E. Hernández-García, J.H. Bettencourt, V. Garçon, I. Hernandez-Carrasco, C. López, V. Rossi, J. Sudre, and E. Tew Kai. Biological Impact of Ocean Transport: A Finite-Size Lyapunov Characterization. In Dumitru Baleanu, Ziya Burhanettin Guvenc, and Ozlem Defterli, editors, *Proceedings of the 3rd Conference on Nonlinear Science and Complexity*. Cankaya University, 2012.

Workshops and conferences

João H. Bettencourt, Cristóbal López, Emilio Hernández-García, Ivonne Montes, Joël Sudre, Boris Dewitte, Aurélien Paulmier, and Véronique Garçon. Mesoscale structures as barriers to mixing in the East Tropical Pacific Oxygen Minimum Zone. In *46th International Liège Colloquium*, Liège, Belgium, May 2014. ULg.

João H. Bettencourt, Cristóbal López, and Emilio Hernández-García. Lagrangian coherent structures and plankton dynamics. In *The Ramón Margalef Summer Colloquia*, Barcelona, Spain, July 2013. ICM.

João H. Bettencourt, Cristóbal López, Emilio Hernández-García, Ivonne Montes, Joël Sudre, Boris Dewitte, Aurélien Paulmier, and Véronique Garçon. Lagrangian variability of the Eastern Tropical Pacific Oxygen Minimum Zone. In *European Geosciences Union Annual Meeting*, Vienna, Austria, April 2013. EGU.

João H. Bettencourt, Cristóbal López, and Emilio Hernández-García. Oceanic three-dimensional Lagrangian Coherent Structures in the Benguela ocean region. In *European Geosciences Union Annual Meeting*, Vienna, Austria, April 2012. EGU.

João H. Bettencourt, Cristóbal López, and Emilio Hernández-García. Estruturas Lagrangianas coerentes na mesoescala oceânica. In *Encontro de Oceanografia Física*, Figueira da Foz, Portugal, June 2012.

João H. Bettencourt, Cristóbal López, and Emilio Hernández-García. Mesoscale three-dimensional Lagrangian Coherent Structures. In *2nd International Workshop on Nonlinear Processes in Atmospheric and Oceanic Flows*, Madrid, Spain, July 2012. ICMAT-Universidad Autónoma de Madrid.

João H. Bettencourt, Cristóbal López, and Emilio Hernández-García. Coherent Structures in Three-Dimensional Flows. In *Workshop Coherent Structures in Dynamical Systems*, Leiden, Netherlands, May 2011. Lorentz Center.

João H. Bettencourt, Cristóbal López, and Emilio Hernández-García. Coherent Structures in a Three Dimensional Turbulent Velocity Field. In *Living organisms in flows: From small-scale turbulence to geophysical flows*, Palma de Mallorca, Spain, June 2010. IFISC.

Other scientific activities

Visit to LEGOS (Laboratoire d'Études en Géophysique et Océanographie Spatiales) in Toulouse October 2012 to work under supervision of Dr. Véronique Garçon (CNRS)

Reviewer for Physica D, Ocean Modelling and ZAMP (Zeitschrift fuer Angewandte Mathematik und Physik)

Computer skills

Programming in FORTRAN90, Matlab, Python2.7

Latex

Finite-element analysis software (ANSYS Mechanical)

Computational Fluid Dynamics software (ANSYS Fluent)
3D CAD software (CATIA V5, NX 6)
Large dataset manipulation in NetCDF and HDF5 format
Satellite data retrieval and manipulation:
ENVISAT, JASON1, JASON2, TOPEX-POSEIDON Altimetry
SeaWiFS Ocean color

*E quanto às notícias do futuro
não as encontrei no livro dos dogmas.*

Fernando Namora

